Fall 2023

A 10x Visium Approach: A Spatial RNA-Seq Analysis of Renal Tissue in Peromyscus eremicus

Molly Kephart
University of New Hampshire

A 10x Visium Approach: A Spatial RNA-Seq Analysis of Renal Tissue in *Peromyscus eremicus*

BY

MOLLY KEPHART

B.S. in Biochemistry, Molecular, and Cellular Biology, University of New Hampshire, 2020

THESIS

Submitted to the University of New Hampshire

In Partial Fulfillment of

The Requirements for the Degree of

Master of Science

In

Genetics

September 2023

This thesis has been examined and approved in partial fulfillment of the requirements of the degree of Master of Science in Genetics by:

Thesis Director, Matthew D. MacManes, Ph.D, Molecular, Cellular, and Biomedical Sciences

W. Kelley Thomas, Ph.D, Molecular, Cellular, and Biomedical Sciences

David C. Plachetzki, Ph.D, Molecular, Cellular, and Biomedical Sciences

On July 20, 2023

Approval signatures are on file with the University of New Hampshire Graduate School.

TABLE OF CONTENTS

LIST OF TABLES……viii

LIST OF FIGURES……..viv

ABSTRACT……..xii

CHAPTER ONE: INTRODUCTION……..1

Normal Kidney Function and How Water Balance Is Maintained……..……..3

Adaptations to Dehydration-Related Effects in Desert-Adapted Mammals……...…..5

Peromyscus eremicus as a Desert-Adapted Model …….....6

Previous Studies Involving Peromyscus eremicus…...……...6

Utilizing Spatial Transcriptomics Within Peromyscus eremicus ……...…...8

Objectives and Aims……9

CHAPTER TWO: A 10X VISIUM ANALYSIS OF *PEROMYSCUS EREMICUS*: A SPATIAL APPROACH TO RNA-SEQ…….….11

INTRODUCTION……....11

METHODS……...14

Tissue Sectioning……...……...14

Fixation, Staining, and Imaging…….15

Tissue Optimization and Permeabilization…….15

Reverse Transcription and Library Preparation……...16

Sequencing and Initial Processing……..17

Data Processing ……17

RESULTS……..19

Library Prep Results, Including Sectioning Permeabilization……....19

Sequencing Results and Statistics……*20*

Assessing Spatial Libraries in Seurat……....22

Exploring Cell Markers using BayesSpace……..26

AQP Family Expression……....30

Sodium-Related Gene Expression……*31*

Differential Gene Expression Between Spatial Clusters……32

DISCUSSION……...35

Initial Clustering and Spatial Relevance……..35

AQP Gene Family……..37

Sodium-Related Gene Expression……38

GO Term Enrichment Within Clusters……..39

Cluster Specific GO Analysis……42

CHAPTER THREE: DISCUSSION AND FUTURE DIRECTIONS……...45

Conclusions……...45

What Is Still Unknown?.....48

Future Studies……...……50

REFERENCES……..51

APPENDICIES……..62

APPENDIX I: UMAP GRAPHS FOR TISSUE SAMPLES B1 AND C1……...62

APPENDIX II: SPATIAL CLUSTERING AND TOP 10 HIGHLY EXPRESSED GENES FOR TISSUE SAMPLE B1……....63

APPENDIX III: SPATIAL CLUSTERING AND TOP 10 HIGHLY EXPRESSED GENES FOR TISSUE SAMPLE C1……....64

APPENDIX IV: SPATIAL CLUSTERING AND TOP 10 HIGHLY EXPRESSED GENES FOR TISSUE SAMPLE D1……....65

APPENDIX V: CORTEX MARKER GENE SPATIAL LOCATION AND EXPRESSION LEVEL PLOTS FOR TISSUE B1……...66

APPENDIX VI: MEDULLARY AND RENAL PELVIS MARKER GENE SPATIAL LOCATION AND EXPRESSION LEVEL PLOTS FOR TISSUE B1……....67

APPENDIX VII: CORTEX MARKER GENE SPATIAL LOCATION AND EXPRESSION LEVEL PLOTS FOR TISSUE C1……...68

APPENDIX VIII: MEDULLARY AND RENAL PELVIS MARKER GENE SPATIAL LOCATION AND EXPRESSION LEVEL PLOTS FOR TISSUE C1……....69

APPENDIX IX: CORTEX MARKER GENE SPATIAL LOCATION AND EXPRESSION LEVEL PLOTS FOR TISSUE D1……..70

APPENDIX X: MEDULLARY AND RENAL PELVIS MARKER GENE SPATIAL LOCATION AND EXPRESSION LEVEL PLOTS FOR TISSUE D1……....71

APPENDIX XI: GENE MARKER MAPS OF MAJOR CELL TYPES IN THE KIDNEY FOR TISSUE B1……....72

APPENDIX XII: GENE MARKER MAPS OF MAJOR CELL TYPES IN THE KIDNEY FOR TISSUE C1……....74

APPENDIX XIII: GENE MARKER MAPS OF MAJOR CELL TYPES IN THE KIDNEY FOR TISSUE D1……...76

APPENDIX XIV: SODIUM RELATED GENE LOG NORMALIZED EXPRESSION VALUE VIOLIN PLOTS FOR TISSUE B1……78

APPENDIX XV: SODIUM RELATED GENE LOG NORMALIZED EXPRESSION VALUE VIOLIN PLOTS FOR TISSUE C1……79

APPENDIX XVI: SODIUM RELATED GENE LOG NORMALIZED EXPRESSION VALUE VIOLIN PLOTS FOR TISSUE D1……80

APPENDIX XVII: AQP GENE FAMILY LOG NORMALIZED EXPRESSION VALUE VIOLIN PLOTS FOR TISSUE B1……81

APPENDIX XVIII: AQP GENE FAMILY LOG NORMALIZED EXPRESSION VALUE VIOLIN PLOTS FOR TISSUE C1……82

APPENDIX XIX: AQP GENE FAMILY LOG NORMALIZED EXPRESSION VALUE VIOLIN PLOTS FOR TISSUE D1……..83

APPENDIX XX: AVERAGE LOG2 FOLD CHANGE HEATMAP OF TOP 10 GENES PER CLUSTER FOR TISSUE B1……...84

APPENDIX XXI: AVERAGE LOG2 FOLD CHANGE HEATMAP OF TOP 10 GENES PER CLUSTER FOR TISSUE C1……85

APPENDIX XXII : AVERAGE LOG2 FOLD CHANGE HEATMAP OF TOP 10 GENES PER CLUSTER FOR TISSUE D1……86

APPENDIX XXIII: GO TERMS FOR TOP 10 GENES PER CLUSTER FOR TISSUE A1……...87

APPENDIX XXIV: CLUSTER 0 PAIRWISE GO TERMS RESULTS FOR TISSUE A1……....89

APPENDIX XXV: CLUSTER 1 PAIRWISE GO TERM RESULTS FOR TISSUE A1……....91

APPENDIX XXVI: CLUSTER 2 PAIRWISE GO TERM RESULTS FOR TISSUE A1……...92

APPENDIX XXVII: CLUSTER 3 PAIRWISE GO TERM RESULTS FOR TISSUE A1……...93

APPENDIX XXVIII: CLUSTER 4 PAIRWISE GO TERM RESULTS FOR TISSUE A1……..96

APPENDIX XXIX: CLUSTER 5 PAIRWISE GO TERMS RESULTS FOR TISSUE A1……..101

APPENDIX XXX: CLUSTER 6 PAIRWISE GO TERM RESULTS FOR TISSUE A1……..103

APPENDIX XXXI: IACUC APPROVAL LETTER……...105

LIST OF TABLES

Table 2-1. Table 2-1: Table of cell type marker genes that were used to define cell type in tissue samples. This table was adapted from information obtained from Clark et al., 2019, Park et al. 2018, and Balzer et al., 2022……..27

Table 2-2. Top ten genes per cluster in tissue A1. Gene expression is based on log2 fold change. Gene list was generated via Seurat's SpatiallyVariableFeatures function…….…….33

LIST OF FIGURES

Figure 2-1. Layout of 10X Visium tissue optimization slide (TOS) on the left and gene expression slide (GES) on the right. TOS slide shows time point layouts for permeabilization optimization experiment (B1 =30 minutes, C1 = 24 minutes, D1 = 18 minutes, A2 = 12 minutes, B2 = 6 minutes, and C2 = 3 minutes), along with control layout (A1 = positive control, D2 = negative control). GES slide layout outlines placement and naming (A1-B1 = male slices, C1-D1 = female slices). Image created with BioRender.com……...16

Figure 2-2. Fluorescent imaging of the tissue optimization slide for *P. eremicus* kidney tissue. Top Left (A1) is positive control, B1 was the 30-minute time mark, C1 was 24 minutes, D1 18 minutes, A2 12 minutes, B2 6 minutes, C2 3 minutes, and D2 was a negative control. Time frame 18 minutes was chosen for the permeabilization time due to the strength of fluorescence…….20

Figure 2-3. UMAP plotting of the spatial clusters defined by Seurat package. Tissue A1 (male) UMAP is on the left, while tissue D1 (female) is on the right……...22

Figure 2-4. Spatial Processing of A1 Tissue Section. 4a (top left) shows Seurat defined clusters projected on top of histological tissue image. 4b (top right) shows individual clusters projected back on to histological image for more direct understanding of cluster definition. 4c (bottom) is a spatially rendered heat map of the top 10 most highly expressed genes (SLC34A1, APOM, PRODH2, ATP12A, ACOT13, ACSM2, AKR1A1, PC, HGD, and S100A6) and their log normalized expression value…….23

Figure 2-5. Spatial visualization of cortical (proximal tubule) marker genes GLYAT, UPB1, and SLC5A2. Spatial plots and correlating violin plots show gene expression location (top) and log normalized expression per cluster (bottom). Y-axis is the log normalized expression level, and each dot represents a spot within the cluster. X-axis position is arbitrary……..….24

Figure 2-6. Spatial visualization of medullary (loop of Henle) marker gene CLDN19. Spatial plot (left) shows location of expression, and violin plot (right) shows log normalized expression per cluster. Y-axis is the log normalized expression level, and each dot represents a spot within the cluster. X-axis position is arbitrary…...…...…….25

Figure 2-7. Spatial Visualization of renal pelvis marker gene AKR1B1. Spatial plot (left) shows location of expression, and violin plot (right) shows log normalized expression per cluster. Y-axis is the log normalized expression level, and each dot represents a spot within the cluster. X-axis position is arbitrary……..…….25

Figure 2-8. Spatially plotted marker gene log normalized expressions for the major cell types recognized in the kidney. Shorthand labels correlate as follows: Endo = endothelial cells, Podo = podocytes, Mes = mesangial cells, PT = proximal tubules, CNT = connecting tubules, LOH = loop of Henle, DCT = distal connecting tubules, CD-PC = collecting duct principal cells, CD-IC = collecting duct interstitial cells, Fib = fibroblast, Macro = macrophage, Neutro = neutrophils, B Lymph = B lymphocytes……...28

Figure 2-9. Visualization of loop of Henle-specific cell type markers and their log normalized expression. Shorthand labels correlate as follows: LOH = Loop of Henle (combination of

all marker genes), SLDL = short loop descending limb, LDL = long descending limb, THINAL = thin ascending limb, THICKAL = thick ascending limb……29

Figure 2-10. Visualization of proximal tubule-specific cell type markers and their log normalized expression levels. Shorthand labels correlate as follows: PT = proximal tubules (all marker genes), S1 = S1 segment, S2 = S2 segment, S3 = S3 segment……..29

Figure 2-11. AQP gene family log normalized expression by cluster. Y-axis is the log normalized expression level, and each dot represents a spot within the cluster. X-axis position is arbitrary. AQP1, AQP3, AQP4, and AQP6 had markedly less expression and distribution among the clusters than AQP7, which shows high levels of abundance in clusters 1, 2, 3 and 5……...30

Figure 2-12. Violin plots of log normalized expression levels of sodium-related genes by cluster. Y-axis is the log normalized expression level, and each dot represents a spot within the cluster. X-axis position is arbitrary. KCNJ1, SLC12A3, SCNN1B, AGT, WNK1, and WNK2 had reduced expression across the tissue clusters compared to SLC12A1, SCNN1G, SGK1, WNK3, and WNK4. ….....32

Figure 2-13. Heat map of the log2 fold change of the top ten genes expressed in each cluster compared to expression values in the other clusters. Duplicate genes are not included in the heatmap, which may reflect in the total number of genes shown. Cluster numbers are shown on the X-axis, while gene names are shown on the Y-axis…….……34

ABSTRACT

A 10X VISIUM APPROACH: A SPATIAL RNA-SEQ ANALYSIS OF RENAL TISSUE IN *PEROMYSCUS EREMICUS*

By

Molly Kephart

University of New Hampshire, September, 2023

Arid environments continue to increase their global coverage yearly due to climate change, and leaves harsh environmental effects in their wake. Of these effects—which include high UV radiation, extreme temperatures, and sparse food sources —lack of free water poses the greatest challenge to the ecosystem as a whole. Water resources are predicted to continue to decrease with the rise in desertification, increasing the threat of dehydration and its harmful effects on bodily function. Dehydration-related kidney injury has been linked to the onset of chronic kidney disease in humans, which has become a leading cause of mortality worldwide. Therefore, studies focusing on dehydration and its effects on the kidney are pertinent to human health in the midst of global warming. Desert-adapted mammals provide an excellent model for studying dehydration, as their environment often forces them to survive on minimal extrinsic water. *Peromyscus eremicus,* commonly known as the cactus mouse, have been known to go their entire life without water intake, but seemingly do not incur excessive kidney damage. Additionally, they are able to be studied in a laboratory setting and have publicly available genomic information, making them an ideal research candidate. While multiple studies outlining their physiology and kidney function exist, none include spatial relevance of their findings. The research outlined here serves as preliminary work for future studies by utilizing the 10X Genomics Visium platform to generate a spatial atlas of genes expressed in the kidney of

Peromyscus eremicus. The specific objectives of this research were to (1) explore cell type distribution across the kidney using previously defined cell type markers, (2) to define spatially resolved clusters by cell type, gene expression, and location, (3) to explore location and expression values of previously significant genes, and (4) to explore differential gene expression patterns across the kidney tissue. Spatial libraries were generated from four kidney slices of wildtype mice using 10X Visium guidelines. Preliminary processing was performed using their publicly available pipeline called Spaceranger. Further analysis was completed using the R packages Seurat and BayesSpace, which allowed us to identify and define spatial clusters. Major cell types were defined from previously discovered cell marker genes and visualized using BayesSpace's advanced subspot resolution. Specifically, the proximal tubules and the loop of Henle were described with high levels of certainty with regard to location and gene expression. Exploration of expression level and locations of genes previously studied in relation to dehydration revealed that genes involved with epithelial sodium channels (ENaC) and sodium-potassium-chloride cotransporters (NKCC2) were highly expressed, while the aquaporin gene family as a whole was not expressed (excluding AQP7) compared to previous literature. Finally, GO term analyses of highly variable genes per cluster were performed to further assign functionality and features to the defined spatial clusters. Overall, the results from this study lay the groundwork for understanding how desert-adapted mammals may cope with lack of water in their environment and provide insight to how humans may one day be able to treat and prevent dehydration-related disease states. These results also provide preliminary information to further investigate spatially relevant information in future dehydrated *P. eremicus* studies.

CHAPTER ONE: INTRODUCTION

Arid desert environments comprise approximately 30% of global land surface today, and that percentage continues to increase annually (Johnson et al., 2016). Deserts present a multitude of challenges to the ecosystem, including extreme temperatures, food source scarcity, high UV exposure, salinity, and humidity. However, one of the most pressing issues is the lack of water availability (Osborne et al., 2020). With the rise of climate change, it is predicted that water resources on earth will continuously decrease, leading to the potential increase of dehydration related diseases (Johnson et al., 2016). Acute kidney injury (AKI) and chronic kidney disease (CKD) are estimated to affect upwards of 45 million people globally, and numbers are predicted to rise as heat waves intensify (Chapman et al., 2020; Roncal-Jimenez et al., 2015). Therefore, research that provides insight to how mammals survive acute and chronic dehydration while maintaining water homeostasis will be of the utmost importance. However, the response to dehydration in humans and other mammals has been shown to vary widely between species and even between individuals (Cheuvront et al., 2013; Stavros, 2002; Dawson et al., 2007). Typically, in non-desert specialists, electrolyte imbalances and kidney injury occur shortly after dehydration begins (Bouby et al., 2003). In contrast, desert-adapted animal models have evolved strategies to overcome acute and chronic dehydration that occurs due to their environment (Ali et al., 2020; Randall et al., 1993; Schwimmer et al., 2009; Rocha et al., 2021; Ghobrial et al., 1975; Wu et al., 2014; Naga et al., 2021). While many of their adaptations are behavioral effects such as nocturnal lifestyle and foraging choices (Randall et al., 1993), physiological changes to renal histology (Altschuler et al., 1979) and metabolic water production have been observed (Cortés et al., 2000) .

Characterization of the gene processes that relate to desert adaptation and how they present physiologically has been a point of interest in many studies (Gallardo et al., 2005; Kaissling et al., 1975; Marra et al., 2014). Among the desert-adapted models that have been studied, *Peromyscus eremicus*, the desert cactus mouse, has proven to be an excellent system to explore adaptations related to dehydration. This desert rodent can live its entire life without fluid intake, but rarely experiences acute kidney damage (MacManes et al., 2014). A full characterization of their transcriptome (MacManes et al., 2014) and genome (Tigano et al., 2020) has been completed, along with studies to characterize the effects of acute dehydration and the genetic underpinnings of their renal phenotypes (Kordonowy et al., 2017; MacManes et al., 2017). Past studies that have sought to define the genetic mechanisms utilized by desert rodents have found the aquaporins (AQP), a protein family that helps maintain water balance in the kidney, and the solute carriers, a gene family that functions to maintain electrolyte levels across the body, to be particularly important to renal homeostasis (Macmanes et al., 2014; Macmanes et al., 2017, Brown et al., 1995; Verkman et al., 2002; Marra et al., 2014). Current next-generation sequencing technologies have allowed us to explore bulk RNA-Seq and single cell expression datasets of different tissues associated with dehydration. However, spatial relevance of the data is lost when tissues are dissociated for RNA extraction. This creates a lack of understanding between relevant cellular interactions and regional gene expression patterns (Dixon et al., 2022).

In recent years, the company 10X Genomics (Pleasanton, CA, USA) has developed a new platform called 10X Visium, which seeks to help bridge the gap between gene expression and spatial location. This is achieved by spatially barcoding all mRNA released from a tissue sample of choice by placing the tissue on an oligo-embedded slide, allowing the user to build sequencing libraries while maintaining histological relevance. The objective of this study was to utilize 10X

Visium's high-throughput sequencing-based approach to reach a deeper understanding of spatially resolved patterns of gene expression across the kidney of *Peromyscus eremicus*. This study lays the groundwork for understanding the gene level differences between desert-adapted and non-desert adapted systems and sets up future comparisons of acutely dehydrated *P. eremicus* to their non-dehydrated state.

Normal Kidney Function and How Water Balance Is Maintained

Dehydration is characterized by excessive loss of body water and is intimately connected with renal dysfunction. Vasopressin, also known as the antidiuretic hormone (ADH), is the first hormone to be excreted during dehydration (Kjær et al., 2000) and is responsible for the concentration of urine (Bouby et al., 2003). Vasopressin is released by the posterior pituitary gland due to increases in serum osmolarity, which occurs when body fluid is lost and produces a hyperosmolar state (Roncal-Jimenez et al., 2015). Vasopressin release can be triggered by blood osmolarity changes as little as 2 mOsm/L (Cuzzo et al., 2022). Three receptors for vasopressin have been identified: V1a, V1b, and V2 (Bankir et al., 2017). Both V1a and V1b utilize calcium as a second messenger, while V2 utilizes cAMP. While all receptors are triggered during dehydration, it has been found that the majority of vasopressin's antidiuretic action comes from the activation of V2 in the renal collecting duct (Bouby et al., 2003).

Vasopressin induces morphological changes in the kidney under dehydrative stress by increasing water permeability. This is achieved by promoting the insertion of aquaporin 2 (AQP2) in the luminal membrane of the collecting duct (Bankir et al.,2017). These water channel proteins help increase water absorption within the kidney to mediate the effects of dehydration (Bouby et al., 2003; Esteva-Font et al., 2012; Burg et al., 2007).

Another major factor of dehydration is the total concentration of electrolytes in the body. Sodium has been identified as one of the most osmotically active electrolytes (Esteva-Font et al., 2012), and total sodium concentration can be directly correlated to extracellular fluid volume (Burg et al., 2007). Consequently, many mechanisms within the body exist to keep the sodium concentration gradient in homeostasis. In the collecting ducts and thick ascending limb of the loop of Henle, membrane transport proteins such as ENaC (epithelial sodium channels) and NKCC2 (Na-K-Cl cotransporter) facilitate sodium movement across the plasma membranes, and are stimulated by vasopressin via the V2R receptor (Bankir et al., 2017). Due to its common coupling with sodium as NaCl, chloride is also considered an important electrolyte that is regulated within the kidney (Esteva-Font et al., 2012; Burg et al., 2007).

When these mechanisms are interrupted due to dehydration, the result is a hyperosmolar state. Hyperosmotic states have been associated with double-stranded DNA breaks, oxidative stress, apoptosis, and inhibition of transcription and translation (MacManes et al., 2017). Due to these effects, untreated dehydration in humans can result in ischemia, Acute Kidney Injury (AKI), and in extreme cases death (Mehta et al., 2015). While once thought completely reversable if treated in time, studies have begun connecting AKI with the rise of CKD, which is expected to affect >10% of the world's population (Roncal-Jimenez et al., 2015; Kovesdy et al., 2011).

Adaptations to Dehydration-Related Effects in Desert-Adapted Mammals

If such severe consequences of dehydration within non-desert adapted mammals are observed, it would be advantageous for desert mammals to evolve adaptations to combat dehydration. Indeed, it has been noted across many studies that desert-adapted mammals show phenotypic adaptations in relation to dehydrative stress (MacManes et al., 2014; Giorello et al., 2018, Cortes et al., 2000; Altschuler et al.,1979; Marra et al., 2014; Ali et al., 2020; Kailssling et al., 1975; Blumstein et al., 2022). In studies focusing on camels, GO term analyses showed an overrepresentation of genes associated with metal ion binding and regulation of body fluid levels (Wu et al., 2014). Another study on camels reported an enrichment for ion transport pathways, along with an upregulation of AQP2, and for the sodium solute carrier SLC9A7 (Alvira-Iraizoz et al., 2021).

In a study exploring the comparison of renal physiology between the desert-adapted kangaroo rat (*Dipodomys spectabilis*) and a non-desert-adapted rodent species, differential gene expression was found in solute carrier proteins (SLC12A1, SLC12A3), which work as sodium/chloride/potassium transporters within the kidney (Marra et al., 2012). In humans, mutations of these genes lead to a reduced ability to reabsorb salt (Herbert, 1998). In another study performed by Marra *et. al.,* genes in the Aquaporin protein family were found to be upregulated, along with genes related to the renin-angiotensin system (RAAS) (Marra et al., 2014). The RAAS system is connected to reduced urine production and increased sodium absorption (Fountain et al., 2023). Angiotensin (specifically Angiotensin II) receptor binding leads to reabsorption of sodium in the proximal tubules, restriction of blood flow, and altered filtration rates in the kidney (Siragy, 2009). These effects lead to a release of aldosterone, which also increases sodium reabsorption (Scott et al., 2023). This heavily increased intake of sodium

leads to a drop in urine production, which in turn encourages water reabsorption in the body (Ardaillou et al., 1999).

Peromyscus eremicus as a Desert-Adapted Model

Among the species used to examine evolutionary adaptations to dehydration is *Peromyscus eremicus*, commonly known as the cactus mouse. *P. eremicus* is endemic to the southwestern U.S.A. and has shown a multitude of behavioral and physiological adaptations to their desert environment (Kordonowy et al., 2017; MacManes et al., 2014; MacManes et al., 2017; Colella et al., 2021; Blumstein et al., 2022). As a consequence of their desert environment, they may spend their entire life with little to no oral water intake and often do not urinate (MacManes et al., 2017). However, despite their seemingly constant state of dehydration, no significant kidney damage has been observed in past studies (Kordonowy et al., 2017). *P. eremicus* also shares characteristics with other model organisms, such as the capability to be reared in the laboratory (Drickamer et al., 1973) and availability of multiple sequenced genomes (Kordonowy et al., 2017, Colella et al., 2020). It is a part of the genus *Peromyscus*, which has been used by North American mammologists for decades as a model organism, leaving in its wake a swath of ecological, genetic and physiological knowledge (Dewey et al., 2001; Bedford et al., 2015; Martin et al., 2007; Weber et al., 2013). The genus *Peromyscus* also includes both desert-adapted and mesic species, making comparative and evolutionary studies between its members possible (Trainor et al., 2006).

Previous Studies Involving Peromyscus eremicus

In past years, Dr. Matthew MacManes at the University of New Hampshire has focused his research on studying the effects of dehydration on *P. eremicus* and their physiological and

genetic adaptations. The MacManes lab has published studies outlining the effects that dehydration has on *P. eremicus'* physiology and biochemistry (Kordonowy et al., 2017), reproductive ability (Kordonowy et al., 2017), and in-depth studies of the kidney under acute dehydration (MacManes et al., 2017). Of specific interest is the latter study, which focuses on transcriptional response to dehydration in renal tissues. This study reported 465 differentially expressed genes in the kidney. Upregulated genes fell into functional categories associated with cellular starvation response, negative regulation of the MAPK cascade, and both positive and negative regulation of apoptosis (MacManes et al., 2017). Modulation of cellular starvation response occurs when cells are deprived of critical nutrients, such as water. However, these pathways do not seem to lead to apoptosis. Genes associated with the negative regulation of the MAPK cascade have been known to inhibit the production of V2 vasopressin receptor signaling, which would slow down urine concentration and production, leading to a retention of vital water within the organism. Regulation of apoptotic pathways is an important part of cellular function, and the ability to negatively regulate apoptosis in a state of dehydrative stress would be pertinent to avoid vital organ damage.

The 2017 MacManes study also examined the role of AQP genes in dehydrated mice. In many past studies, the AQP family was thought to play a large role in desert adaptation to dehydration (Cortes et al., 2000; Giorello et al., 2018; Kordonowy et al., 2017; Marra et al., 2012). However MacManes et al. 2017 reported that the only AQP gene found to be differentially expressed was AQP4, which showed a decrease in expression than that of the control group. The hypothesis presented was that lower expression may be related to the reduced water available for movement, and therefore the need for such protein complexes is reduced. When looking at genes that deal with regulating sodium in serum, they found AVPR2 and

SLC8A1 to be differentially expressed, but both were more highly expressed in control animals. AVPR2 is a vasopressin receptor that is linked to sodium excretion, and SLC8A is a sodium/calcium exchanger. The latter is a part of the solute carrier group expected to be intimately equated with desert animal adaptation. The area of sodium management is hypothesized to be very complex, and understanding the different roles that gene families play within the different regions of the kidney may unlock a deeper understanding of these adaptations (MacManes et al., 2014).

Utilizing Spatial Transcriptomics Within Peromyscus eremicus

In the past, kidney samples from rodents have been analyzed via RNA-seq, using either bulk RNA (MacManes et al., 2014; MacManes et al., 2017; Giorello et al., 2018; Marra et al., 2012), or single-cell techniques (scRNA) (Park et al., 2018). While these techniques have proven invaluable and have help uncover many functions and cellular workings within the kidney, the process of extracting RNA requires manipulation of tissue, including cellular dissociation, which results in the loss of spatial information (Wu et al., 2017; Lee et al., 2015). In recent years, a new technique has become available in hopes to bridge the gap between spatially resolved information and RNA-Seq technology. Spatial transcriptomics (ST) integrates histological slides of the tissue of interest with RNA-seq based technology. Oligo-dT spots embedded on the slide surface capture the release of any polyadenylated RNA from the tissue of interest, allowing the mRNA to be utilized for library preparation and sequencing. The gene expression is then placed on top of the histological image, and spatial gene expression can be explored (Ortiz et al., 2020, Stahl et al., 2016; Raghubar et al., 2020).

While some rodent studies have started utilizing the ST platform to build spatial atlases for different tissues (Raghubar et al., 2020; Ortiz et al., 2020; Dixon et al., 2022), no studies

involving *Peromyscus eremicus* have integrated such technology. The implications of using this technique have already been speculated by MacManes et al. 2017 to provide necessary spatial information to understanding the complexity of sodium regulation. The building of a spatial atlas can also provide a deeper understanding of cell distribution and location, spatial gene expression patterns, and to lay the groundwork for ST-seq studies on mice subjected to acute dehydration.

Objectives and Aims

The overall goal of this project was to create a spatial atlas of the kidney of *Peromyscus eremicus* and provide information on differential gene expression, cell type distribution, and spatial cluster definition. Specific objectives were to:

1. Use defined cell marker genes from literature to deconvolute and define cell types in *P. eremicus* kidney tissue.
2. Define spatially resolved clusters in *P. eremicus* tissue by cell type, differential gene expression, and location (cortex, medulla, etc.).
3. Explore location and expression of genes previously considered important in desert adaptation.
4. Explore patterns of differential gene expression across the entirety of kidney sections.

The resulting data and atlas of the kidney sections of *P. eremicus* will allow future researchers to explore gene expression in a spatially robust format and make hypotheses on desert adaptations within the model. This project also opens the door for a study utilizing the ST platform to compare morphological and genetic differences between *P. eremicus* mice with and without exposure to acute dehydration. Integrating spatial information is pertinent to

understanding and applying information gained about desert adaptation to the clinical response of dehydration in humans, who are perilously sensitive to the effects of dehydration.

CHAPTER TWO: A 10X VISIUM ANALYSIS OF *PEROMYSCUS EREMICUS*: A SPATIAL APPROACH TO RNA-SEQ

INTRODUCTION

Over one third of the surface of earth is classified as arid and over 2.1 billion people inhabit deserts or drylands annually (Osborne et al., 2020). While arid landscapes offer a myriad of challenges, the greatest of these challenges is water scarcity. Water is essential to all forms of life, and significant deleterious effects have been observed when prolonged dehydration occurs (Chapman et al., 2021). In humans, mild dehydration can result in significant renal derangement through dehydration-linked electrolyte imbalance (Nose et al., 1988). Acute kidney injury (AKI) has been closely linked with moderate dehydration, and if left untreated can result in death (Johnson et al., 2016). Even if AKI is caught early and treated, new studies have found that AKI may result in chronic kidney disease (CKD), which affects upward of 800 million individuals worldwide and is the 16th cause of loss of life worldwide (Chen et al., 2019). Indeed, humans and traditional mammalian models walk a fine line maintaining electrolyte balance while under limited water conditions.

Conversely, desert-adapted mammals have been evolving in these arid conditions for millions of years (Rocha et al., 2021) and seemingly do not suffer the same consequences following limited water availability and intake. Evolutionary adaptations in phenotype have allowed these mammals to survive these conditions through behavioral (Blumstein et al., 2022), morphological (Gallardo et al., 2005), and physiological changes (Colella et al., 2021; Tigano et al., 2020; Kordonowy et al., 2017, MacManes et al., 2017; MacManes et al., 2014). Additionally,

studies have shown that these mammals have genetic adaptations that provide specialized machinery to manage solute balance during states of dehydration (Zhang et al., 2019; Giorello et al., 2018; Pannabecker et al., 2015; MacManes et al., 2017; MacManes et al., 2014; Gallardo et al., 2005; Gallardo et al., 2002). The aquaporin (AQP) protein family, which helps provide maintenance of water balance in the kidney (Liu et al., 2003), and the solute carriers, which aids in the transport and maintenance of electrolytes for daily function (Pizzagalli et al., 2021), have both been found to be differentially expressed in desert mammals (Marra et al., 2012; Marra et al., 2014; MacManes et al., 2017). Since dehydration results in a hyperosmolar state, electrolyte imbalance is a common challenge that desert animals have to overcome (Takei et al., 2012). Utilizing highly adapted mechanisms such as the AQP's water shunting ability and solute carrier's ionic transport may be at least in part one way that these desert mammals combat the effects of dehydration.

Dehydration in non-desert-adapted mammals results in the alteration of cell volume via hyperosmolarity (Nugent., 2005). When cells experience this change in state, they experience a range of deleterious effects, such as oxidative stress, halting of cellular metabolism, cell cycle arrest, and apoptosis (Nose et al., 1988). When severity of dehydration increases, damage to cellular mechanisms also increases. However, desert-adapted mammals are under constant hyperosmolar stress, and would have had to evolutionarily adapt to persist. Studies have shown that desert mammals, specifically desert rodents, have decreased signals of cellular stress, unfolded protein response, and apoptosis under acute dehydration (MacManes et al., 2017; Marra et al., 2014; Giorello et al., 2018). Due to their environment, many of these desert rodents have very limited water intake. *Peromyscus eremicus*, also known as the cactus mouse, is one of these rodents. Endemic to the southwestern area of North America, this rodent may go its entire life

without consuming water and often goes without urinating, but seems to not incur any persistent renal dysfunction (Kordonowy et al., 2017). *P. eremicus* has been studied both for its response to dehydration and due to the characteristics it shares with other well established model organisms, including its ability to be reared in the laboratory (MacManes et al., 2017) and the availability of sequenced genomes (Collela et al., 2020). These key features make *P. eremicus* an excellent candidate for studying physiological and genetic adaptations to dehydration that may help elucidate clinical treatments for renal impairment due to dehydration.

In past studies, kidney samples from desert and non-desert mammals have been studied by employing Next Generation Sequencing (NGS) techniques such as bulk (MacManes et al., 2017; Marra et al., 2014; Kordonowy et al., 2017; Giorello et al., 2018; Park et al., 2018) and single cell RNA-seq (Dumas et al., 2020). While these studies have uncovered many adaptations and differential expression patterns that have helped define dehydration related responses, the tissue itself is manipulated and the cells dissociated, resulting in a convolution of spatial information that may be crucial to understand cellular interaction and gene expression. To help provide this key piece of data, 10X Genomics has devised a Spatial Transcriptomics (ST) platform, termed Visium, that allows the user to combine the powers of single cell sequencing with histological practices to allow for spatially resolved understanding of gene expression (Ortiz et al., 2020, Stahl et al., 2016; Raghubar et al., 2020). Using a glass slide embedded with spatially barcoded spots, tissue sections can be stained, imaged, and then denatured to release mRNA that then can be sequenced and transcribed back onto the resulting image, providing a spatially accurate gene expression matrix (Asp et al., 2020). Utilizing this ST platform, the goal of this project was to generate a spatial atlas of *P. eremicus* kidney in hopes to provide crucial information about cell type, location, and spatially explicit differential gene expression, along

with establishig the framework for future studies involving dehydration experiments that utilize the ST platform.

METHODS

Tissue sectioning

Mice selected for this study were from a captive colony of cactus mice held at the University of New Hampshire. Two male and two female mice were euthanized with an overdose of isoflurane followed by decapitation. The kidneys were then prepared according to 10X guidelines. Specifically, kidneys were extracted from the body cavity and placed in 2 mL collection tubes, which within 2 minutes were placed on dry ice to halt tissue degradation. The kidneys were then slowly thawed, and excess moisture was blotted off. The whole kidneys were then embedded in Optimal Cutting Temperature compound (OCT) and frozen in isopentane (2-methylbutane, Sigma) on dry ice. Once frozen, OCT blocks were kept at -80 ℃ until sectioning. For sectioning, OCT blocks were equilibrated to -18 ℃ for 30 minutes and then sliced into 10-μm sections on a cryostat at -16℃ (Leica CM3050 S, Leica). Sections were mounted onto spatially barcoded arrays (6 mm x 6 mm) manufactured by 10X Genomics, one section per well. Capture area A1 and B1 were both male kidney slices, one slice per mouse. Capture area C1 and D1 are both female kidney slices, one slice per mouse (Figure 2-1). Slides were then stored at -80 ℃ until the time of spatial library preparation. All animal care procedures were conducted in accordance with the University of New Hampshire Animal Care and Use Committee guidelines and the guidelines established by the American Society of Mammologists (Sikes et al., 2011). Animal care procedures, including housing conditions, euthanasia, and tissue collection procedures, were approved by the University of New Hampshire Animal Care Use Committee (protocol number 210602).

Fixation, Staining, and Imaging

The kidney sections were fixed to the slide by incubating in methanol (Sigma) for 30 minutes at -20℃. To perform the hematoxylin and eosin (H&E) staining of the tissue, the sections were incubated in Mayer's Hematoxylin (Electron Microscopy Sciences, Hattfield, PA) for 7 minutes, Bluing buffer for 2 minutes, and Eosin (Sigma-Aldrich) mix for 1 minute. After drying, the tissue sections were imaged and stitched together using the EVOS FL Auto 2 platform (Thermo Fisher Scientific, Waltham, MA) on 20X magnification with the DAPI filter selected. Images were visualized and were each extracted as a .tiff.

Tissue Optimization and Permeabilization

Prior to beginning the experiment on the Gene Expression Slide (GES) used for the data generated in this study, a tissue optimization experiment was required to find out the optimal permeabilization time for the specific tissue sectioned. Seven tissue slices were placed, fixed, and stained as described above on the Tissue Optimization Slide (TOS), with one capture area left empty for positive control (see fig 2-1). Two µl of positive control RNA obtained from prior lab RNA extractions on kidney tissue were placed in capture area A1. 70 µl of permeabilization enzyme were added to capture areas B1-C2 (figure X) following an incubation time course that would allow specific permeabilization times to be tested. The times tested were 30 minutes (B1), 24 minutes (C1), 18 minutes (D1), 12 minutes (A2), 6 minutes (B2), and 3 minutes (C2), all incubated at 37℃. A negative control (D2), which did not receive any permeabilization enzyme but did include tissue, was included in this test. Following permeabilization, a fluorescent RT master mix was used to synthesize the complementary cDNA strand, and the tissue was chemically removed from the slide and fluorescently imaged using the EVOS FL Auto 2 platform (Thermo Fisher Scientific, Waltham, MA) on 20X magnification and with the RFP filter

selected. Once an optimal permeabilization time was determined, it was applied to the GES slide. Tissue sections were incubated at 37℃ for 18 minutes following the addition of 70 µl of permeabilization enzyme. Cells were then washed using 100 µl of 0.1X SCC (Thermo Fisher Scientific).

Figure 2-1: 10X Visium Slide layouts

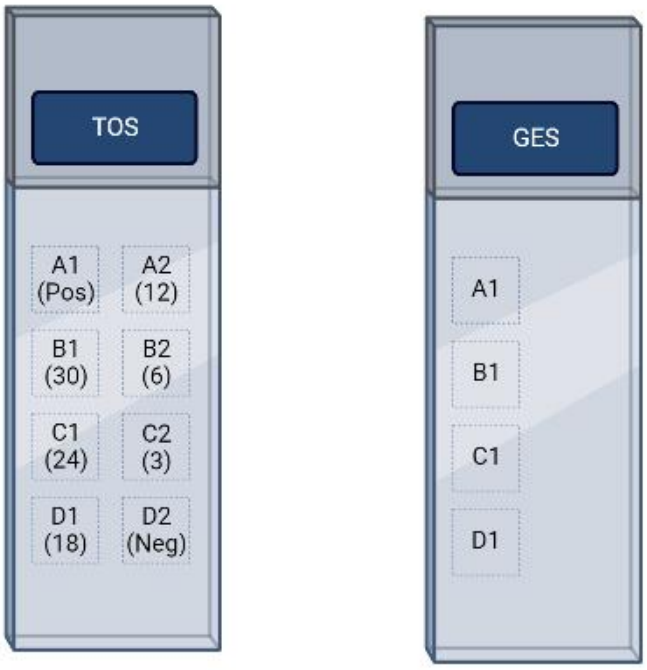

Figure 2-1: Layout of 10X Visium tissue optimization slide (TOS) on the left and gene expression slide (GES) on the right. TOS slide shows time point layouts for permeabilization optimization experiment (B1 = 30 minutes, C1 = 24 minutes, D1 = 18 minutes, A2 = 12 minutes, B2 = 6 minutes, and C2 = 3 minutes), along with control layout (A1 = positive control, D2 = negative control). GES slide layout outlines placement and naming (A1-B1 = male slices, C1-D1 = female slices). Image created with BioRender.com

Reverse Transcription and Library Preparation

After permeabilization, 75 µl of reverse transcription (RT) master mix was added to each of the four wells of the GES slide and incubated at 53℃ for 45 minutes. Next, second-strand synthesis, cDNA synthesis, fragmentation, end repair, A-tailing, adaptor ligation, and sample indexing were performed following 10X Visium manufacturer's instructions (PN-1000187, lot no. 200403, Rev

F). The quality and size distribution of the resulting libraries were characterized using the Agilent Bioanalyzer High sensitivity kit (Agilent, Santa Clara, CA), and quantity was measured via Qubit ds-DNA HS assay (Thermo Fisher Scientific).

Sequencing and Initial Processing

Spatial sequencing libraries were sequenced on a NovaSeq 6000 according to 10X Genomics Visium manufacturer's instructions (PN-1000187, lot no. 200403, Rev F), targeting 50,000 reads per spot and averaging 150 million reads per sequencing array using 150-bp paired end sequencing. A reference GTF file was assembled using gffread (https://github.com/gpertea/gffread) using the annotated genome and transcriptome references of *P. eremicus* generated by the MacManes Lab and DNAZoo (https://dnazoo.s3.wasabisys.com/index.html?prefix=Peromyscus_eremicus/). The resulting GTF, along with the *P. eremicus* annotated genome, was used to generate a reference package using SpaceRanger's *mkref* feature (spatial 3′ v1; spaceranger-1.2.1). Then the reference package, FASTQ sequencing files, and H&E images were run through SpaceRanger *count*, where the data was normalized. Space Ranger output files were initially viewed in 10X Genomics Loupe Browser to visualize UMAP and tSNE plots, as well as preprocessed spatial clustering onto sample images.

Data Processing

Due to the limitations of the 10X Genomics Loupe Browser, such as only being able to visualize one gene at a time, the images and corresponding sequencing files were loaded into Seurat (http://satijalab.org/seurat/; Hao et al., 2021; Stuart et al., 2019; Butler et al., 2018, Satija et al., 2015) and BayesSpace (https://github.com/edward130603/BayesSpace; Zhao et al.,

2020). All statistical analyses were conducted in R Statistical Software (V 4.2.3; R Core Team 2021) and R Studio (Version 2023. 03) unless otherwise specified. All scripts used in this project are available through GitHub at: https://github.com/molkep/10X-Visium-pero-Kidney-Thesis.

Seurat

The spatial objects were loaded into Seurat (Version 4.9.9.9039) in R Studio (Version 2023. 03). *SCTtransform* was used to normalize each of the samples, and results of the clustering of this data were visualized using *DimPlot* for UMAP space and *SpatialDimPlot* for clustering directly onto the sample image. Initial exploration of the data followed a modified version of the Seurat Spatial workflow (https://satijalab.org/seurat/archive/v3.2/spatial_vignette.html). Differentially expressed genes (DEGs) were generated using Seurat functions, and gene ontology (GO) analysis of the DEGs were performed using g:Profiler (https://biit.cs.ut.ee/gprofiler/; Reimand et al., 2007).

BayesSpace

Previously generated Seraut data objects were transformed into workable BayesSpace (Version 1.1.4) datasets. Data was pre-processed using their *spatialPreprocess* function, which log normalizes the count matrix and performs a PCA on the top highly variable genes while keeping the principal components. Top highly variable genes are enerated by comparing the log2 fold change of genes between the clusters and determining spatially variable regions of expression. Using their function *qTune*, the cluster number was calculated to use in analysis. This function calculates the average pseudo-log likelihood and is plotted using *qPlot*, where the number of clusters selected should be around the elbow of the graph. Data was clustered based on these calculations and visualized on the sample images. Bayesspace uses Bayesian statistical methods

of spatial neighborhoods to enhance the resolution of clustering analyses by introducing subspot level deconvolution. This subspot integration helps smooth out noise and sparsity that may exist within the datasets and helps to display gene expression more accurately across the tissue. These enhanced plots were used to examine cell type distribution across the renal tissue via established gene markers from previous literature (Balzer et al., 2022; Park et al., 2018; Clark et al., 2019).

RESULTS

Library Prep Results Including Sectioning Permeabilization:

Seven slices of male kidney were prepped for permeabilization time determination as described above. When examining the fluorescent image of the slide (fig 2-2), the brightest time point, indicating the optimal permeabilization time, was deemed to be 18 minutes. This time point was used in the completion of library preparation for the gene expression slide (GES).

Figure 2-2: Result of Fluorescent Imaging of Tissue Optimization Slide

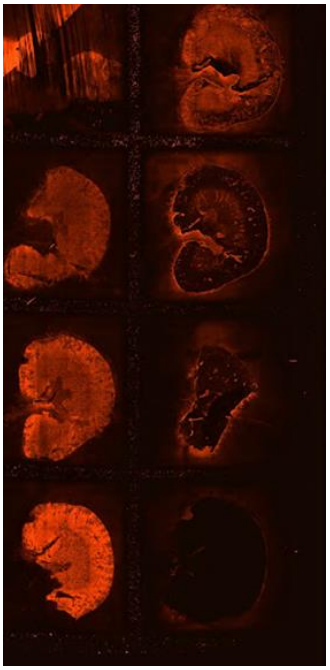

Figure 2-2: Fluorescent imaging of the tissue optimization slide for *P. eremicus* kidney tissue. Top Left (A1) is positive control, B1 was the 30-minute time mark, C1 was 24 minutes, D1 18 minutes, A2 12 minutes, B2 6 minutes, C2 3 minutes, and D2 was a negative control. Time frame 18 minutes was chosen for the permeabilization time due to the strength of fluorescence.

A total of four kidney sections (n = 2 male, n = 2 female), were cryosectioned coronally to expose major physiological regions and place onto the tissue capture area of the 10X Visium glass GES slide embedded with spatially barcoded oligo sequences. Library preparation protocols were followed according to 10X Genomics Visium manufacturer's instructions (CG-000239, lot no. 200403, Rev F). Concentrations of each slide well library were recorded as A1: 4.94 ng/µl, B1: 5.96 ng/µl, C1: 3.99 ng/µl, D1: 24.5 ng/µl.

Sequencing Results and Statistics

Forward and reverse Raw FASTQ files for each gene expression slide capture area were run though the Space Ranger Count pipeline for processing and to generate spatial feature counts. Raw reads can be found at the BioProject ID PRJNA989595. Each capture area was run

individually and generated a summary HTML file that gives statistics for the library. For capture area A1, 3,146 spots were under the tissue, with 177,091 mean reads per spot and 1,305 median genes per spot. A total of 557,127,407 reads were generated, and a total of 11,887 genes were detected. Capture area B1 had 3,534 spots under the tissue, with 146,168 mean reads and 1,192 median genes per spot, for a total of 516,558,794 generated reads and 11,701 total genes detected. Capture area C1 reported 3,050 spots under tissue, with 167,216 mean reads and 1,157 median genes per spot. A total of 510,008,993 reads were generated, with 11,166 total genes detected. Capture area D1 reported 2, 931 spots under tissue, with 205,362 mean reads and 1,344 median genes per spot. A total of 601,915,070 reads were generated, with 11,845 total genes detected. While tissue section D1 outperformed section A1 in total reads and genes, Tissue A1 covered more spot areas than D1. Higher reads and gene expression may also be attributed to a higher starting concentration for the library prior to sequencing, as the concentration for D1 was almost five-fold the amount for A1. Upon further exploration of cluster definition and histological relevance, Tissue A1 more clearly defines understood regions of kidney architecture, and clear clustering can be observed in A1 versus D1 by comparing UMAP plotting between the two tissue samples (Fig. 2-3). For these reasons, the analysis and results described in this study will focus on tissue section A1, with supplementary figures and data supplied for all other tissues.

Figure 2-3: UMAP Plotting of Spatial Clusters

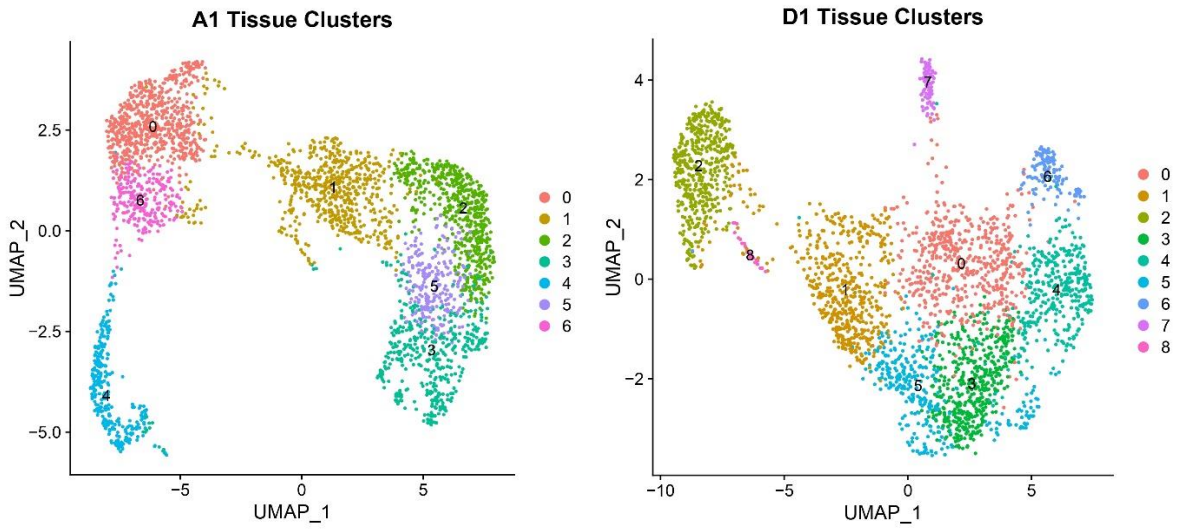

Figure 2-3: UMAP plotting of the spatial clusters defined by Seurat package. Tissue A1 (male) UMAP is on the left, while tissue D1 (female) is on the right.

Assessing Spatial Libraries in Seurat

Using Seurat, we identified spatial organization within the kidney by first defining neighborhoods of cells with similar feature expression patterns. This is done by constructing a K-nearest neighbor (KNN) graph based on Euclidean distance in PCA space, and then the edge weights between any two cells are refined based on Jaccard similarity. The Louvain algorithm is used to iteratively groups cells together and are then mapped back onto the H&E-stained tissue (Fig 2-4a, Figure 2-4b). Seurat returned 7 uniquely defined clusters for tissue A1, numbered 0-6 (Figure 2-4a). While clusters and cell type are not directly correlated in this analysis, cell type patterns have been observed within the clusters.

Figure 2-4: A1 Kidney Tissue Spatial Cluster Visualization, Breakdown, and Top 10 Gene Expression

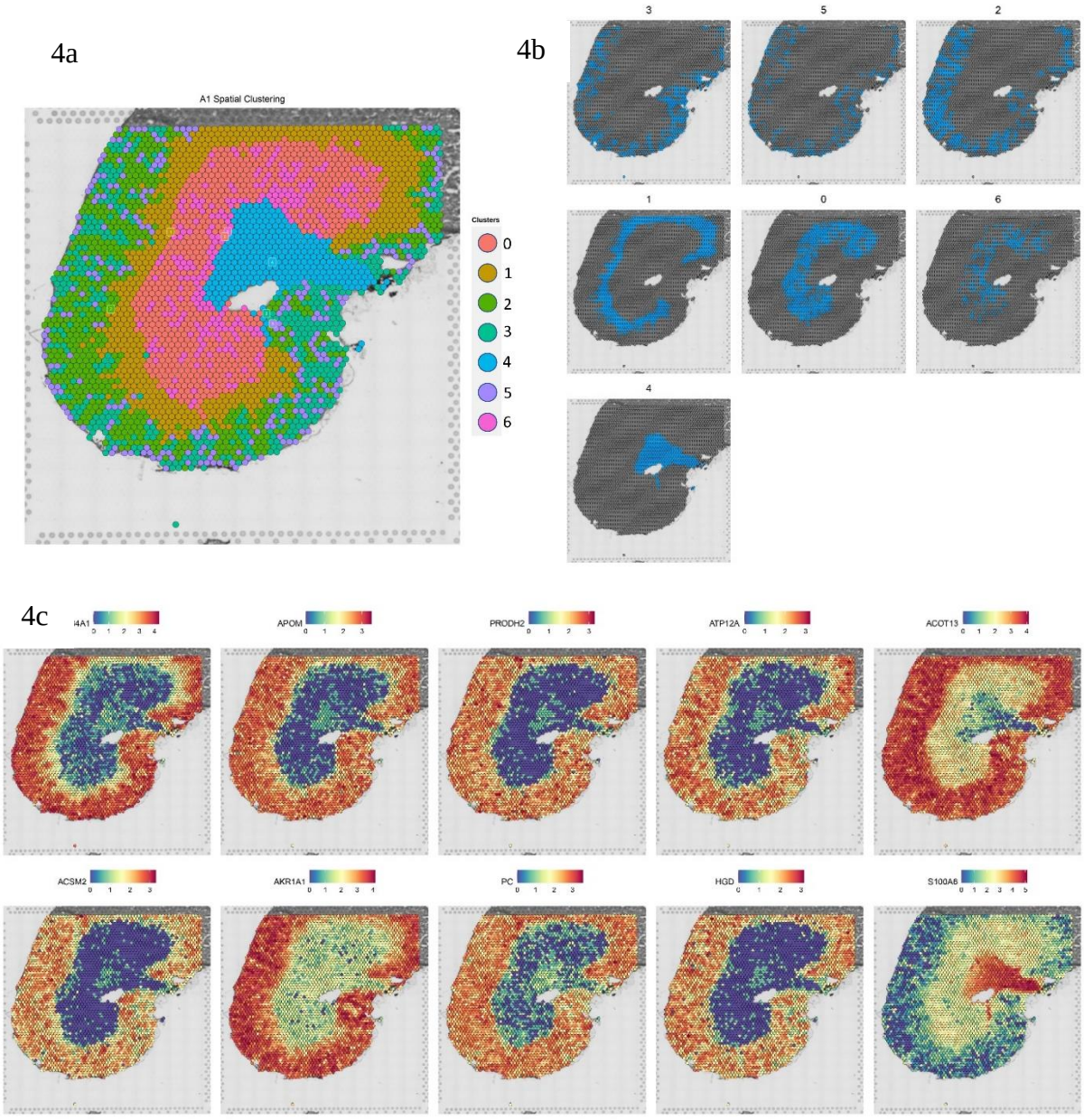

Figure 2-4: Spatial Processing of A1 Tissue Section. 4a (top left) shows Seurat defined clusters projected on top of histological tissue image. 4b (top right) shows individual clusters projected back on to histological image for more direct understanding of cluster definition. 4c (bottom) is a spatially rendered heat map of the top 10 most spatially varialble genes (SLC34A1, APOM, PRODH2, ATP12A, ACOT13, ACSM2, AKR1A1, PC, HGD, and S100A6) and their log normalized expression value.

The top 10 highly variable genes were calculated using the Mark Variogram method, which was inspired by Trendsceek (Edsgärd et al., 2018), where spatial data is modeled as a mark point, which is the measured dependence between two points in a defined distance apart. It then identifies genes whose expression level is dependent on their spatial location from the marked point value (Fig 2-4c) (Stoyan et al., 2000). When the top ten highly variable genes were plotted, clearer patterns of cell distribution were observed. Using established marker genes from previously published single cell analysis literature (Clark et al., 2019; Park et al., 2018; Balzer et al., 2022), cluster associations of cell types were visualized (Proximal tubule: GLYAT, UPB1, and SLC5A2 (cortex), loop of Henle: CDN19 (medulla), Renal pelvis: AKR1B1)

Figure 2-5: Cortex Marker Gene Visualization

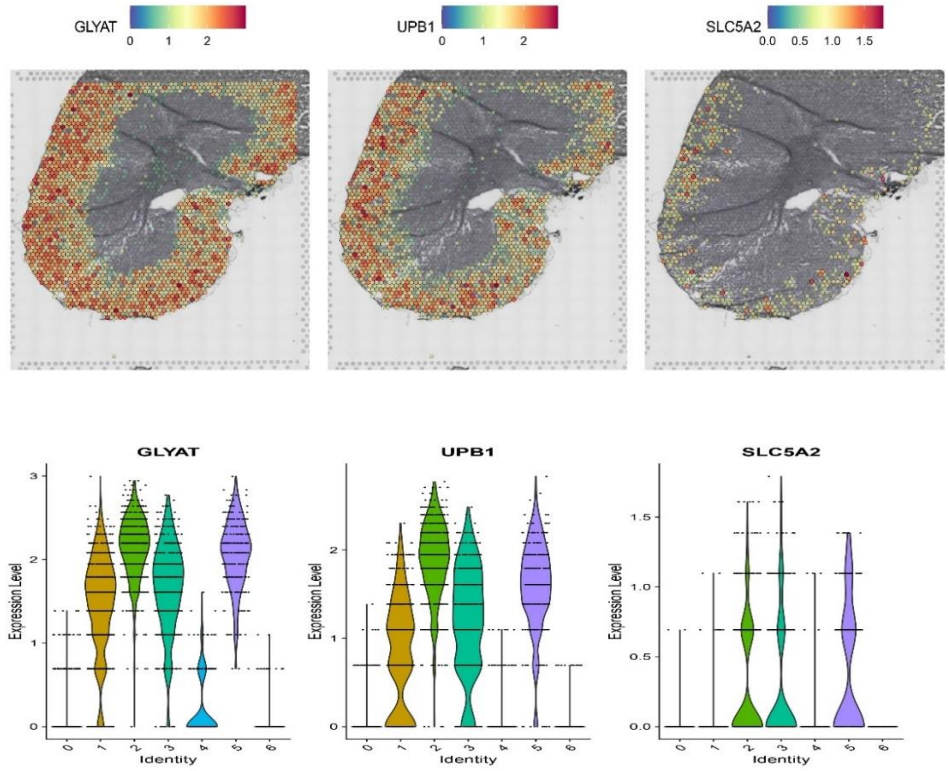

Figure 2-5: Spatial visualization of cortical (proximal tubule) marker genes GLYAT, UPB1, and SLC5A2. Spatial plots and correlating violin plots show gene expression location (top) and log normalized expression per cluster (Bottom). Y-axis is the log normalized expression level, and each dot represents a spot within the cluster. X axis position is arbitrary.

Figure 2-6: Visualization of Medullary Marker Genes

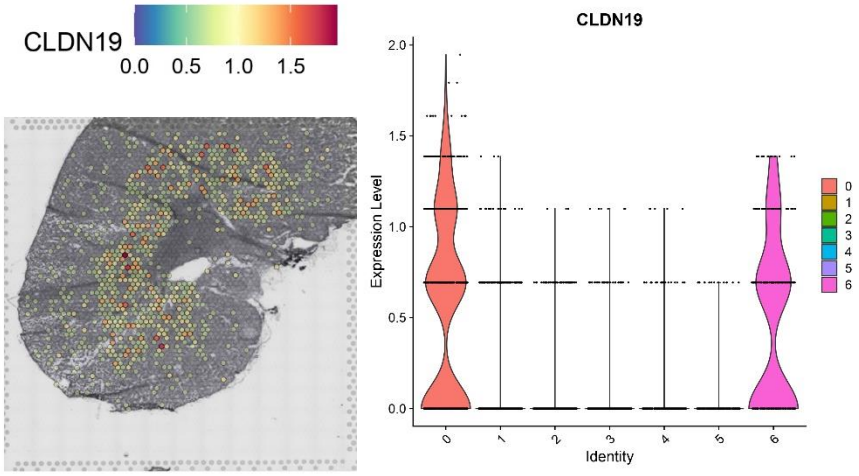

Figure 2-6: Spatial visualization of medullary (loop of Henle) marker gene CLDN19. Spatial plot (left) shows location of expression, and violin plot (right) shows log normalized expression per cluster. Y-axis is the log normalized expression level, and each dot represents a spot within the cluster. X axis position is arbitrary.

Figure 2-7: Visualization of Renal Pelvis Marker Gene

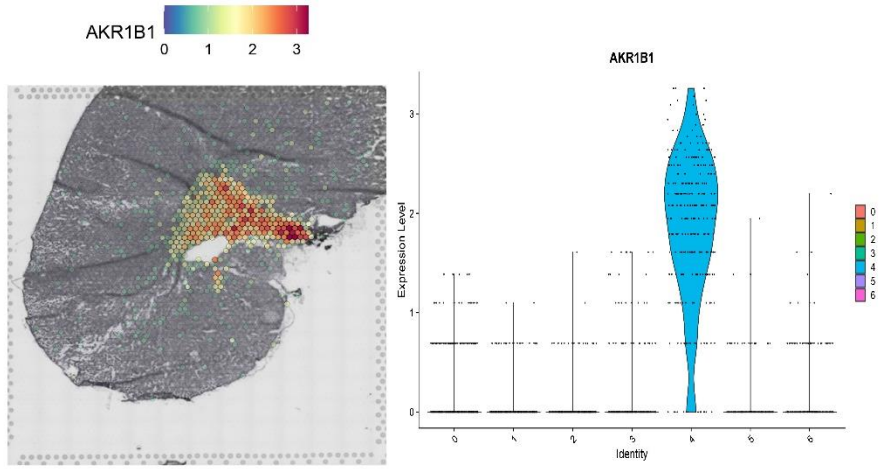

Figure 2-7: Spatial Visualization of renal pelvis marker gene AKR1B1. Spatial plot (left) shows location of expression, and violin plot (right) shows log normalized expression per cluster. Y-axis is the log normalized expression level, and each dot represents a spot within the cluster. X axis position is arbitrary.

Clusters 3, 5, and 2 tended to express genes at a similar level and fall into the established area of the renal cortex, while clusters 0 and 6 express a separate set of genes and fall into the established area of the medulla (Fig 2-5, Fig 2-6). Cluster 1, while often expressing similar genes

as cluster 3, 5 and 2, does not always express the same genes as these clusters, as seen in SLC5A2. It can also be noted that cluster 4 displays a unique gene expression pattern than that of the other two identified cluster regions, which is especially prominent when observing gene expression of S100A6 (Fig 2-4c) and AKR1B1 (fig 2-7).

Exploring Cell Markers using BayesSpace

To increase resolution in between spots and to smooth out subspot expression data, the computational program BayesSpace was utilized. We applied the BayesSpace workflow onto our 10X Visium data to achieve spatially enhanced clustering that could be projected back onto the H&E-stained histological images. We then used defined gene markers from previous single cell literature (Clark et al., 2019; Park et al., 2018; Balzer et al., 2022) to identify cell types (Table 2-1) and used the spatially enhanced plots to show defined cell type regions within the tissue via their log-normalized expression (Figure 2-8).

Table 2-1: Gene Markers by Cell Type

Cell Type:	Gene Markers:
Endocyte (Endo)	*ENG, PLAC8, TSPAN8, KDR, ETS1, PROX1*
Podocyte (Podo)	*NPHS1, NPHS2, CD2AP*
Mesangial Cells (Mes)	*FN1, PAWR, PTN, SERPINE2*
Proximal Tubules (PT)	*AGXT2, CYP2E1, CRYL1, GLYAT, SORD, PDZK1, UPB1, SOD3, HNF4A*
Connecting Tubules (CNT)	*CALB1*
Loop of Henle (LOH)	*SLC12A1, UMOD*
Distal Connecting Tubules (DCT)	*FETUB, PCOLCE, SGCA, SLC12A3*
Collecting Duct: Principal Cells (CD-PC)	*ACER2, AQP3, AQP4, AVPR2, FXYD4, FZD1, PTGES, STC1, TMEM45B, TSPAN1*
Collecting Duct: Intercalated Cells (CD-IC)	*ATP6V1G3, RHCG, ADGRF5, JAG1, INSRR, P2RY14, DMRT2, CLCNKA, AVPR1A, TMEM213, AQP6, ATP6V1B1*
Fibroblasts (Fib)	*COL1A1*
Macrophages (Macro)	*CD68, PPARG*
Neutrophils (Neutro)	*S100A8, S100A9*
B-Lymphocytes (B Lymph)	*SPIB*

Note: gene markers listed do not include genes that were not detected in tissue, and therefore do not represent all marker genes per cell type

Table 2-1: Table of cell type marker genes that were used to define cell type in tissue samples. This table was adapted from information obtained from Clark et al., 2019, Park et al. 2018, and Balzer et al., 2022.

Figure 2-8: Spatial Plotting of Cell Types

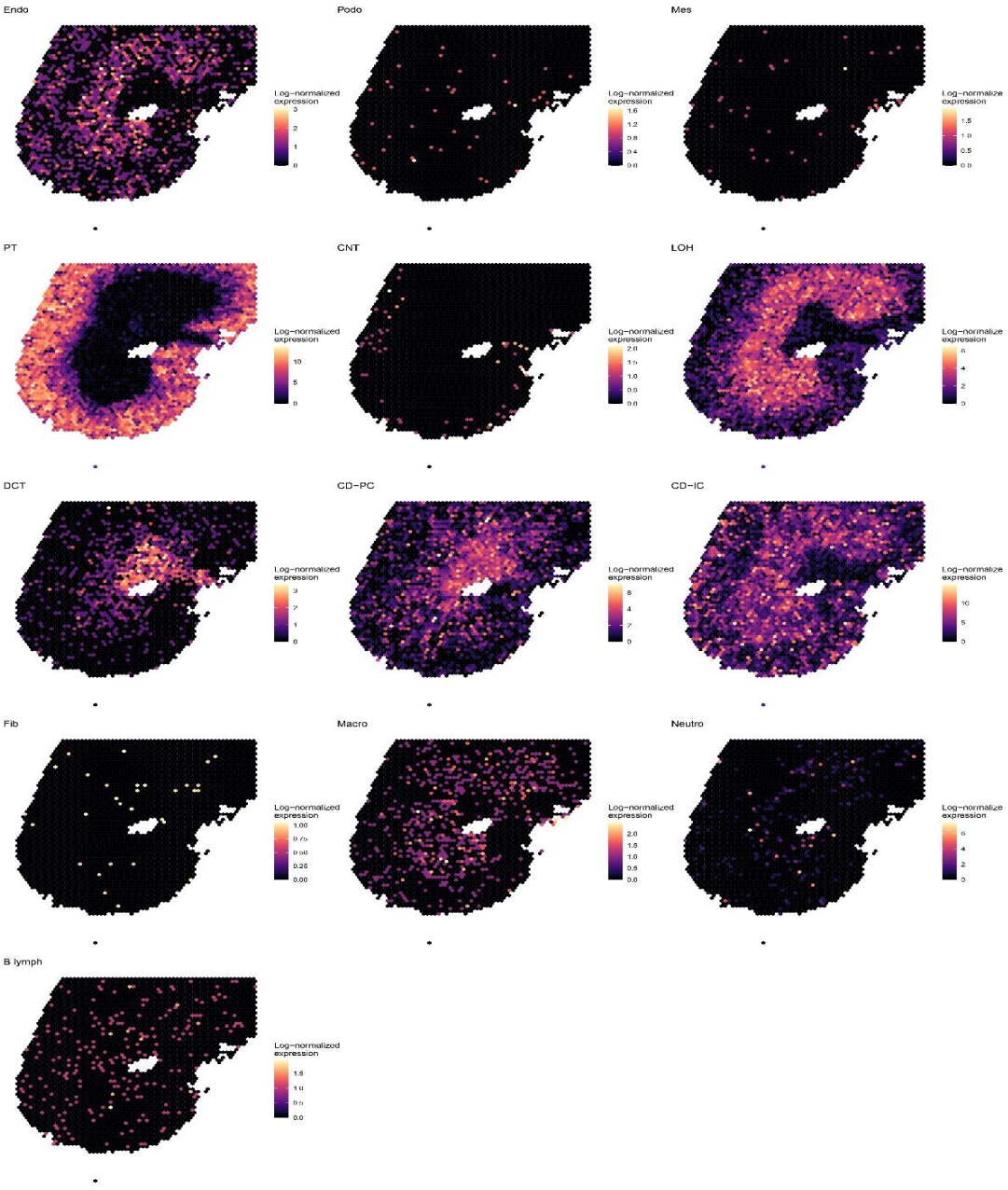

Figure 2-8: Spatially plotted marker gene log normalized expressions for the major cell types recognized in the kidney. Shorthand labels correlate as follows: Endo = endothelial cells, Podo = podocytes, Mes = mesangial cells, PT = proximal tubules, CNT = connecting tubules, LOH = loop of Henle, DCT = distal connecting tubules, CD-PC = collecting duct principal cells, CD-IC = collecting duct interstitial cells, Fib = fibroblast, Macro = macrophage, Neutro = neutrophils, B Lymph = B lymphocytes.

Figure 2-9: Loop of Henle Cell Marker Location and Expression

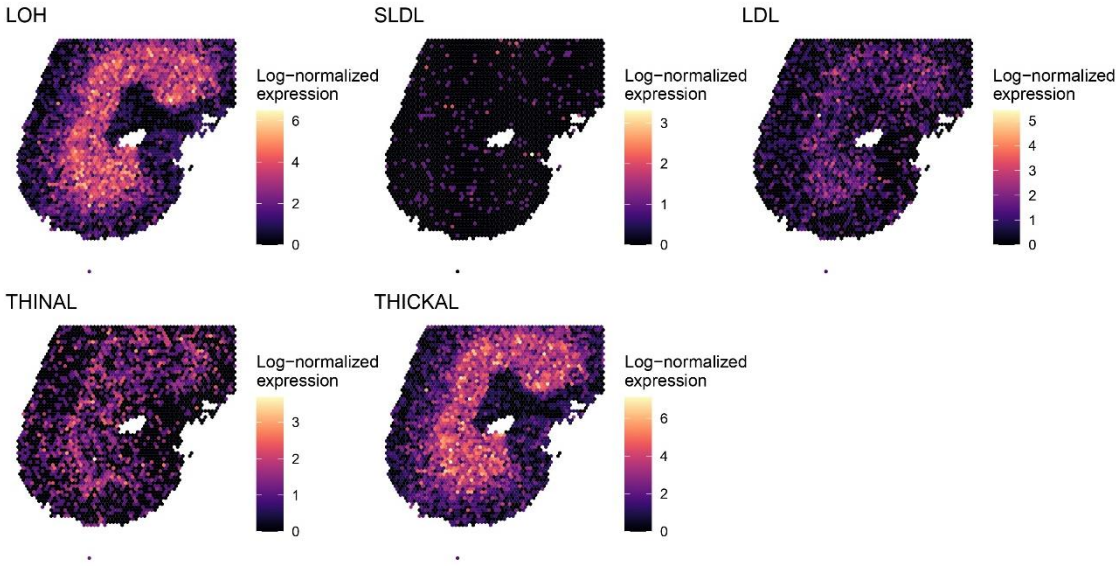

Figure 1-9: visualization of loop of Henle specific cell type markers and their log normalized expression. Shorthand labels correlate as follows: LOH = Loop of Henle (combination of all marker genes), SLDL = short loop descending limb, LDL = long descending limb, THINAL = thin ascending limb, THICKAL = thick ascending limb

Figure 2-10: Proximal Tubule Cell Marker Location and Expression

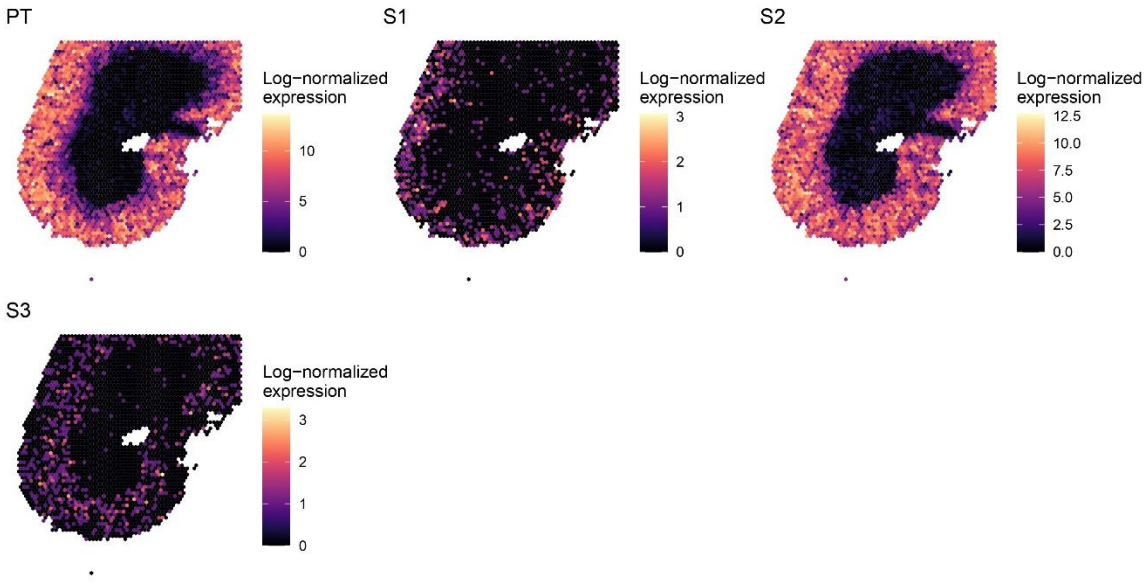

Figure 2-10: Visualization of proximal tubule specific cell type markers and their log normalized expression levels. shorthand labels correlate as follows: PT = proximal tubules (all marker genes), S1 = S1 segment, S2 = S2 segment, S3 = S3 segment

AQP Family Expression

Using expression probability distributions across gene clusters via Seurat, log normalized expression of the aquaporin (AQP) family was assessed. The analysis showed that while AQP 1, 3, 4, 6 and 7 all were expressed within the kidney tissue, only AQP 7 was expressed in an appreciable way, and is observed to be highly expressed in cluster 1 (AvglogFC= 1.56, P-Val = 8.92e-244). AQP genes 2, 5, 8, and 9 were not found to be expressed within our dataset (Fig 2-11).

Figure 2-11: Log normalized expression of AQP Family Genes By Cluster

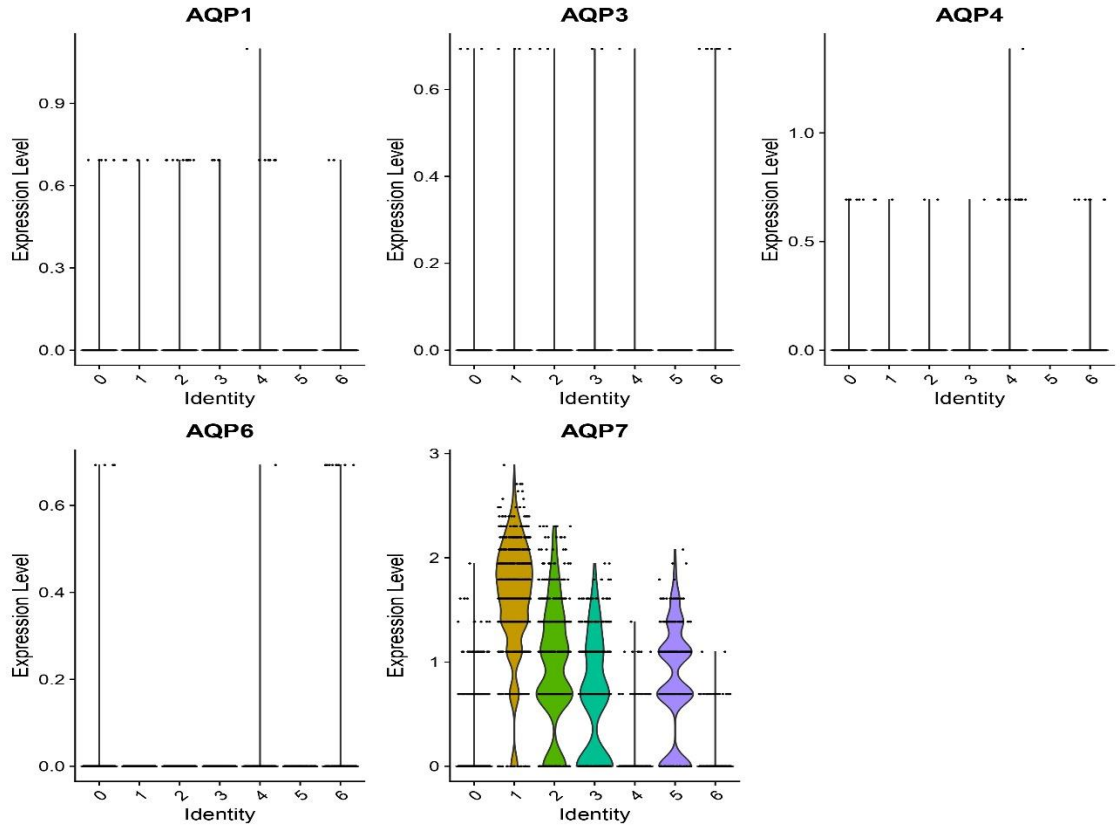

Figure 2-11: AQP gene family log normalized expression by cluster. Y-axis is the log normalized expression level, and each dot represents a spot within the cluster. X axis position is arbitrary. AQP1, AQP3, AQP4, and AQP6 have markedly less expression and distribution among the clusters than AQP7, which shows high levels of abundance in clusters 1, 2, 3 and 5.

Sodium Related Gene expression

Gene expressions of common sodium related genes cited in previous literature (MacManes et al., 2017; Zhang et al., 2019; Konopacka et al., 2015; Marra et al., 2012) were explored in the same manner as described above. High expression values for SCNN1G (sodium channel epithelial 1 subunit gamma), SGK1 (serum/glucocorticoid regulated kinase 1), WNK3 (lysine deficient protein kinase 3), WNK4 (lysine deficient protein kinase 4), and SLC12A1(solute carrier family 12 member 1) are observed across the clusters, with SLC12A1 exhibiting specific expression in clusters 0 (Avglog2FC = .40, P-val = 4.3e-62)and 6 (Avglog2FC = 0.27, P-Val = 1.5e-15). SCNN1G, SGK1, WNK3, and WNK4 show widespread expression throughout all the clusters; however, SGK1 (Avglog2FC = 1.23, P-Val = 1.12e-70) and WNK3 (Avglog2FC = 2.25, P-Val = 2.94e-158) appear to express highest in cluster 4 (Fig 2-12).

Figure 2-12: Log Normalized Expression of Sodium Related Genes by Cluster

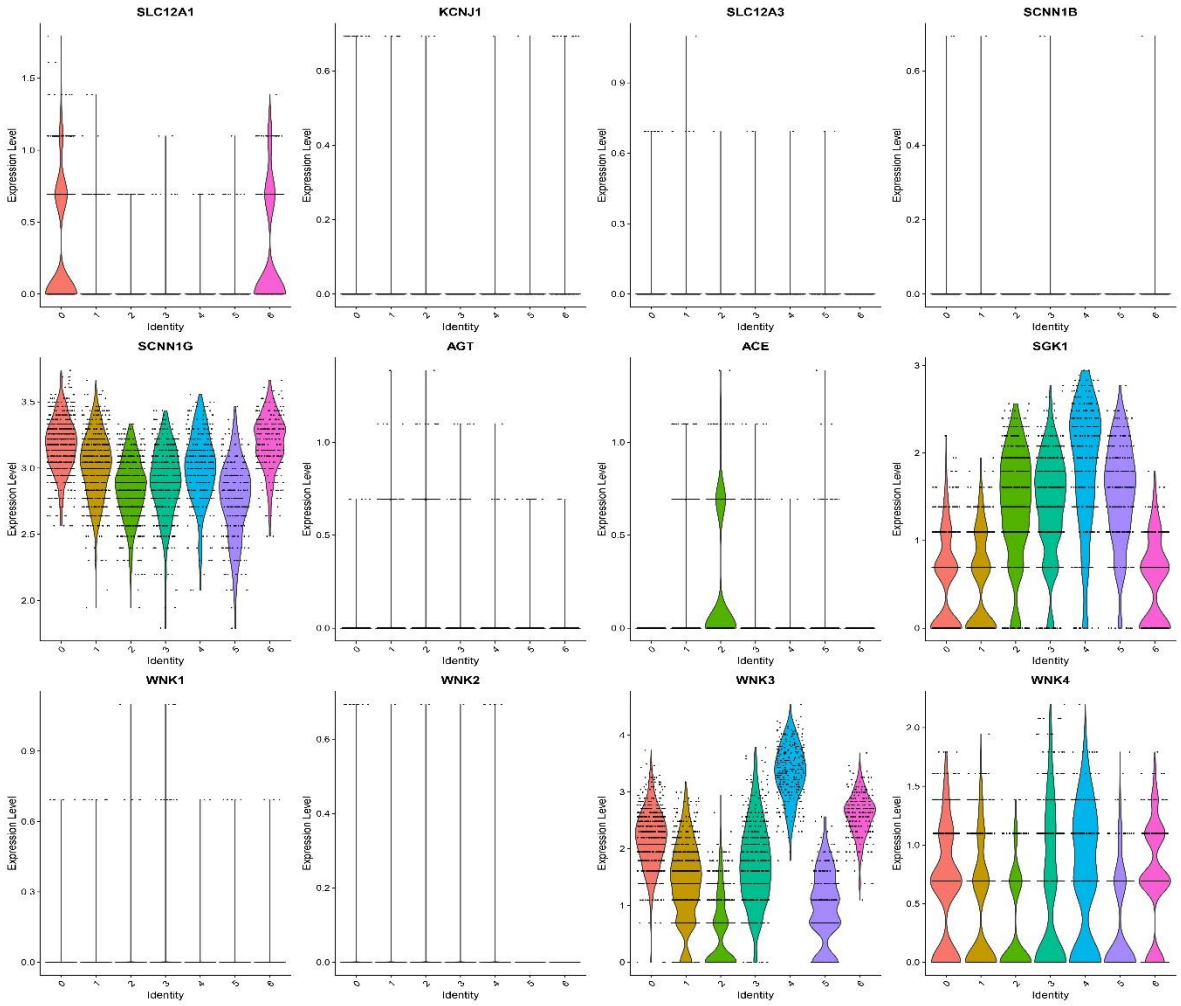

Figure 2-12: Violin plots of log normalized expression levels of sodium related genes by cluster. Y-axis is the log normalized expression level, and each dot represents a spot within the cluster. X axis position is arbitrary. KCNJ1, SLC12A3, SCNN1B, AGT, WNK1, and WNK2 had reduced expression across the tissue clusters compared to SLC12A1, SCNN1G, SGK1, WNK3, and WNK4.

Differential Gene Expression Between Spatial Clusters

To further understand the breakdown between clusters, a differentially expressed gene (DEG) analysis pipeline was run via Seurat. As a default, Seurat performs differential expression based on the non-parametric Wilcoxon rank sum test. The top ten differentially expressed genes

per cluster were highlighted and compared to the log2 fold change of the same genes in the different clusters (Fig 2-13). GO analysis of the top ten genes in each cluster (Table 2-2) was performed using g:Profiler using the provided *Mus musculus* database. Results of the top ten gene GO analysis per cluster can be found in the appendices, and all other supplemental tables can be found at https://github.com/molkep/10X-Pero-erem-Kidney-Thesis-Tables.

Table 2-2: Top Ten Spatially Differentially Expressed Genes by Cluster for Tissue A1

Seurat Defined Clusters of A1	Top 10 Genes
0	*MRPS6, UMOD, PPP1R1A, LDHB, TESC, FABP3, GTR1, GPX2, COX7A1, ECRG4*
1	*SLC6A18, AQP7, SPTBN1, NNMT, KHK, GPM6A, FAH, GGT1, CLES1, PC*
2	*AKR1A1, HSD11B1, ACSM1, FTL2, CYP2E1, RBP2, CTSL, SLC34A1*
3	*KLK1B3, SUSD2, FAM151A, DPEP1, PGAM2, SLC34A1, SLC37A4, SULT1A1, CA15, ATP6V1G3*
4	*AKR1B1, MT3, MT2, PCOLCE, S100A6, CAPG, WNK3, MGP, CRYAB, FXYD4*
5	*SLC34A1, SULT1A1, SUSD2, DPEP1, RBP2, APOM, CYP2E1, SLC37A4, PRODH2, GLYAT*
6	*OPN5, FXYD4, ATP6V1G3, CKMT1, LDHB, TESC, SPTBN2, TMEM213, COX7A1, CLCNKB*

Figure 2-2: Top ten genes per cluster in tissue A1. Gene expression is based on log2 fold change and were generated via Seurat's SpatiallyVariableFeatures function.

Figure 2-13: Heat Map of Spatial Patterning of Differential Gene Expression for A1 Tissue

Figure 2-13: Heat map of the log2 fold change of the top ten genes expressed in each cluster compared to expression values in the other clusters. Duplicate genes are not included in the heatmap, which may reflect in the total number of genes shown. Cluster numbers are shown on the X-axis, while gene names are shown on the Y-axis.

To understand the functions of clusters in comparison to the other clusters defined in our dataset, GO term analyses between clusters were performed. Custom GMT files containing specific GO terms and genes associated were created using a filtering code run on the *Mus musculus* GMT files used previously for general GO term analysis. The resulting files were then uploaded to g:Profiler, and a list of the top most highly variable genes per cluster were each run against each different custom cluster GMT. This resulted in GO Terms that not only define

function of the clusters, but function in comparison to the other clusters. Results from these analyses can be found in the appendices (Appendix XXIV-Appendix XXX), and all other supplemental tables can be found at https://github.com/molkep/10X-Pero-erem-Kidney-Thesis-Tables.

DISCUSSION

Desert adaptation has been well studied in desert mammals (Shmidt-Neilsen et al., 1948; McNab et al., 1963; Hayward et al., 1965; MacManes et al., 2017; MacManes et al., 2014; Wu et al., 2014; Blumstein et al., 2022; Aboul Naga et al., 2021), including that of their kidney function (Ali et al., 2020; MacManes et al., 2014; Marra et al., 2014; Altschuler et al., 1979; Kaißling et al., 1975) and their ability to escape renal failure while experiencing extreme dehydration (MacManes et al., 2017; Kordonowy et al., 2017). While studies exist that examine gene expression across the tissue, until recently, there has been no spatial information that links tissue position to the gene expression observed. In this study, we have generated a 10X Genomics Visium platform spatial atlas of genes expressed in the kidney of *Peromyscus eremicus* under normal hydration conditions in hopes to understand cell type structure and spatial patterns of differential gene expression within the tissue.

Initial Clustering and Spatial Relevance:

While 10x Visium offers excellent sample preparation, analysis pipelines, and basic visualization software via the Loupe Browser, limitations on exploring multiple genes at a time and resolution of cell communities led us to expand our data visualization to the R packages of Seurat and BayesSpace. Seurat allowed us to explore gene families and known markers of desert adaptation by cluster, and BayesSpace helped increase cell resolution by using Bayesian models

and information from spatial neighborhoods to create subspots within the data. While many cell types were able to be defined by prior gene markers, certain cell types such as connecting tubules (CNT), podocytes (Podo), Mesangial cells (Mes), and fibroblasts (Fib), were not able to be highlighted with great distinction (Figure 2-8). Other cell types, such as T-Lymphocytes, could not be defined by known gene markers at all. Both podocytes and mesangial cells are key cell types for the glomerular structures of the kidney, which are the main functional unit for filtration of the blood and formation of primary urine (Ebefors et al., 2022). While *P. eremicus* has been noted to have reduced urinary output (MacManes et al., 2014), blood filtration is still essential to life (Benzing, 2020), and therefore the diminished expression shown in our analysis more likely reflects the need of more specific cell markers to better highlight their distribution.

From these spatial graphs, major cell types of the clusters can be inferred with more confidence due to the highlighted groups of cell marker genes. Clusters 3, 2, and 5 sit well within the defined spatial locations of the proximal tubules, with segment S1 broadly associating with cluster 3 and 5, segment S2 being associated with clusters 3, 2, and 5, and segment S3 being broadly associated with cluster 2 (Figure 2-10). Cluster 1, which shows unique cell type patterns, seems to also associate with segment S2 of the proximal tubules. While the proximal tubules had more defined regions, the loop of Henle, including its constituent parts (thin ascending limb, thick ascending limb, long descending limb, and short loop descending limb) seem to broadly associate with clusters 0 and 6 but extend out to cluster 1 as well (Figure 2-9). Cluster 1 can also be linked to the collecting ducts (Figure 2-8). Cluster 4 is heavily associated with the distal convoluted tubules and partially with the collecting duct principal cells (Figure 2-8).

AQP Gene Family:

It has long been hypothesized that the AQP genes have been critical for the maintenance of homeostasis in desert-adapted animals (Gallardo et al, 2002; Gallardo et al., 2005; Xu et al., 2016; Zhang et al., 2019; MacManes et al., 2017); therefore, they have been heavily studied over the years. Interestingly, our analysis of expression of this gene family returned sparse results. The only gene to show noticeable expression in any of the clusters was AQP7, which has been shown to be abundantly present in the apical membrane of the proximal straight tubules, specifically the S3 segment (Sohara et al., 2006). This corresponds with its expression in clusters 2, 3, and 5, which we demonstrated earlier to have connections to the proximal tubules though cluster analysis and cell type markers. AQP7 has been found to contribute to water permeability of the brush border membrane, and, more importantly, it is intimately involved in glycerol reabsorption of the kidneys (Sohara et al., 2006). Glycerol is important for ATP production through the gluconeogenesis pathway (Gull et al., 2021) and helps create an osmotic gradient that favors water retention (Van Rosendal et al., 2010), which would be highly beneficial for desert-adapted animals.

While it is surprising that the AQP gene class seems to be significantly downregulated in our analysis compared to previous studies (MacManes et al., 2017, Marra et al., 2014), it has been found that increased expression of AQP genes leads to activation of downstream apoptosis cascades, and that lower expressions lead to inhibition of apoptosis (Jablonksi et al., 2007). This diminished expression may be an adaptation help reduce the effect of apoptosis and kidney injury in times of severe dehydration.

Sodium Related Gene Expression:

Water management is closely related to salt concentration and regulation in the body, and one of the most important salts to regulate is sodium. Hypernatremia is often observed in dehydrated animals (Sonani et al., 2023), which makes the balance of serum sodium in desert animals highly important in maintaining normal bodily function (MacManes et al., 2017). Genes associated with sodium pathways were analyzed in this study to understand baseline sodium maintenance strategies of *P. eremicus*. Of the genes detected within the tissue, marked expression levels of SCNN1G (sodium channel epithelial subunit 1 gamma), SGK1 (serum/glucocorticoid regulated kinase 1), WNK3 and WNK4 (lysine deficient protein kinase 3 and 4), and SLC12A1 (solute carrier family 12 member 1) were observed. SCNN1G is part of a family of genes that encode the subunits of the epithelial sodium channels (ENaCs), which are intimately involved with maintaining body salt and water homeostasis (Edelheit et al., 2005). ENaC-dependent reabsorption of sodium in the renal tubules helps regulate extracellular fluid volume and blood pressure via modulation of osmolarity (Hanukoglu et al., 2016). Mutations of these genes have been heavily related to the disease state multi-system pseudohypoaldosteronism type I (PHA), which presents with severe hyponatremia, hyperkalemia, and dehydration (Edelheit et al., 2005).

SLC12A1 encodes for the kidney-specific sodium-potassium-chloride cotransporter (NKCC2) that is responsible for co-translocation of these ions via the apical membrane of the thick ascending loop of Henle (TALH) (Kaplan et al., 1996). The NKCC2 complex can reclaim up to 25% of the ultrafiltered NaCl load, making it extremely important in the maintenance of serum sodium concentration (Marcoux et al., 2021).

While SGK1 and the WNK genes are not directly related to sodium transport or exchange, they encode important kinases involved in the regulation of kidney ion channels

(Verissimo et al., 2001; Noor et al., 2021). WNK kinases connect angiotensin II, aldosterone, and renal sodium and potassium transporters, all of which are directly affected by the dehydration state (An et al., 2022). When the osmotic gradient is disrupted, it triggers the release of angiotensin II, which then activates G protein-coupled angiotensin II receptors (Scott et al., 2023). Among other functions, these receptors release aldosterone, which has the ability to modulate expression and function of renal ion channels, including those that deal with sodium and potassium (Valinsky et al., 2018). WNK3 increases sodium chloride transporters (NCC) and NKCC2 via the SPAK pathway (Oi et al., 2012), and WNK4 works to either to inhibit or upregulate NCC depending on the level of Cl^-; when low chloride is detected, WNK4 is phosphorylated through the SPAK pathway and works to positively regulate NCC, while under high Cl^-conditions, WNK4 cannot be phosphorylated and therefore inhibits NCC (Hanukoglu et al., 2016, An et al, 2022). WNK4 also works to activate the ENaC proteins by phosphorylating SGK1 (O'Reilly et al., 2003). The SGK1 gene is also recognized as an important kinase, as it acts to activate ENaC (Pearce, 2003). SGK1 works to regulate NKCC2, NCC, and NHE3, all of which are directly related to sodium regulation (Valinsky et al., 2018). The high expression of SNN1G over the other subunits of ENaC and the upregulation of WNK3 and WNK4 kinases could point to specific adaptations in these complexes and their regulatory pathways, but more in-depth research into their expression levels compared to other non-desert species is needed.

GO Term Enrichment Within Clusters:

In order to deepen our understanding of the defined clusters observed in our analysis, GO term enrichment of the top ten differentially expressed genes per cluster were performed (Appendix XXIII). To look at genes that were differentially expressed between the clusters, Seurat was utilized to create a heatmap of average log2 fold change of the top ten differentially

expressed gene per cluster compared to the other clusters (Figure 2-13). This gave a visual guide to show whether genes expressed in one cluster were downregulated, not expressed, or similarly expressed in other clusters. Generally, genes expressed in clusters 2, 3, and 5 shared similar expression values, which is expected, as they share a general functional area within the kidney (cortex). Likewise, clusters 0 and 6 showed similar gene expression, as they occupy the same functional location as well (medulla). Cluster 4 and cluster 1 both show somewhat unique differential gene expression, but do show overlap with their surrounding clusters.

Genes in cluster 0 significantly clustered around two terms: phosphatase inhibitor activity (GO:0019212), and intracellular sodium ion homeostasis (GO:0006883). Renal sodium channels are not normally voltage-gated in their unphosphorylated state, but upon phosphorylation, they become voltage-dependent and increase their open probability (Ismailov et al., 1995). Therefore, inhibiting phosphatase activity would increase sodium ion channeling and subsequently sodium ion homeostasis. The loop of Henle is intimately associated with water and NaCl recovery from urine (Kondo et al., 1992), both highly important functions in desert-adapted mammals. Cluster 6 showed clustering around terms that centered around transmembrane transporter activity (GO:0015318, GO:0015075, GO:0098660, GO:0034220), membranes (GO:0016020, GO:0044289), and collecting duct acid secretion (KEGG:04966).

Terms significantly associated with cluster 1 included fumarylacetoacetase activity (GO:0004334) and ketohexokinase activity (GO:0004454. Fumarylacetoacetase is the last enzyme in the tyrosine catabolic pathway (Moe et al., 2009), and it has been found that the kidney plays a major role in the uptake of phenylalanine and its hydroxylation and release as tyrosine (Kopple, 2007). Decreased phenylalanine hydroxylation has been linked to chronic renal failure (Kopple, 2007), and specific mutations in fumarylacetoacetase results in Fanconi

syndrome (Moe et al., 2007). Ketohexokinase is a primary enzyme in fructose metabolism (Abad et al., 2011), and knockout studies of the ketohexokinase isoform A have shown that insufficiency of this enzyme can cause severe renal injury (Doke et al., 2018).

Cluster 2 and cluster 5 genes were significantly associated with a host of GO terms linked to metabolism, specifically metabolism of carboxylic acids, lipids, and glucocorticoids, along with the apical plasma membrane (Appendix XXIII). The proximal tubules mediate most of the filtering of water and solutes, and rely on fatty acid metabolism to generate a high amount of ATP to compensate (Gewin, 2021). However, glucose metabolism via gluconeogenesis is also utilized in the kidneys, though it is used for energy to a lesser extent than fatty acid metabolism, as the kidney is an important organ for glucose reabsorption, production, and utilization (Alsahli et al., 2017). Both the glucose transporters and fatty acid receptors are found on the apical membrane of the proximal tubules (Gewin, 2021). The results from cluster 3 mirror those of cluster 2, cluster 5, and cluster 1, and help to deepen the understanding of the many roles that the proximal tubules play. Cluster 3 came back with three significant terms: response to mercury ions (GO:0046689), phosphate ion transmembrane transport (GO:0035435), and gluconeogenesis (REAC:R-MMU-70263). Uptake, regulation, and excretion of ions and toxins are carried out mainly in the proximal tubules, which are intimately associated with the glomerulus, the filtering units of the kidney (Blaine et al., 2015).

Cluster 4, associated with the renal pelvis and the distal convoluted tubules, showed significant association with GO terms involved with metal ion binding and detoxification related to metal ions. While it has been hypothesized that the proximal tubules are the main area of the kidney involved with metal ion reuptake and reabsorption, the loop of Henle and the distal convoluted tubules have been associated with permeability of metals (Barbier et al., 2005).

Specifically, the divalent metal transporter 1 (DMT1) has been connected to reabsorption of metals such as $Fe^{2+}, Co^{2+}, Cd^{2+}, \text{and } Zn^{2+}$ (Barbier et al., 2004). These metals are then excreted via urine, which passes through the renal pelvis (Pizzorno, 2015).

Cluster Specific GO analysis

Crafting custom GMT files for each cluster to perform pairwise comparisons between them allowed the analysis of function of each of the individual clusters with the added information of spatially relevant upregulated functions. Starting with cluster 0, which had been connected to the general location and function of the loop of Henle, most GO terms were generated when comparing the gene list against the cluster 6 GMT file, along with more limited results from cluster 1, 2 and 4. Due to cluster 0's location, this result was intriguing, as both clusters 6 and 0 had been connected with the loop of Henle and should have had similar functions. This should have resulted in no enriched GO terms between the two. No significant terms were found when comparing the gene list for 6 against the cluster 0 GMT file. Instead, all GO terms generated for cluster 6 came from comparisons against cluster 3, which had been connected to the location and function of the proximal tubules. This suggests that cluster 6 is a subset of cluster 0, where cluster 0 may include more generalized functions of the loop of Henle, and cluster 6 includes more specialized functions. Indeed, when looking at the significantly ($P < .05$) enriched GO terms for the two clusters, cluster 0 presents with energy production, metabolism, cellular respiration, and respiratory electron transport associated terms (Appendix XXIV), while cluster 6 presents with proton transmembrane transport, ATPase complex, vacuolar related functions, iron uptake, stress response, and kinase activity (Appendix XXX).

Similar results were observed when comparing clusters 2 and 3. Cluster 3, which, as mentioned before, was connected to proximal tubule function, and had many GO terms populate

from clusters 2, 4, and 6. While cluster 4 and 6 are both different in function and location and were expected to generate results for cluster 3, cluster 2 had also been connected to the proximal tubules, and is locationally similar to cluster 3. In contrast, cluster 2 returned the sparsest results for all the clusters, and only had results when compared against cluster 1 and 3. Similar to clusters 0 and 6, this suggests that cluster 2 may be a subset of cluster 3, and performs more generalized functions. Cluster 2 returned GO terms that were broadly associated with metabolism, mitochondrion, and cellular processes (Appendix XXVI), while cluster 3 produced terms associated with transmembrane transporters, apical membrane, aldehyde and aldosterone response, sodium ion homeostasis, proton transporter activity, and kinase activity (Appendix XXVII).

Clusters 1 and 5 both showed results that seemed to place them into a mixed or generalized functional area of the kidney. Cluster 1 showed sparse results, with no real renal-specific functional GO terms other than that of distal convoluted tubules (Appendix XXV), and terms only populated when compared against clusters 0 and 2. This suggests that cluster 1 shares functions with all clusters presented and may perform functions of both the proximal tubules and the loop of Henle. It is also possible that this area of the kidney is a crossing-over point for these two functional areas, and that the specific functions are convoluted. Cluster 5 also shows this general function characteristic. Cluster 5 had been assumed to be part of the the proximal tubule cluster group, and still shows major differences from that of cluster 4, much like cluster 3. However, no results came back from comparisons against cluster 0 and 6, which was expected. Instead, GO terms populated from comparisons to 1, 2, and 3, with a higher return from cluster 2. This suggests that while 5 still shares some GO term functions with that of the proximal tubule-related cluster 3, such as “apical membrane” and “aldosterone response” (Appendix XXIX;

Appendix XXVII), it also may perform more general functions like cluster 2, who both return the GO term “metabolism” (Appendix XXVI).

Finally, cluster 4 generated the longest list of GO terms out of all the clusters. Results came back from every comparison except that of clusters 0 and 1. This was expected, as cluster 4 has been associated with the renal pelvis and is functionally and locationally unique. Terms enriched from proximal tubule-associated clusters (2, 3, and 5) include those of ribosomal functions, neuronal and nervous system-related functions, ion channel regulation, and TP53 activity (Appendix XXVIII). Comparison against the loop of Henle-associated cluster 6, returned terms such as organic compound metabolic processes, proton transporters, toxic substances, plasma membranes, and ATPase complexes (Appendix XXX). These results suggest that cluster 4 is a complex and functionally diverse area of the kidney and shows a strong association with the nervous system, specifically with dendrites. Cluster 4 has been associated with the renal pelvis, which is where a major portion of the renal afferent nerves originate (Sata et al., 2018). The renal afferent nerves are a key player in increasing renal sympathetic nerve activity (RSNA) during dehydration, which stimulates the excretion of renin (Chapman et al., 2021). Increased plasma renin leads to the production of angiotensin II, which binds to the angiotensin type 1 receptor (AT_1R) and stimulates sodium and water reabsorption pathways in the proximal tubules (Li et al., 2011). Angiotensin II also works to activate thirst response in the brain, and to stimulate the release of aldosterone, which increases salt reabsorption and potassium excretion (Chapman et al., 2021; Scott et al., 2023).

CHAPTER THREE: DISCUSSION AND FUTURE DIRECTIONS

CONCLUSIONS

Climate change has increased the percentage of arid desert environments over the years, along with ecological challenges that these deserts present. Out of these challenges, the mixture of extreme temperatures and a lack of water availability poses a substantial risk for dehydration to the animals that live there. Of the bodily systems that are affected by dehydration, the kidneys are one of the organs most at risk for immediate and long-term damage. Acute kidney injury and chronic kidney disease have both been directly linked to dehydration states, and there has been an increase in both pathologies as heat waves become more prevalent across the globe. Thus, research geared towards understanding how to survive acute dehydration will hopefully provide answers on how to help human populations living in arid environments.

Peromyscus eremicus, the desert cactus mouse, is a desert-adapted rodent that is near-model organism used to study desert adaptation in respect to physiology, behavior, and genetics. Most importantly to this study, *P. eremicus* may go its entire life without oral water uptake and has severely decreased urine output. However, these rodents experience little to no renal disfigurement from this acute dehydration state. Due to its near constant exposure to dehydration, this made it the perfect candidate for our study.

A spatial gene atlas of the histological architecture of the kidney was compiled using the 10x Genomics Visium platform, with the additional use of the R tools Seurat and BayesSpace. A total of seven distinct clusters were identified in the tissue highlighted in this study, each with a unique spatially differential gene expression signature. Clusters 2, 3, and 5 all showed

upregulated expression of marker genes for the proximal tubules, while clusters 0 and 6 showed expression for genes associated with the loop of Henle. Clusters 4 and 1 showed gene signatures of the clusters that surrounded them (clusters 2, 3, and 5 for 1, and clusters 0 and 6 for 4), but also showed their own unique expression patterns. While cluster 1 shows a combination of both the loop of Henle and proximal tubule genes and does not necessarily associate with a specific functional unit, cluster 4 has been associated with the structural unit of the renal pelvis.

Known cell type markers of kidney functional units, including the loop of Henle, proximal tubules, and distal connecting tubules, were integrated with the enhanced subpspot resolution provided by BayesSpace to create cell type identification maps across the tissue (Figures 2-8, 2-9, 2-10). The cell maps showed a wide distribution of epithelial cells, and distinct regions for the proximal tubule and loop of Henle that can be correlated to their respective clusters identified previously. Both the proximal tubules and loop of Henle cells were broken down into more specific segments, which showed wide distribution of the S3 segment of the proximal tubules and the thick and thin ascending loop of the loop of Henle, suggesting that there have been some possible physiological adaptations from that of a non-desert-adapted animal. Comparison studies would need to be conducted to confirm this finding. There was minimal expression of podocytes, fibroblasts, and mesangial cells, which has been attributed to lack of development of sufficient marker genes for this organism.

Genes intimately associated with water and sodium ion homeostasis were identified, and expression levels were explored across the clusters (figures 2-11, 2-12). A marked decrease of expression from what was expected was reported for the aquaporin gene families, which may be due to the limited water available to shunt within the kidneys. It was also hypothesized that this may be a tactic to decrease apoptotic signals within kidney tissue to minimize cellular damage

when under extreme dehydration states. Upregulation of the ENaC beta subunit was reported, along with high expression of the WNK3 and WNK 4 kinases. This upregulation of sodium-related genes suggests that *P. eremicus* has higher ion-related function in order to increase reabsorption and maintain homeostasis, which is critical to decrease injury when experiencing dehydration.

Finally, spatially differential gene expression was explored between the clusters, and GO terms associated with these genes were identified and explored in relation to the functional processes related to the kidney (Appendix XXIII). Many of the terms that were returned highlighted general function of the related functional region of the kidney (e.g., clusters 2, 3, and 5 all had terms that could be linked back to processes occurring in the proximal tubules). Further GO term analysis was performed using pairwise comparisons of the clusters by creating custom GMT files for each cluster and performing pairwise comparisons with the top highly variable genes of each cluster. This analysis showed that while some clusters are connected to a specific functional group, the remaining clusters may be functional subsets of other clusters. For example, cluster 3 was shown to produce the most robust functional GO terms related to the proximal tubules, while cluster 2 was shown to be related to more general functions and is most likely a functional subset of cluster 3. Similar results were found for clusters 0 and 6, where 6 is the subset of 0, and both are related to the loop of Henle. Clusters 1 and 5 were found to have overlapping functions for both the proximal tubules and the loop of Henle, and cluster 4 was found to be the most distinct cluster functionally, further confirming its connection to the renal pelvis, highlighted by the connection to nerve functions.

Overall, the results of this study have laid the framework for developing a deeper understanding of the kidney function of *Peromyscus eremicus*, a desert-adapted rodent that is

intimately acquainted with dehydration. Spatial clusters with unique gene signatures were identified across the tissue, along with cell type marker maps for major cell types identified within the kidney. Possible areas of adaptation correlated with the spatial information were identified, along with the gene families associated. This work will provide a launch point for future spatial projects within this organism, along with future research directions for single cell work to help further the understanding of dehydration-related desert adaptation.

What is Still Unknown?

There are many aspects of the function of *P. eremicus* kidney function that are not fully characterized. The Aquaporin family gene expression results (Figure 2-11) show that generally, aquaporin genes are not widely expressed across the tissue, even though past studies have implicated that their expression is generally increased in desert-adapted rodents (Pannabecker, 2015; Gallardo et al., 2002; Gallardo et al., 2005, Zhang et al., 2019). However, it has been shown in past studies that AQP4 has been shown to be down regulated in *P. eremicus* when in a state of dehydration (MacManes et al., 2017). It is possible that *P. eremicus* has developed specific adaptations that lead to down regulation of these water handling proteins. More studies on this gene family is required to parse out the reasoning for this discrepancy in findings.

Similarly, when exploring the sodium related genes within our dataset, high levels of expression were noted for the SCNN1G gene, which encodes for the beta subunit for the ENaC complex (An et al., 2022) but not for any of the other subunits of the same complex. No studies have looked into the overexpression of this specific subunit, and very little can be found on its specific function outside of being the building block for this sodium-handling complex. Expression comparison to a non-desert adapted model and more research into the functionality of this subunit may be required to understand these results.

Another question related to the sodium ion related genes comes from analyzing the WNK kinases. While high expression was noted for WNK3 and WNK4, WNK1 was considerably lower than both (Figure 2-12). WNK1 has coupling effects with WNK3, and they work together to help inhibit WNK4 to regulate kidney ion channels (An et al., 2022). It would be assumed that if one coupled kinase is upregulated, along with the kinase it helps inhibit, then the other coupled kinase would also be upregulated. More research elucidating this connection and upregulation is needed to fully understand the interactions and processes involved within this desert-adapted kidney system.

When exploring cell type distribution across the tissue, some cell types were not well detected, such as fibroblasts, mesangial cells, podocytes, and the connecting tubules. As described earlier, mesangial cells and podocytes are part of the glomerular structures of the kidney and are essential to normal kidney health. This leads to the question of whether our specific kidney tissue slices alone did not contain many of these structures, or if there are specific cell markers for *P. eremicus* that have not been reported thus far. Integrating single cell data into our spatial dataset would possibly help deconvolute these results and provide a clearer cell type distribution of the kidney.

Finally, the pairwise GO term comparison revealed that some clusters identified within the tissue have mixed functions of both the loop of Henle and proximal tubules. This finding suggests that the functions and tubular structures are interwoven and may share anatomical space. It was also found that some clusters, while sharing a functional unit (i.e. proximal tubules), do not share similar functions, and that more specific defining cellular and anatomical functions may have locational specificity. There is need for further deconvolution of specific kidney functions to help elucidate specific spatial function within the kidney; single cell data

paired with a spatial dataset may bring crucial details to the forefront and help elucidate these results.

Future Studies

The results of the study have provided ample future research opportunities to explore the differential gene expression of both the aquaporin gene family and of genes related to sodium ion channel complexes and their regulatory kinases. The study also has set the groundwork to create a spatial atlas of dehydrated *P. eremicus* kidney tissue to compare the results to this study and explore differential or upregulated functions under a dehydrated state. As tools continue to develop to explore spatial datasets, more analyses will be performed in order to elucidate gene expression and cell types we may be unable to detect at the time.

REFERENCES

Abad, M. C., Gibbs, A. C., & Zhang, X. (2011). Chapter nineteen—Electron Density Guided Fragment-Based Drug Design—A Lead Generation Example. In L. C. Kuo (Ed.), *Methods in Enzymology* (Vol. 493, pp. 487–508). Academic Press. https://doi.org/10.1016/B978-0-12-381274-2.00019-4

Aboul Naga, A. M., Abdel Khalek, T. M., Osman, M., Elbeltagy, A. R., Abdel-Aal, E. S., Abou-Ammo, F. F., & El-Shafie, M. H. (2021). Physiological and genetic adaptation of desert sheep and goats to heat stress in the arid areas of Egypt. *Small Ruminant Research*, *203*, 106499. https://doi.org/10.1016/j.smallrumres.2021.106499

Ali, M. A., Abu Damir, H., Ali, O. M., Amir, N., Tariq, S., Greenwood, M. P., Lin, P., Gillard, B., Murphy, D., & Adem, A. (2020). The effect of long-term dehydration and subsequent rehydration on markers of inflammation, oxidative stress and apoptosis in the camel kidney. *BMC Veterinary Research*, *16*(1), 458. https://doi.org/10.1186/s12917-020-02628-5

Alsahli, M., & Gerich, J. E. (2017). Renal glucose metabolism in normal physiological conditions and in diabetes. *Diabetes Research and Clinical Practice*, *133*, 1–9. https://doi.org/10.1016/j.diabres.2017.07.033

Altschuler, E. L., Nagle, R. B., Braun, E. J., Lindstedt, S. L., & Krutzsch, P. H. (1979). Morphological study of the desert heteromyid kidney with emphasis on the genus perognathus. *The Anatomical Record*, *194*(3). https://doi.org/10.1002/ar.1091940311

Alvira-Iraizoz, F., Gillard, B. T., Lin, P., Paterson, A., Pauža, A. G., Ali, M. A., Alabsi, A. H., Burger, P. A., Hamadi, N., Adem, A., Murphy, D., & Greenwood, M. P. (2021). Multiomic analysis of the Arabian camel (Camelus dromedarius) kidney reveals a role for cholesterol in water conservation. *Communications Biology*, *4*(1), Article 1. https://doi.org/10.1038/s42003-021-02327-3

Ardaillou, R. (1999). Angiotensin II receptors. *Journal of the American Society of Nephrology*, *10 Suppl 11*, S30-9.

Asp, M., Bergenstråhle, J., & Lundeberg, J. (2020). Spatially Resolved Transcriptomes—Next Generation Tools for Tissue Exploration. *BioEssays*, *42*(10), 1900221. https://doi.org/10.1002/bies.201900221

Balzer, M. S., Rohacs, T., & Susztak, K. (2022). How Many Cell Types Are in the Kidney and What Do They Do? *Annual Review of Physiology*, *84*, 507–531. https://doi.org/10.1146/annurev-physiol-052521-121841

Bankir, L., Bichet, D. G., & Morgenthaler, N. G. (2017). Vasopressin: Physiology, assessment and osmosensation. *Journal of Internal Medicine*, *282*(4), 284–297. https://doi.org/10.1111/joim.12645

Barbier, O., Jacquillet, G., Tauc, M., Cougnon, M., & Poujeol, P. (2005). Effect of Heavy Metals on, and Handling by, the Kidney. *Nephron Physiology*, *99*(4), p105–p110. https://doi.org/10.1159/000083981

Barbier, O., Jacquillet, G., Tauc, M., Poujeol, P., & Cougnon, M. (2004). Acute study of interaction among cadmium, calcium, and zinc transport along the rat nephron in vivo. *American Journal of Physiology. Renal Physiology*, *287*(5), F1067-1075. https://doi.org/10.1152/ajprenal.00120.2004

Bedford, N. L., & Hoekstra, H. E. (2015). Peromyscus mice as a model for studying natural variation. *ELife*, *4*, e06813. https://doi.org/10.7554/eLife.06813

Blaine, J., Chonchol, M., & Levi, M. (2015). Renal Control of Calcium, Phosphate, and Magnesium Homeostasis. *Clinical Journal of the American Society of Nephrology : CJASN*, *10*(7), 1257–1272. https://doi.org/10.2215/CJN.09750913

Blumstein, D. M., Colella, J. P., Linder, E., & MacManes, M. D. (2022). *High total water loss driven by low-fat diet in desert-adapted mice* (p. 2022.04.15.488461). bioRxiv. https://doi.org/10.1101/2022.04.15.488461

Bouby, N., Ahloulay, M., Nsegbe, E., Déchaux, M., Schmitt, F., & Bankir, L. (1996). Vasopressin increases glomerular filtration rate in conscious rats through its antidiuretic action. *Journal of the American Society of Nephrology*, *7*(6), 842. https://doi.org/10.1681/ASN.V76842

Brown, D., Katsura, T., Kawashima, M., Verkman, A. S., & Sabolic, I. (1995). Cellular distribution of the aquaporins: A family of water channel proteins. *Histochemistry and Cell Biology*, *104*(1), 1–9. https://doi.org/10.1007/BF01464780

Burg, M. B., Ferraris, J. D., & Dmitrieva, N. I. (2007). Cellular response to hyperosmotic stresses. *Physiological Reviews*, *87*(4), 1441–1474. https://doi.org/10.1152/physrev.00056.2006

Butler, A., Hoffman, P., Smibert, P., Papalexi, E., & Satija, R. (2018). Integrating single-cell transcriptomic data across different conditions, technologies, and species. *Nature Biotechnology*, *36*(5), Article 5. https://doi.org/10.1038/nbt.4096

Chapman, C. L., Johnson, B. D., Parker, M. D., Hostler, D., Pryor, R. R., & Schlader, Z. (n.d.). Kidney physiology and pathophysiology during heat stress and the modification by exercise, dehydration, heat acclimation and aging. *Temperature: Multidisciplinary Biomedical Journal*, *8*(2), 108–159. https://doi.org/10.1080/23328940.2020.1826841

Chen, T. K., Knicely, D. H., & Grams, M. E. (2019). Chronic Kidney Disease Diagnosis and Management: A Review. *JAMA*, *322*(13), 1294–1304. https://doi.org/10.1001/jama.2019.14745

Cheuvront, S. N., Kenefick, R. W., Charkoudian, N., & Sawka, M. N. (2013). Physiologic basis for understanding quantitative dehydration assessment. *The American Journal of Clinical Nutrition*, *97*(3), 455–462. https://doi.org/10.3945/ajcn.112.044172

Clark, J. Z., Chen, L., Chou, C.-L., Jung, H. J., Lee, J. W., & Knepper, M. A. (2019). Representation and relative abundance of cell-type selective markers in whole-kidney RNA-Seq data. *Kidney International*, *95*(4), 787–796. https://doi.org/10.1016/j.kint.2018.11.028

Colella, J. P., Blumstein, D. M., & MacManes, M. D. (2021a). Disentangling environmental drivers of circadian metabolism in desert-adapted mice. *Journal of Experimental Biology*, *224*(18), jeb242529. https://doi.org/10.1242/jeb.242529

Colella, J. P., Tigano, A., & MacManes, M. D. (2020). A linked-read approach to museomics: Higher quality de novo genome assemblies from degraded tissues. *Molecular Ecology Resources*, *20*(4), 856–870. https://doi.org/10.1111/1755-0998.13155

Cortés, A., Rosenmann, M., & Bozinovic, F. (2000). Water economy in rodents: Evaporative water loss and metabolic water production. *Revista Chilena de Historia Natural*, *73*(2), 311–321. https://doi.org/10.4067/S0716-078X2000000200006

Cuzzo, B., Padala, S. A., & Lappin, S. L. (2023). Physiology, Vasopressin. In *StatPearls*. StatPearls Publishing. http://www.ncbi.nlm.nih.gov/books/NBK526069/

Dawson, T. J., Blaney, C. E., McCarron, H. C. K., & Maloney, S. K. (2007). Dehydration, with and without heat, in kangaroos from mesic and arid habitats: Different thermal responses including varying patterns in heterothermy in the field and laboratory. *Journal of Comparative Physiology B*, *177*(7), 797–807. https://doi.org/10.1007/s00360-007-0176-1

Dewey, M. J., & Dawson, W. D. (2001). Deer mice: "The Drosophila of North American mammalogy." *Genesis (New York, N.Y.: 2000)*, *29*(3), 105–109. https://doi.org/10.1002/gene.1011

Dixon, E. E., Wu, H., Muto, Y., Wilson, P. C., & Humphreys, B. D. (2022). Spatially Resolved Transcriptomic Analysis of Acute Kidney Injury in a Female Murine Model. *Journal of the American Society of Nephrology*, *33*(2), 279. https://doi.org/10.1681/ASN.2021081150

Doke, T., Ishimoto, T., Hayasaki, T., Ikeda, S., Hasebe, M., Hirayama, A., Soga, T., Kato, N., Kosugi, T., Tsuboi, N., Lanaspa, M. A., Johnson, R. J., Kadomatsu, K., & Maruyama, S. (2018). Lacking Ketohexokinase-A Exacerbates Renal Injury in Streptozotocin-induced Diabetic Mice. *Metabolism: Clinical and Experimental*, *85*, 161–170. https://doi.org/10.1016/j.metabol.2018.03.020

Drickamer, L. C., & Vestal, B. M. (1973). Patterns of Reproduction in a Laboratory Colony of Peromyscus. *Journal of Mammalogy*, *54*(2), 523–528. https://doi.org/10.2307/1379147

Dumas, S. J., Meta, E., Borri, M., Goveia, J., Rohlenova, K., Conchinha, N. V., Falkenberg, K., Teuwen, L.-A., de Rooij, L., Kalucka, J., Chen, R., Khan, S., Taverna, F., Lu, W., Parys, M., De Legher, C., Vinckier, S., Karakach, T. K., Schoonjans, L., … Carmeliet, P. (2020). Single-Cell RNA Sequencing Reveals Renal Endothelium Heterogeneity and Metabolic Adaptation to Water Deprivation. *Journal of the American Society of Nephrology : JASN*, *31*(1), 118–138. https://doi.org/10.1681/ASN.2019080832

Ebefors, K., Bergwall, L., & Nyström, J. (2022). The Glomerulus According to the Mesangium. *Frontiers in Medicine*, *8*, 740527. https://doi.org/10.3389/fmed.2021.740527

Edelheit, O., Hanukoglu, I., Gizewska, M., Kandemir, N., Tenenbaum-Rakover, Y., Yurdakök, M., Zajaczek, S., & Hanukoglu, A. (2005). Novel mutations in epithelial sodium channel (ENaC) subunit genes and phenotypic expression of multisystem pseudohypoaldosteronism. *Clinical Endocrinology*, *62*(5), 547–553. https://doi.org/10.1111/j.1365-2265.2005.02255.x

Edsgärd, D., Johnsson, P., & Sandberg, R. (2018). Identification of spatial expression trends in single-cell gene expression data. *Nature Methods*, *15*(5), Article 5. https://doi.org/10.1038/nmeth.4634

Esteva-Font, C., Ballarin, J., & Fernández-Llama, P. (2012). Molecular biology of water and salt regulation in the kidney. *Cellular and Molecular Life Sciences*, *69*(5), 683–695. https://doi.org/10.1007/s00018-011-0858-4

Fountain, J. H., Kaur, J., & Lappin, S. L. (2023). Physiology, Renin Angiotensin System. In *StatPearls*. StatPearls Publishing. http://www.ncbi.nlm.nih.gov/books/NBK470410/

Gallardo, P. A., Cortés, A., & Bozinovic, F. (2005). Phenotypic Flexibility at the Molecular and Organismal Level Allows Desert-Dwelling Rodents to Cope with Seasonal Water Availability. *Physiological and Biochemical Zoology*, *78*(2), 145–152. https://doi.org/10.1086/425203

Gallardo, P., Olea, N., & Sepúlveda, F. V. (2002). Distribution of aquaporins in the colon of Octodon degus, a South American desert rodent. *American Journal of Physiology-Regulatory, Integrative and Comparative Physiology*, *283*(3), R779–R788. https://doi.org/10.1152/ajpregu.00218.2002

Gewin, L. S. (2021). Sugar or Fat? Renal Tubular Metabolism Reviewed in Health and Disease. *Nutrients*, *13*(5), 1580. https://doi.org/10.3390/nu13051580

Ghobrial, L. I., & Nour, T. A. (1975). The Physiological Adaptations of Desert Rodents. In I. Prakash & P. K. Ghosh (Eds.), *Rodents in Desert Environments* (pp. 413–444). Springer Netherlands. https://doi.org/10.1007/978-94-010-1944-6_21

Giorello, F. M., Feijoo, M., D'Elía, G., Naya, D. E., Valdez, L., Opazo, J. C., & Lessa, E. P. (2018). An association between differential expression and genetic divergence in the Patagonian olive mouse (Abrothrix olivacea). *Molecular Ecology*, *27*(16), 3274–3286. https://doi.org/10.1111/mec.14778

Gull, M., & Pasek, M. A. (2021). The Role of Glycerol and Its Derivatives in the Biochemistry of Living Organisms, and Their Prebiotic Origin and Significance in the Evolution of Life. *Catalysts*, *11*(1), Article 1. https://doi.org/10.3390/catal11010086

Hanukoglu, I., & Hanukoglu, A. (2016). Epithelial sodium channel (ENaC) family: Phylogeny, structure-function, tissue distribution, and associated inherited diseases. *Gene*, *579*(2), 95–132. https://doi.org/10.1016/j.gene.2015.12.061

Hao, Y., Hao, S., Andersen-Nissen, E., Mauck, W. M., Zheng, S., Butler, A., Lee, M. J., Wilk, A. J., Darby, C., Zager, M., Hoffman, P., Stoeckius, M., Papalexi, E., Mimitou, E. P., Jain, J., Srivastava, A., Stuart, T., Fleming, L. M., Yeung, B., … Satija, R. (2021). Integrated analysis of multimodal single-cell data. *Cell*, *184*(13), 3573-3587.e29. https://doi.org/10.1016/j.cell.2021.04.048

Hayward, J. S. (1965). Metabolic rate and its temperature-adaptive significance in six geographic races of peromyscus. *Canadian Journal of Zoology*, *43*(2), 309–323. https://doi.org/10.1139/z65-029

Hebert, S. C. (1998). Roles of Na-K-2Cl and Na-Cl cotransporters and ROMK potassium channels in urinary concentrating mechanism. *The American Journal of Physiology*, *275*(3), F325-327. https://doi.org/10.1152/ajprenal.1998.275.3.F325

Ismailov, I. I., & Benos, D. J. (1995). Effects of phosphorylation on ion channel function. *Kidney International*, *48*(4), 1167–1179. https://doi.org/10.1038/ki.1995.400

Jablonski, E. M., Mattocks, M. A., Sokolov, E., Koniaris, L. G., Hughes, F. M., Fausto, N., Pierce, R. H., & McKillop, I. H. (2007). Decreased Aquaporin Expression Leads to Increased Resistance to Apoptosis in Hepatocellular Carcinoma. *Cancer Letters*, *250*(1), 36–46. https://doi.org/10.1016/j.canlet.2006.09.013

Johnson, R. J., Stenvinkel, P., Jensen, T., Lanaspa, M. A., Roncal, C., Song, Z., Bankir, L., & Sánchez-Lozada, L. G. (2016). Metabolic and Kidney Diseases in the Setting of Climate Change, Water Shortage, and Survival Factors. *Journal of the American Society of Nephrology: JASN*, *27*(8), 2247–2256. https://doi.org/10.1681/ASN.2015121314

Kaißling, B., de Rouffignac, C., Barrett, J. M., & Kriz, W. (1975). The structural organization of the kidney of the desert rodent Psammomys obesus. *Anatomy and Embryology*, *148*(2), 121–143. https://doi.org/10.1007/BF00315265

Kaplan, M. R., Plotkin, M. D., Lee, W. S., Xu, Z. C., Lytton, J., & Hebert, S. C. (1996). Apical localization of the Na-K-Cl cotransporter, rBSC1, on rat thick ascending limbs. *Kidney International*, *49*(1), 40–47. https://doi.org/10.1038/ki.1996.6

Kavouras, S. A. (2002). Assessing hydration status. *Current Opinion in Clinical Nutrition & Metabolic Care*, *5*(5), 519.

Kjær, A., Knigge, U., Jørgensen, H., & Warberg, J. (2000). Dehydration-induced vasopressin secretion in humans: Involvement of the histaminergic system. *American Journal of Physiology-Endocrinology and Metabolism*, *279*(6), E1305–E1310. https://doi.org/10.1152/ajpendo.2000.279.6.E1305

Kondo, Y., Kudo, K., Igarashi, Y., Kuba, Y., Arima, S., Tada, K., & Abe, K. (1992). Functions of Ascending Thin Limb of Henle's Loop with Special Emphasis on Mechanism of NaCl Transport. *The Tohoku Journal of Experimental Medicine*, *166*(1), 75–84. https://doi.org/10.1620/tjem.166.75

Kopple, J. D. (2007). Phenylalanine and Tyrosine Metabolism in Chronic Kidney Failure. *The Journal of Nutrition*, *137*(6), 1586S-1590S. https://doi.org/10.1093/jn/137.6.1586S

Kordonowy, L. L., & MacManes, M. D. (2016). Characterization of a male reproductive transcriptome for Peromyscus eremicus (Cactus mouse). *PeerJ*, *4*, e2617. https://doi.org/10.7717/peerj.2617

Kordonowy, L., Lombardo, K. D., Green, H. L., Dawson, M. D., Bolton, E. A., LaCourse, S., & MacManes, M. D. (2017). Physiological and biochemical changes associated with acute experimental dehydration in the desert adapted mouse, Peromyscus eremicus. *Physiological Reports*, *5*(6), e13218. https://doi.org/10.14814/phy2.13218

Kordonowy, L., & MacManes, M. (2017). Characterizing the reproductive transcriptomic correlates of acute dehydration in males in the desert-adapted rodent, Peromyscus eremicus. *BMC Genomics*, *18*(1), 473. https://doi.org/10.1186/s12864-017-3840-1

Kovesdy, C. P. (2022). Epidemiology of chronic kidney disease: An update 2022. *Kidney International Supplements*, *12*(1), 7–11. https://doi.org/10.1016/j.kisu.2021.11.003

Lee, J. W., Chou, C.-L., & Knepper, M. A. (2015). Deep Sequencing in Microdissected Renal Tubules Identifies Nephron Segment-Specific Transcriptomes. *Journal of the American Society of Nephrology: JASN*, *26*(11), 2669–2677. https://doi.org/10.1681/ASN.2014111067

Li, H., Weatherford, E. T., Davis, D. R., Keen, H. L., Grobe, J. L., Daugherty, A., Cassis, L. A., Allen, A. M., & Sigmund, C. D. (2011). Renal proximal tubule angiotensin AT1A receptors regulate blood pressure. *American Journal of Physiology - Regulatory, Integrative and Comparative Physiology*, *301*(4), R1067–R1077. https://doi.org/10.1152/ajpregu.00124.2011

Liu, H., Hooper, S. B., Armugam, A., Dawson, N., Ferraro, T., Jeyaseelan, K., Thiel, A., Koukoulas, I., & Wintour, E. M. (2003). Aquaporin gene expression and regulation in the ovine fetal lung. *The Journal of Physiology*, *551*(2), 503–514. https://doi.org/10.1113/jphysiol.2003.044875

MacManes, M. D. (2017). Severe acute dehydration in a desert rodent elicits a transcriptional response that effectively prevents kidney injury. *American Journal of Physiology-Renal Physiology*, *313*(2), F262–F272. https://doi.org/10.1152/ajprenal.00067.2017

MacManes, M. D., & Eisen, M. B. (2014). Characterization of the transcriptome, nucleotide sequence polymorphism, and natural selection in the desert adapted mouse Peromyscus eremicus. *PeerJ*, *2*, e642. https://doi.org/10.7717/peerj.642

Marcoux, A.-A., Tremblay, L. E., Slimani, S., Fiola, M.-J., Mac-Way, F., Garneau, A. P., & Isenring, P. (2021). Molecular characteristics and physiological roles of Na+ -K+ -Cl- cotransporter 2. *Journal of Cellular Physiology*, *236*(3), 1712–1729. https://doi.org/10.1002/jcp.29997

Marra, N. J., Eo, S. H., Hale, M. C., Waser, P. M., & DeWoody, J. A. (2012). A priori and a posteriori approaches for finding genes of evolutionary interest in non-model species: Osmoregulatory genes in the kidney transcriptome of the desert rodent Dipodomys spectabilis (banner-tailed kangaroo rat). *Comparative Biochemistry and Physiology Part D: Genomics and Proteomics*, *7*(4), 328–339. https://doi.org/10.1016/j.cbd.2012.07.001

Marra, N. J., Romero, A., & DeWoody, J. A. (2014). Natural selection and the genetic basis of osmoregulation in heteromyid rodents as revealed by RNA-seq. *Molecular Ecology*, *23*(11), 2699–2711. https://doi.org/10.1111/mec.12764

Martin, L. B., Weil, Z. M., & Nelson, R. J. (2007). Immune defense and reproductive pace of life in Peromyscus mice. *Ecology*, *88*(10), 2516–2528. https://doi.org/10.1890/07-0060.1

McNab, B. K., & Morrison, P. (1963). Body Temperature and Metabolism in Subspecies of Peromyscus from Arid and Mesic Environments. *Ecological Monographs*, *33*(1), 63–82. https://doi.org/10.2307/1948477

Mehta, R. L., Cerdá, J., Burdmann, E. A., Tonelli, M., García-García, G., Jha, V., Susantitaphong, P., Rocco, M., Vanholder, R., Sever, M. S., Cruz, D., Jaber, B., Lameire, N. H., Lombardi, R., Lewington, A., Feehally, J., Finkelstein, F., Levin, N., Pannu, N., … Remuzzi, G. (2015). International Society of Nephrology's 0by25 initiative for acute kidney injury (zero preventable deaths by 2025): A human rights case for nephrology. *The Lancet*, *385*(9987), 2616–2643. https://doi.org/10.1016/S0140-6736(15)60126-X

Miao, Z., Balzer, M. S., Ma, Z., Liu, H., Wu, J., Shrestha, R., Aranyi, T., Kwan, A., Kondo, A., Pontoglio, M., Kim, J., Li, M., Kaestner, K. H., & Susztak, K. (2021). Single cell regulatory landscape of the mouse kidney highlights cellular differentiation programs and disease targets. *Nature Communications*, *12*(1), Article 1. https://doi.org/10.1038/s41467-021-22266-1

Moe, O. W., Seldin, D. W., & Baum, M. (2009). Chapter 10—The Fanconi Syndrome. In R. P. Lifton, S. Somlo, G. H. Giebisch, & D. W. Seldin (Eds.), *Genetic Diseases of the Kidney* (pp. 171–197). Academic Press. https://doi.org/10.1016/B978-0-12-449851-8.00010-3

Noor, S., Mohammad, T., Ashraf, G. M., Farhat, J., Bilgrami, A. L., Eapen, M. S., Sohal, S. S., Yadav, D. K., & Hassan, M. I. (2021). Mechanistic insights into the role of serum-glucocorticoid kinase 1 in diabetic nephropathy: A systematic review. *International Journal of Biological Macromolecules*, *193*(Pt A), 562–573. https://doi.org/10.1016/j.ijbiomac.2021.10.165

Nose, H., Mack, G. W., Shi, X. R., & Nadel, E. R. (1988). Shift in body fluid compartments after dehydration in humans. *Journal of Applied Physiology*, *65*(1), 318–324. https://doi.org/10.1152/jappl.1988.65.1.318

Nugent, B. W. (2005). Hyperosmolar Hyperglycemic State. *Emergency Medicine Clinics of North America*, *23*(3), 629–648. https://doi.org/10.1016/j.emc.2005.03.006

Oi, K., Sohara, E., Rai, T., Misawa, M., Chiga, M., Alessi, D. R., Sasaki, S., & Uchida, S. (2011). A minor role of WNK3 in regulating phosphorylation of renal NKCC2 and NCC co-transporters in vivo. *Biology Open*, *1*(2), 120–127. https://doi.org/10.1242/bio.2011048

O'Reilly, M., Marshall, E., Speirs, H. J. L., & Brown, R. W. (2003). WNK1, a Gene within a Novel Blood Pressure Control Pathway, Tissue-Specifically Generates Radically Different Isoforms with and without a Kinase Domain. *Journal of the American Society of Nephrology*, *14*(10), 2447. https://doi.org/10.1097/01.ASN.0000089830.97681.3B

Ortiz, C., Navarro, J. F., Jurek, A., Märtin, A., Lundeberg, J., & Meletis, K. (2020). Molecular atlas of the adult mouse brain. *Science Advances*, *6*(26), eabb3446. https://doi.org/10.1126/sciadv.abb3446

Osborne, P., Hall, L. J., Kronfeld-Schor, N., Thybert, D., & Haerty, W. (2020). A rather dry subject; investigating the study of arid-associated microbial communities. *Environmental Microbiome*, *15*, 20. https://doi.org/10.1186/s40793-020-00367-6

Pannabecker, T. L. (2015). Aquaporins in Desert Rodent Physiology. *The Biological Bulletin*, *229*(1), 120–128. https://doi.org/10.1086/BBLv229n1p120

Park, J., Shrestha, R., Qiu, C., Kondo, A., Huang, S., Werth, M., Li, M., Barasch, J., & Suszták, K. (2018). Single-cell transcriptomics of the mouse kidney reveals potential cellular targets of kidney disease. *Science (New York, N.Y.)*, *360*(6390), 758–763. https://doi.org/10.1126/science.aar2131

Pearce, D. (2003). SGK1 regulation of epithelial sodium transport. *Cellular Physiology and Biochemistry: International Journal of Experimental Cellular Physiology, Biochemistry, and Pharmacology*, *13*(1), 13–20. https://doi.org/10.1159/000070245

Pizzagalli, M. D., Bensimon, A., & Superti-Furga, G. (2021). A guide to plasma membrane solute carrier proteins. *The Febs Journal*, *288*(9), 2784–2835. https://doi.org/10.1111/febs.15531

Pizzorno, J. (2015). The Kidney Dysfunction Epidemic, Part 1: Causes. *Integrative Medicine: A Clinician's Journal*, *14*(6), 8–13.

Raghubar, A. M., Pham, D. T., Tan, X., Grice, L. F., Crawford, J., Lam, P. Y., Andersen, S. B., Yoon, S., Ng, M. S. Y., Teoh, S. M., Holland, S. E., Stewart, A., Francis, L., Combes, A. N., Kassianos, A. J., Healy, H., Nguyen, Q., & Mallett, A. J. (2020). *Spatially resolved transcriptome profiles of mammalian kidneys illustrate the molecular complexity of functional nephron segments, cell-to-*

cell interactions and genetic variants (p. 2020.09.29.317917). bioRxiv. https://doi.org/10.1101/2020.09.29.317917

Randall, J. A. (1993). Behavioural adaptations of desert rodents (Heteromyidae). *Animal Behaviour*, *45*(2), 263–287. https://doi.org/10.1006/anbe.1993.1032

Reimand, J., Kull, M., Peterson, H., Hansen, J., & Vilo, J. (2007). g:Profiler—A web-based toolset for functional profiling of gene lists from large-scale experiments. *Nucleic Acids Research*, *35*(Web Server issue), W193–W200. https://doi.org/10.1093/nar/gkm226

Rocha, J. L., Godinho, R., Brito, J. C., & Nielsen, R. (2021). Life in Deserts: The Genetic Basis of Mammalian Desert Adaptation. *Trends in Ecology & Evolution*, *36*(7), 637–650. https://doi.org/10.1016/j.tree.2021.03.007

Roncal-Jimenez, C., Lanaspa, M. A., Jensen, T., Sanchez-Lozada, L. G., & Johnson, R. J. (2015). Mechanisms by Which Dehydration May Lead to Chronic Kidney Disease. *Annals of Nutrition & Metabolism*, *66 Suppl 3*, 10–13. https://doi.org/10.1159/000381239

Sata, Y., Head, G. A., Denton, K., May, C. N., & Schlaich, M. P. (2018). Role of the Sympathetic Nervous System and Its Modulation in Renal Hypertension. *Frontiers in Medicine*, *5*. https://www.frontiersin.org/articles/10.3389/fmed.2018.00082

Satija, R., Farrell, J. A., Gennert, D., Schier, A. F., & Regev, A. (2015). Spatial reconstruction of single-cell gene expression data. *Nature Biotechnology*, *33*(5), Article 5. https://doi.org/10.1038/nbt.3192

Schmidt-Nielsen, K., Schmidt-Nielsen, B., & Schneiderman, H. (1948). SALT EXCRETION IN DESERT MAMMALS. *American Journal of Physiology-Legacy Content*, *154*(1), 163–166. https://doi.org/10.1152/ajplegacy.1948.154.1.163

Schwimmer, H., & Haim, A. (2009). Physiological adaptations of small mammals to desert ecosystems. *Integrative Zoology*, *4*(4), 357–366. https://doi.org/10.1111/j.1749-4877.2009.00176.x

Scott, J. H., Menouar, M. A., & Dunn, R. J. (2023b). Physiology, Aldosterone. In *StatPearls*. StatPearls Publishing. http://www.ncbi.nlm.nih.gov/books/NBK470339/

Sikes, R. S., & Gannon, W. L. (2011). Guidelines of the American Society of Mammalogists for the use of wild mammals in research. *Journal of Mammalogy*, *92*(1), 235–253.

Siragy, H. M. (2010). The angiotensin II type 2 receptor and the kidney. *Journal of the Renin-Angiotensin-Aldosterone System : JRAAS*, *11*(1), 33–36. https://doi.org/10.1177/1470320309347786

Sohara, E., Rai, T., Sasaki, S., & Uchida, S. (2006). Physiological roles of AQP7 in the kidney: Lessons from AQP7 knockout mice. *Biochimica Et Biophysica Acta*, *1758*(8), 1106–1110. https://doi.org/10.1016/j.bbamem.2006.04.002

Sonani, B., Naganathan, S., & Al-Dhahir, M. A. (2023). Hypernatremia. In *StatPearls*. StatPearls Publishing. http://www.ncbi.nlm.nih.gov/books/NBK441960/

Ståhl, P. L., Salmén, F., Vickovic, S., Lundmark, A., Navarro, J. F., Magnusson, J., Giacomello, S., Asp, M., Westholm, J. O., Huss, M., Mollbrink, A., Linnarsson, S., Codeluppi, S., Borg, Å., Pontén, F., Costea, P. I., Sahlén, P., Mulder, J., Bergmann, O., … Frisén, J. (2016). Visualization and analysis of gene expression in tissue sections by spatial transcriptomics. *Science*, *353*(6294), 78–82. https://doi.org/10.1126/science.aaf2403

Storz, J. F., Cheviron, Z. A., McClelland, G. B., & Scott, G. R. (2019). Evolution of physiological performance capacities and environmental adaptation: Insights from high-elevation deer mice (Peromyscus maniculatus). *Journal of Mammalogy*, *100*(3), 910–922. https://doi.org/10.1093/jmammal/gyy173

Stoyan, Dietrich & Wälder, Olga. (2000). On Variograms in Point Process Statistics, II: Models of Markings and Ecological Interpretation. Biometrical Journal. 42. 171 - 187. 10.1002/(SICI)1521-4036(200005)42:2<171::AID-BIMJ171>3.0.CO;2-L.

Stuart, T., Butler, A., Hoffman, P., Hafemeister, C., Papalexi, E., Mauck, W. M., Hao, Y., Stoeckius, M., Smibert, P., & Satija, R. (2019). Comprehensive Integration of Single-Cell Data. *Cell*, *177*(7), 1888-1902.e21. https://doi.org/10.1016/j.cell.2019.05.031

Takei, Y., Bartolo, R. C., Fujihara, H., Ueta, Y., & Donald, J. A. (2012). Water deprivation induces appetite and alters metabolic strategy in Notomys alexis: Unique mechanisms for water production in the desert. *Proceedings of the Royal Society B: Biological Sciences*, *279*(1738), 2599–2608. https://doi.org/10.1098/rspb.2011.2627

Tigano, A., Colella, J. P., & MacManes, M. D. (2020). Comparative and population genomics approaches reveal the basis of adaptation to deserts in a small rodent. *Molecular Ecology*, *29*(7), 1300–1314. https://doi.org/10.1111/mec.15401

Trainor, B. C., Martin, L. B., Greiwe, K. M., Kuhlman, J. R., & Nelson, R. J. (2006). Social and photoperiod effects on reproduction in five species of Peromyscus. *General and Comparative Endocrinology*, *148*(2), 252–259. https://doi.org/10.1016/j.ygcen.2006.03.006

Valinsky, W. C., Touyz, R. M., & Shrier, A. (2018). Aldosterone, SGK1, and ion channels in the kidney. *Clinical Science*, *132*(2), 173–183. https://doi.org/10.1042/CS20171525

van Rosendal, S. P., Osborne, M. A., Fassett, R. G., & Coombes, J. S. (2010). Guidelines for glycerol use in hyperhydration and rehydration associated with exercise. *Sports Medicine (Auckland, N.Z.)*, *40*(2), 113–129. https://doi.org/10.2165/11530760-000000000-00000

Veríssimo, F., & Jordan, P. (2001). WNK kinases, a novel protein kinase subfamily in multi-cellular organisms. *Oncogene*, *20*(39), Article 39. https://doi.org/10.1038/sj.onc.1204726

Verkman, A. S. (2002). Physiological importance of aquaporin water channels. *Annals of Medicine*, *34*(3), 192–200.

Weber, J. N., Peterson, B. K., & Hoekstra, H. E. (2013). Discrete genetic modules are responsible for complex burrow evolution in Peromyscus mice. *Nature*, *493*(7432), Article 7432. https://doi.org/10.1038/nature11816

Wu, H., Guang, X., Al-Fageeh, M. B., Cao, J., Pan, S., Zhou, H., Zhang, L., Abutarboush, M. H., Xing, Y., Xie, Z., Alshanqeeti, A. S., Zhang, Y., Yao, Q., Al-Shomrani, B. M., Zhang, D., Li, J., Manee, M. M., Yang, Z., Yang, L., … Wang, J. (2014). Camelid genomes reveal evolution and adaptation to desert environments. *Nature Communications*, *5*(1), Article 1. https://doi.org/10.1038/ncomms6188

Wu, H., & Humphreys, B. D. (2017). The promise of single-cell RNA sequencing for kidney disease investigation. *Kidney International*, *92*(6), 1334–1342. https://doi.org/10.1016/j.kint.2017.06.033

Xu, M.-M., & Wang, D.-H. (2016). Water deprivation up-regulates urine osmolality and renal aquaporin 2 in Mongolian gerbils (Meriones unguiculatus). *Comparative Biochemistry and Physiology Part A: Molecular & Integrative Physiology*, *194*, 37–44. https://doi.org/10.1016/j.cbpa.2016.01.015

Yawitz, T. A., Barts, N., & Kohl, K. D. (2022). Comparative digestive morphology and physiology of five species of Peromyscus under controlled environment and diet. *Comparative Biochemistry and Physiology Part A: Molecular & Integrative Physiology*, *271*, 111265. https://doi.org/10.1016/j.cbpa.2022.111265

Zhang, J., Li, S., Deng, F., Baikeli, B., Huang, S., Wang, B., & Liu, G. (2019). Higher Expression Levels of Aquaporin Family of Proteins in the Kidneys of Arid-Desert Living Lepus yarkandensis. *Frontiers in Physiology*, *10*. https://www.frontiersin.org/articles/10.3389/fphys.2019.01172

Zhao, E., Stone, M. R., Ren, X., Pulliam, T., Nghiem, P., Bielas, J. H., & Gottardo, R. (2020). *BayesSpace enables the robust characterization of spatial gene expression architecture in tissue sections at increased resolution* (p. 2020.09.04.283812). bioRxiv. https://doi.org/10.1101/2020.09.04.283812

APPENDICES

APPENDIX I: UMAP GRAPHS FOR TISSUE SAMPLES B1 AND C1

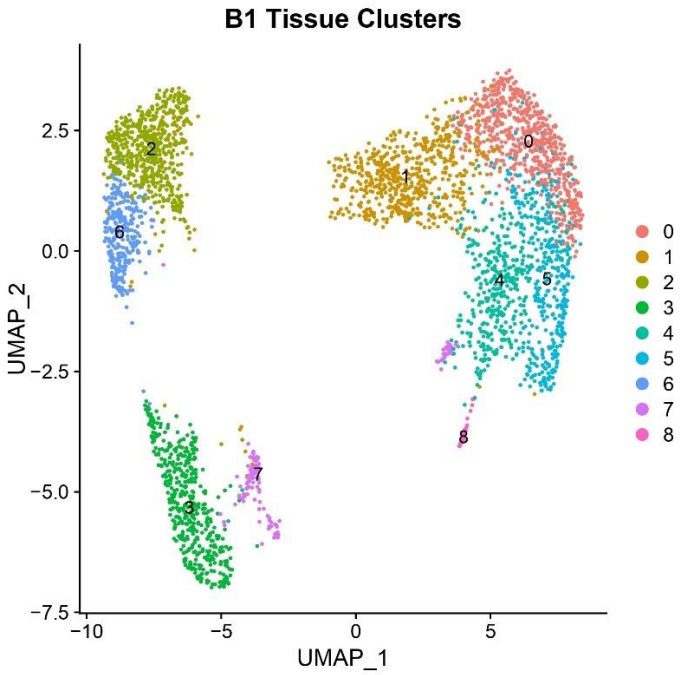

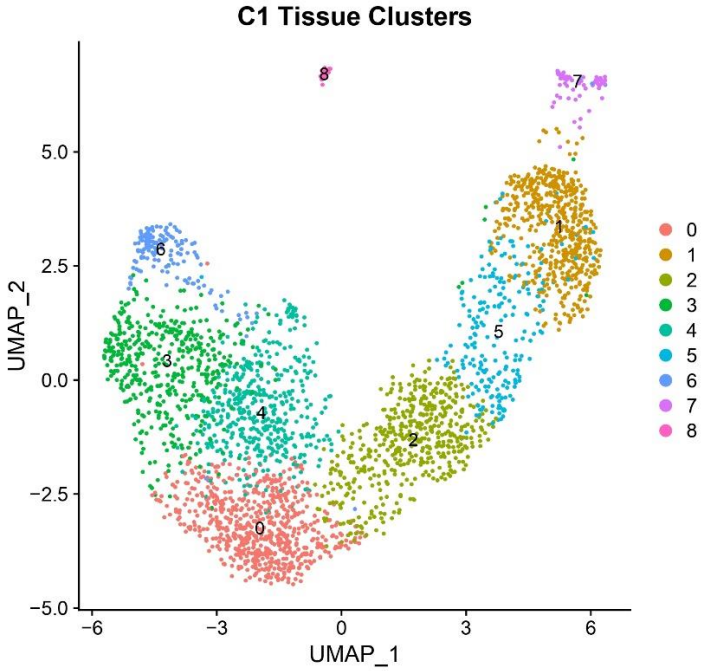

APPENDIX II: SPATIAL CLUSTERING AND TOP 10 HIGHLY EXPRESSED GENES FOR TISSUE SAMPLE B1

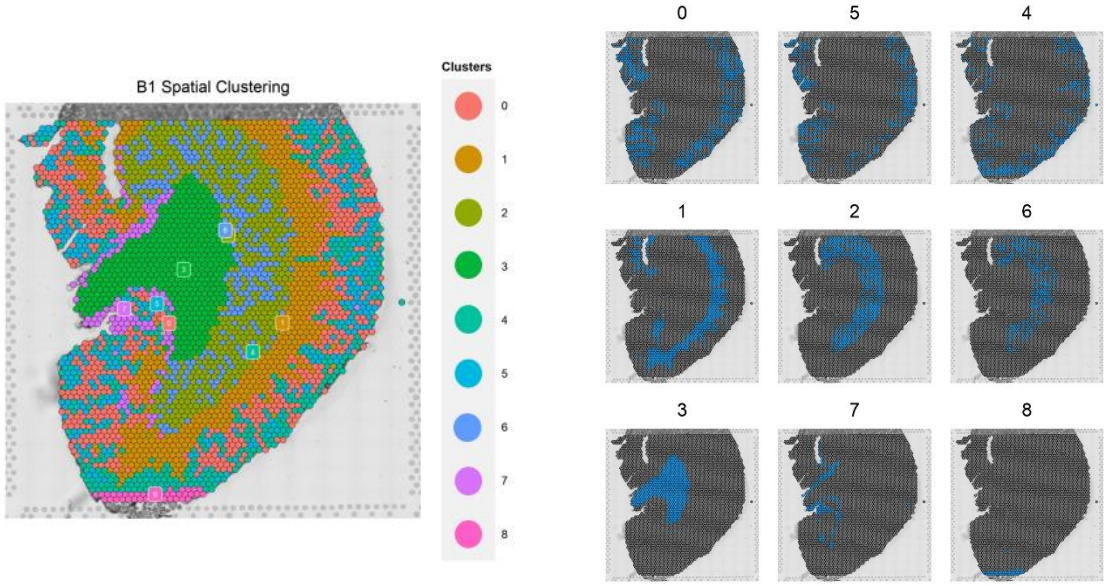

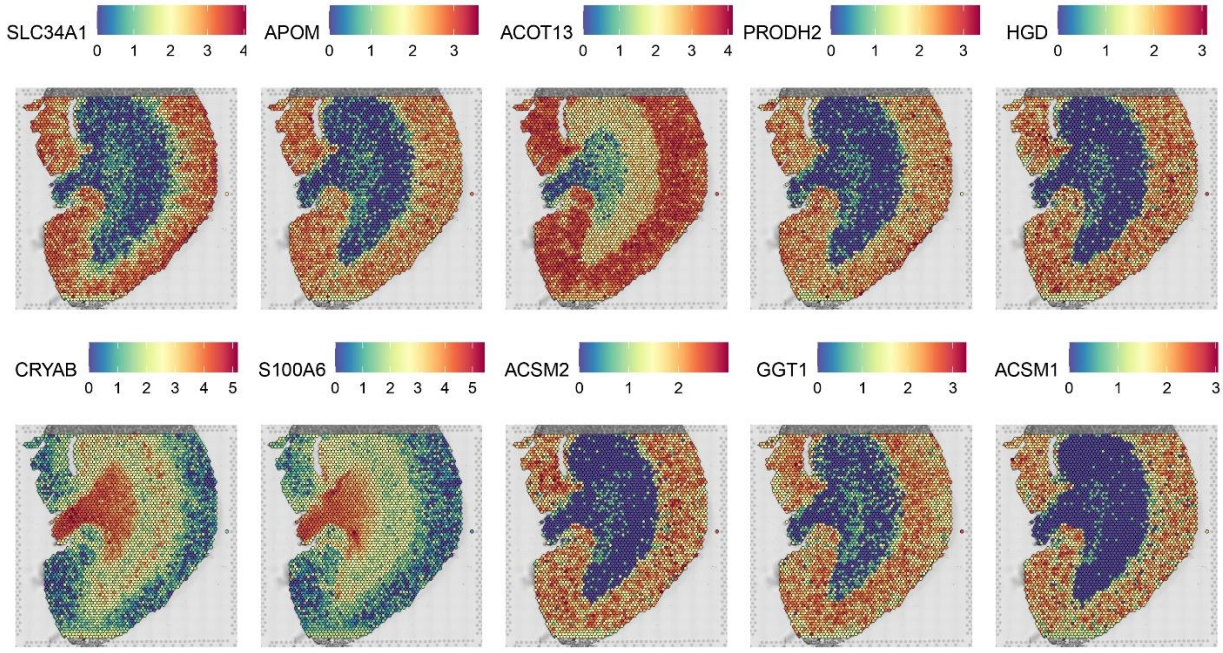

APPENDIX III: SPATIAL CLUSTERING AND TOP 10 HIGHLY EXPRESSED GENES FOR TISSUE SAMPLE C1

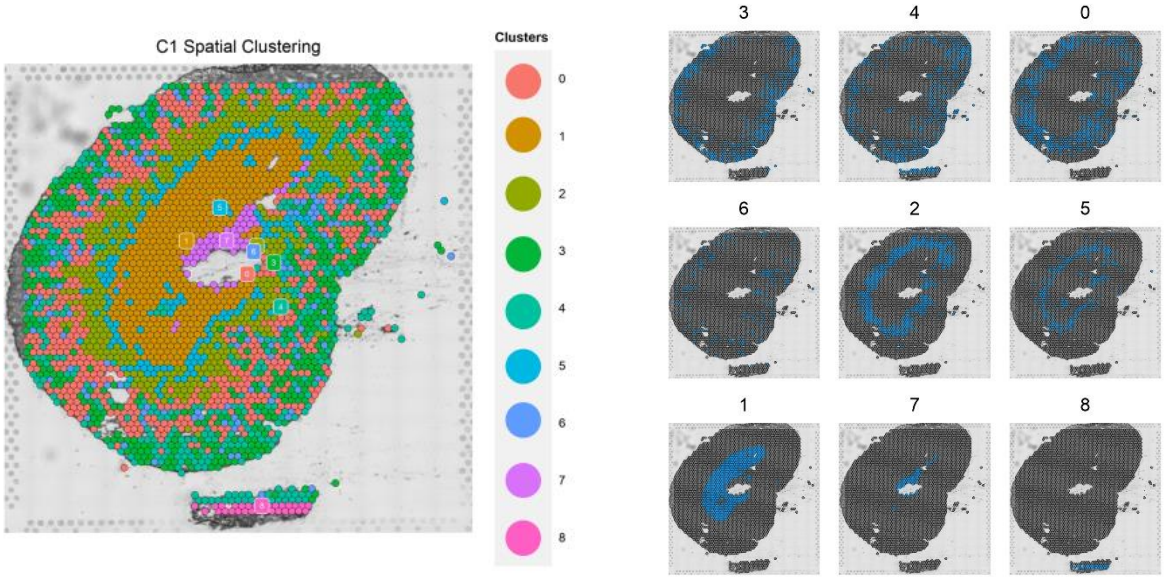

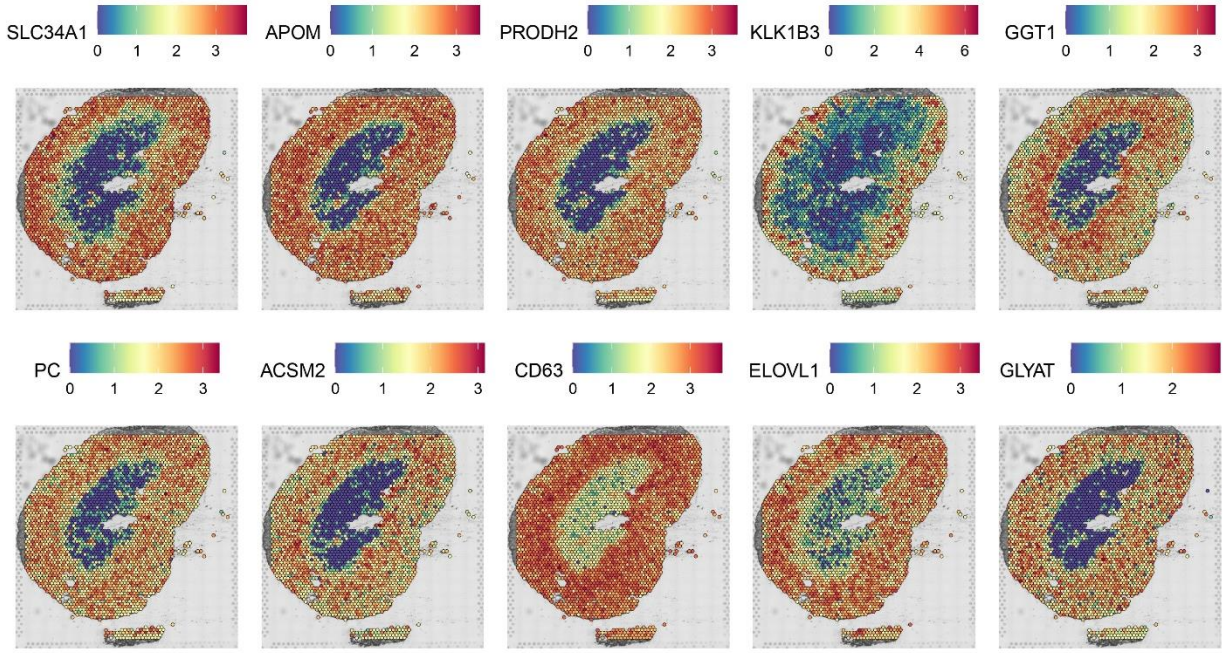

APPENDIX IV: SPATIAL CLUSTERING AND TOP 10 HIGHLY EXPRESSED GENES FOR TISSUE SAMPLE D1

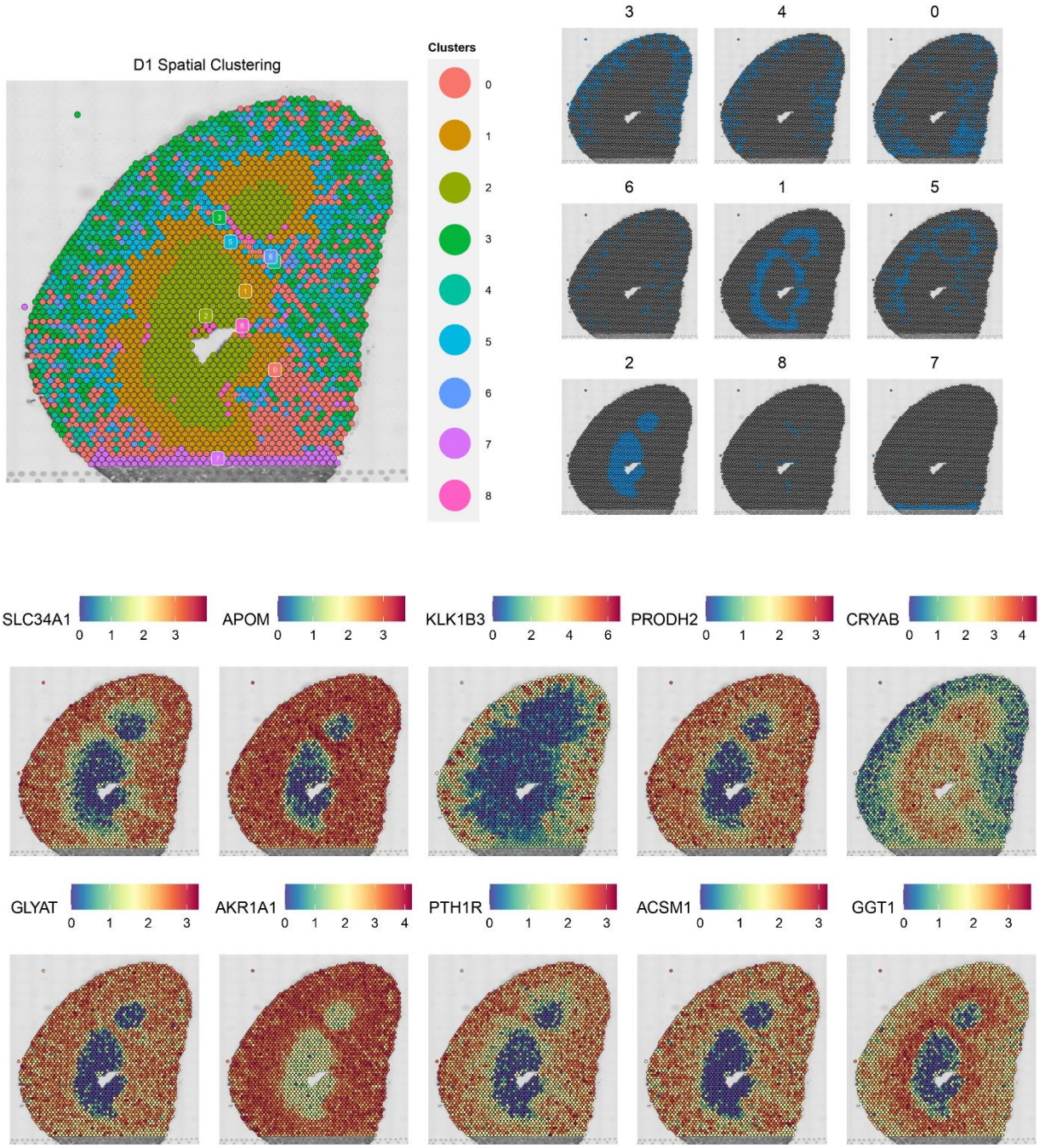

APPENDIX V: CORTEX MARKER GENE SPATIAL LOCATION AND EXPRESSION LEVEL PLOTS FOR TISSUE B1

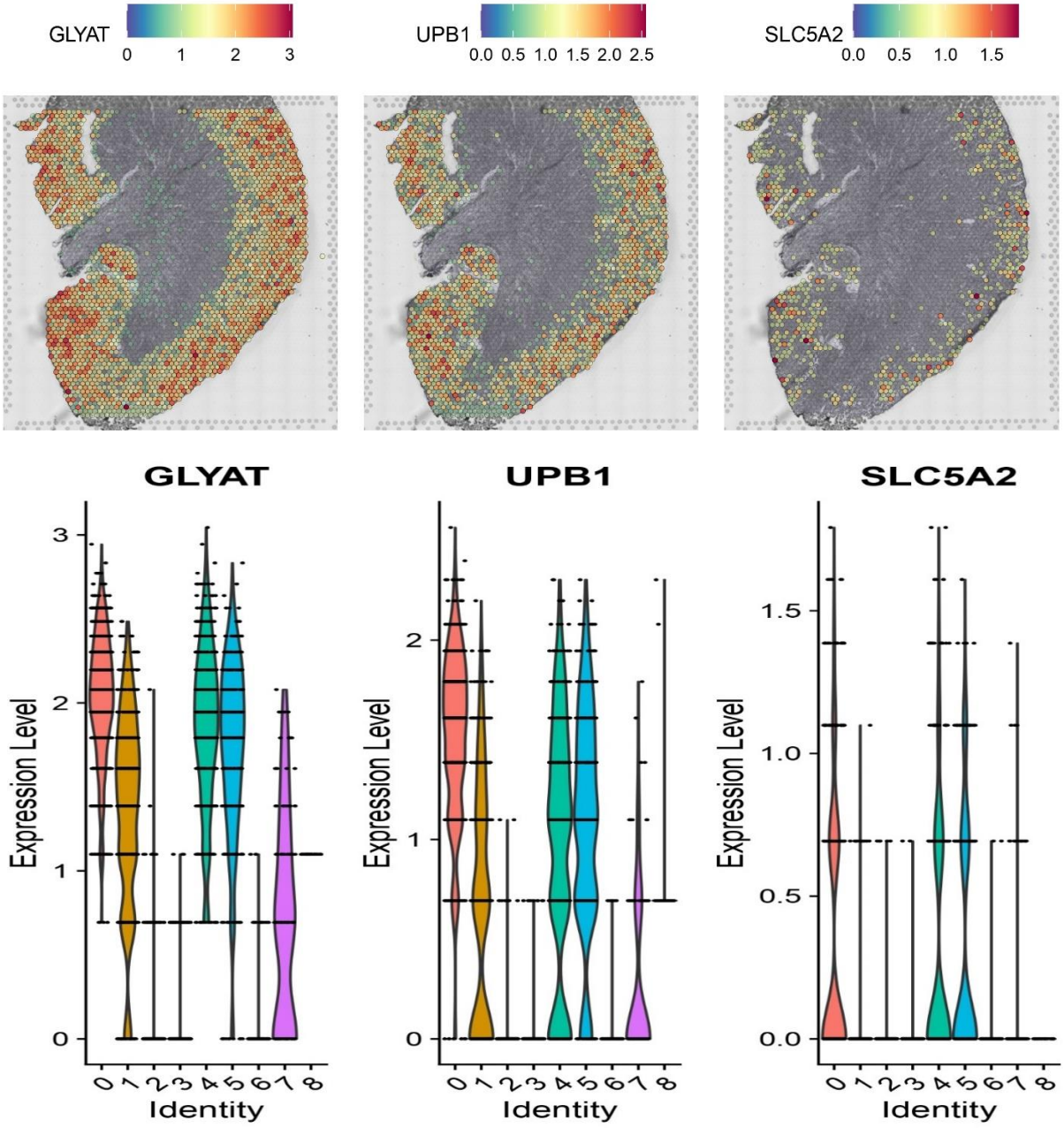

APPENDIX VI: MEDULLARY AND RENAL PELVIS MARKER GENE SPATIAL LOCATION AND EXPRESSION LEVEL PLOTS FOR TISSUE B1

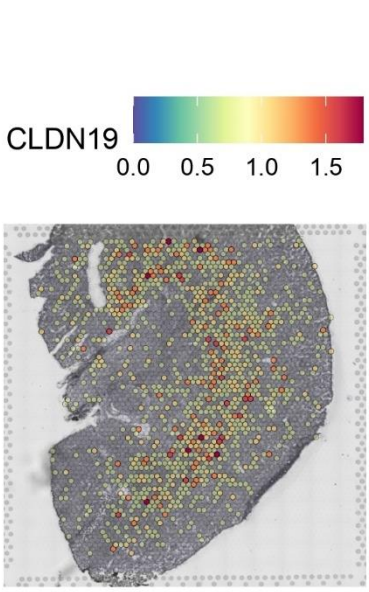

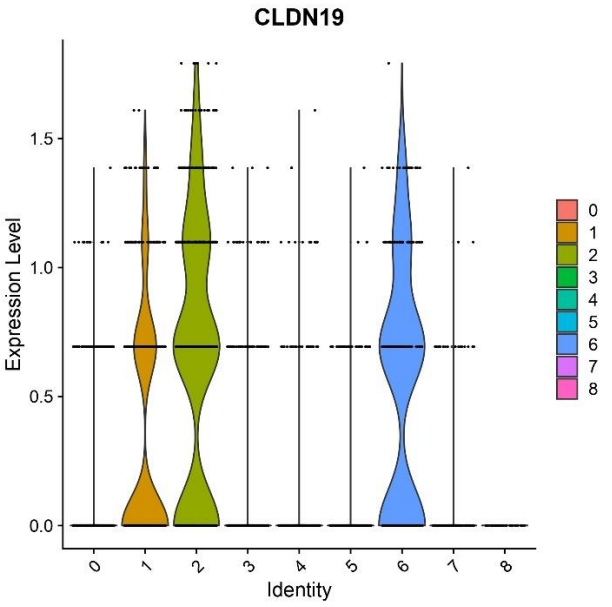

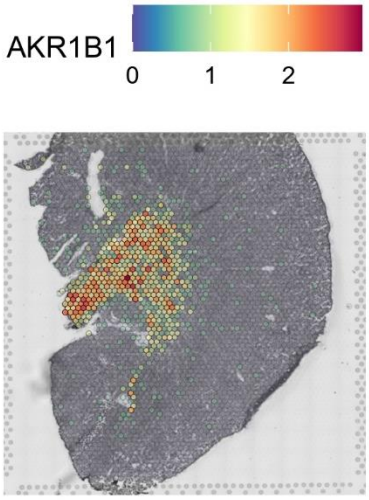

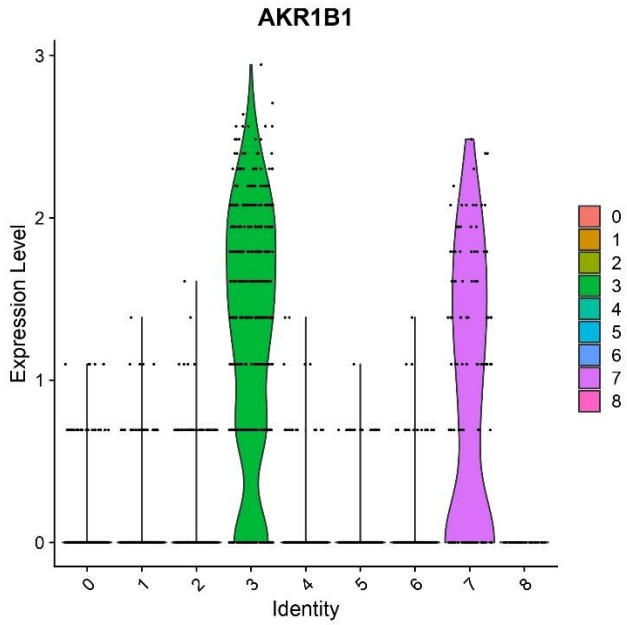

APPENDIX VII: CORTEX MARKER GENE SPATIAL LOCATION AND EXPRESSION LEVEL PLOTS FOR TISSUE C1

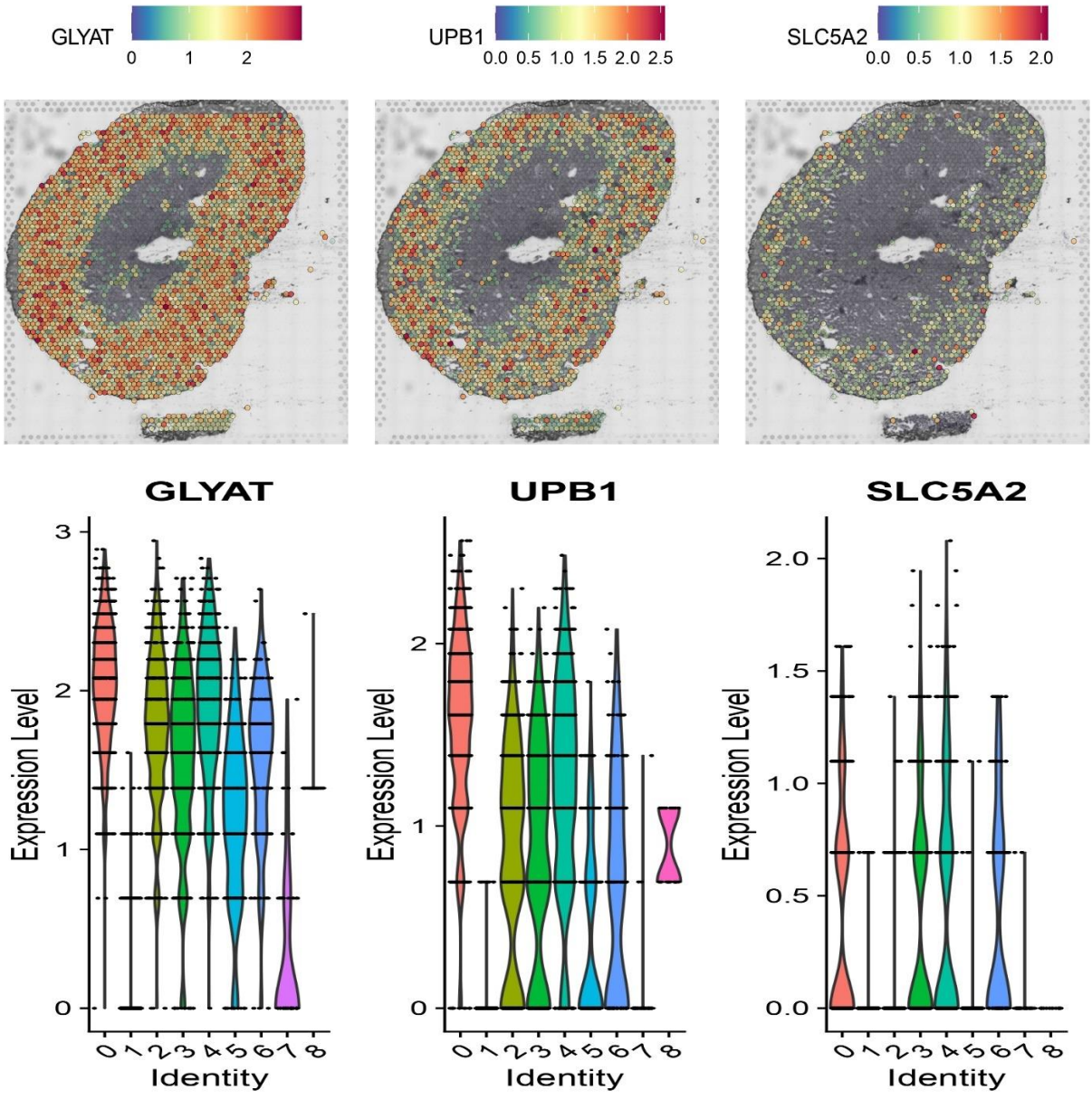

APPENDIX VIII: MEDULLARY AND RENAL PELVIS MARKER GENE SPATIAL LOCATION AND EXPRESSION LEVEL PLOTS FOR TISSUE C1

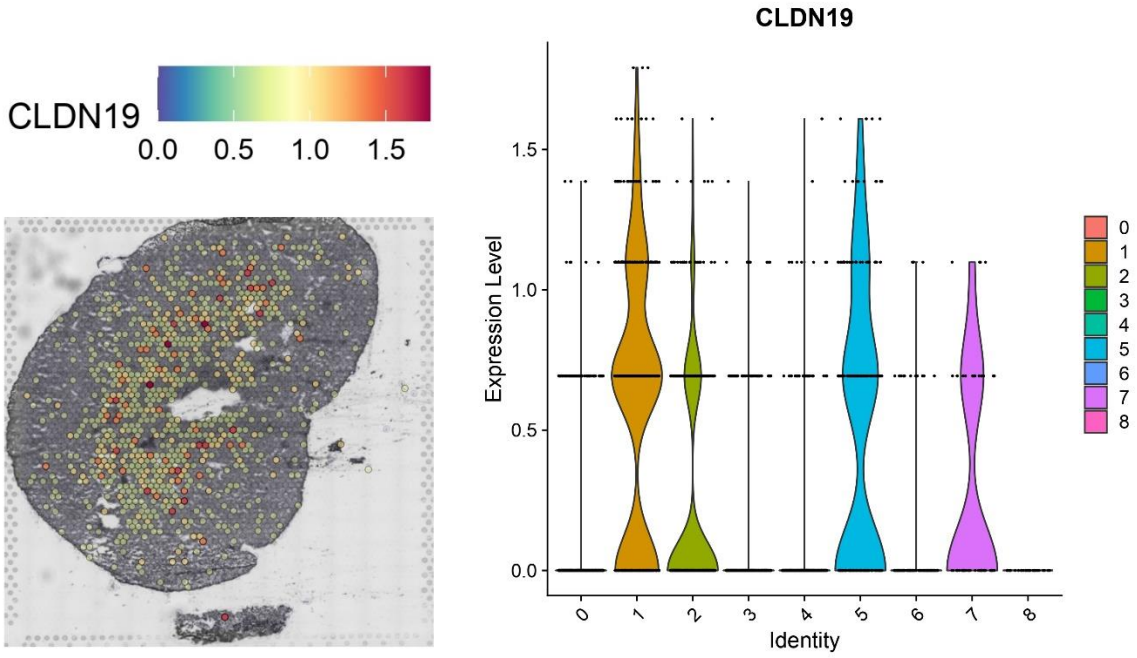

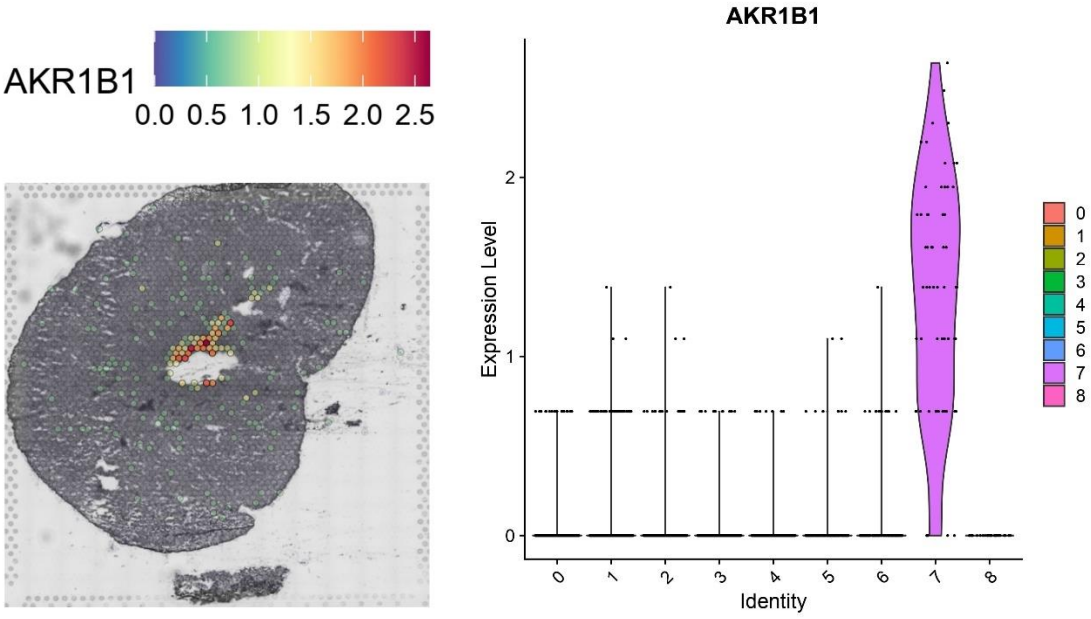

APPENDIX IX: CORTEX MARKER GENE SPATIAL LOCATION AND EXPRESSION LEVEL PLOTS FOR TISSUE D1

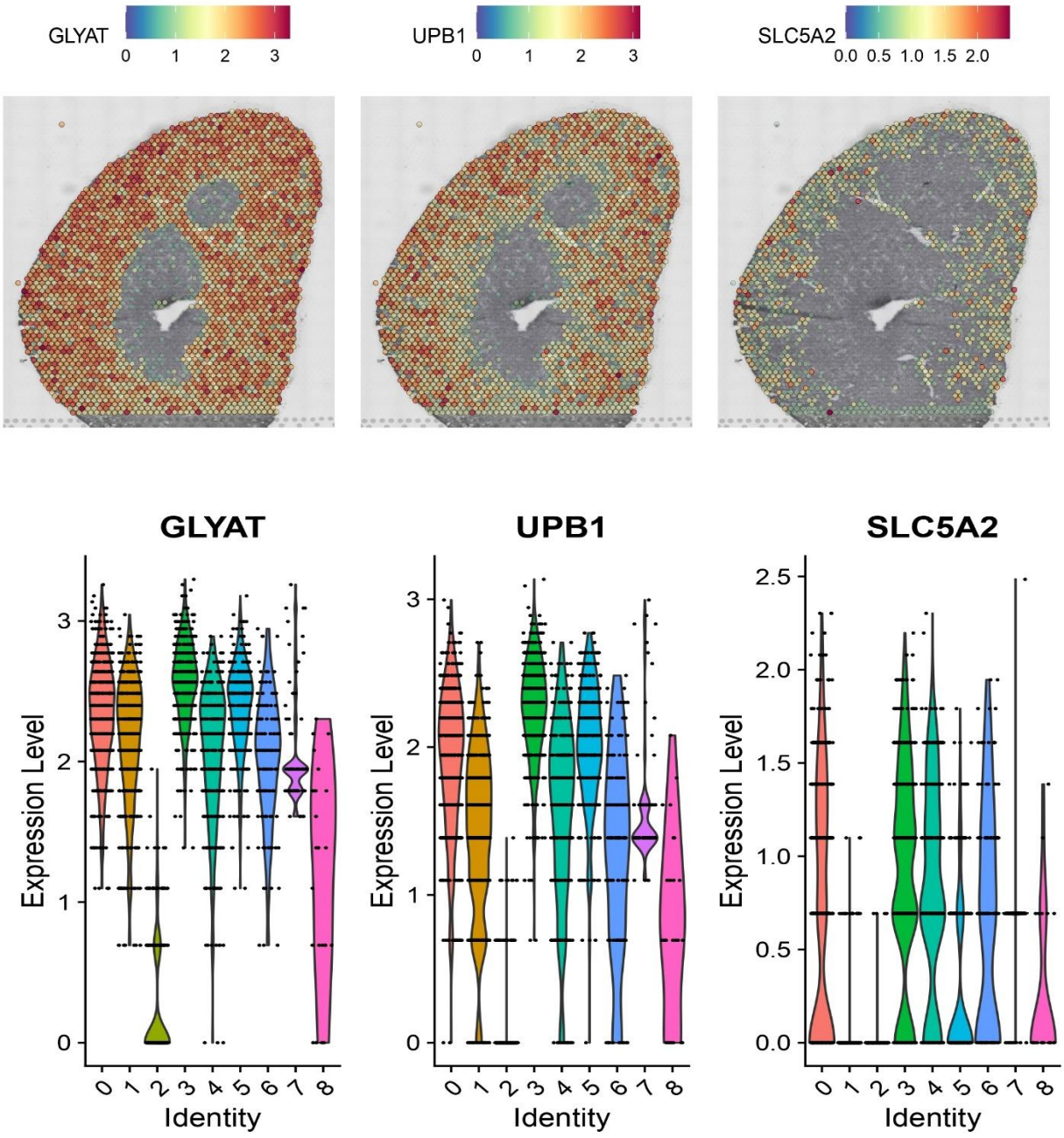

APPENDIX X: MEDULLARY AND RENAL PELVIS MARKER GENE SPATIAL LOCATION AND EXPRESSION LEVEL PLOTS FOR TISSUE D1

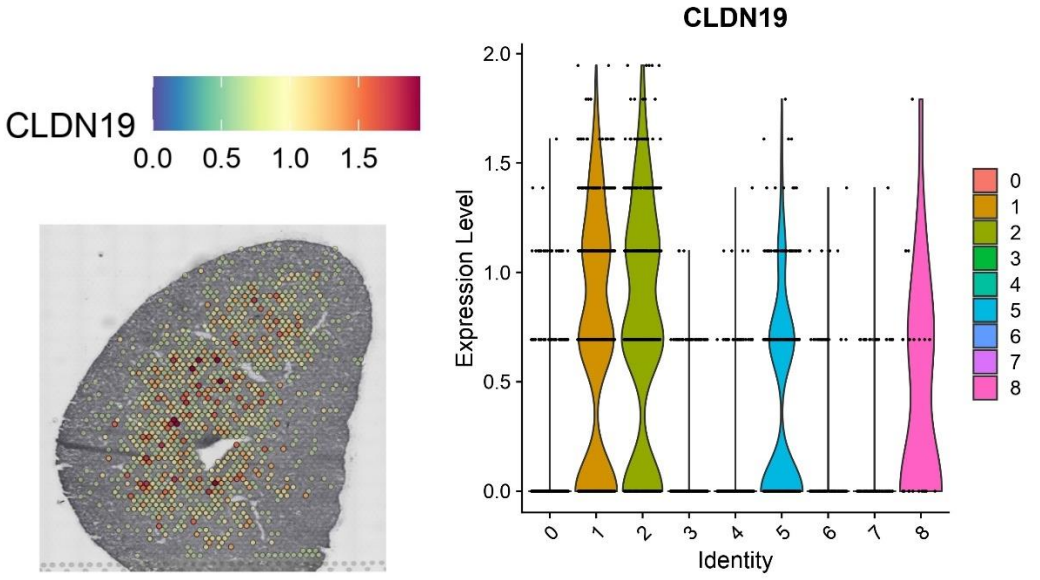

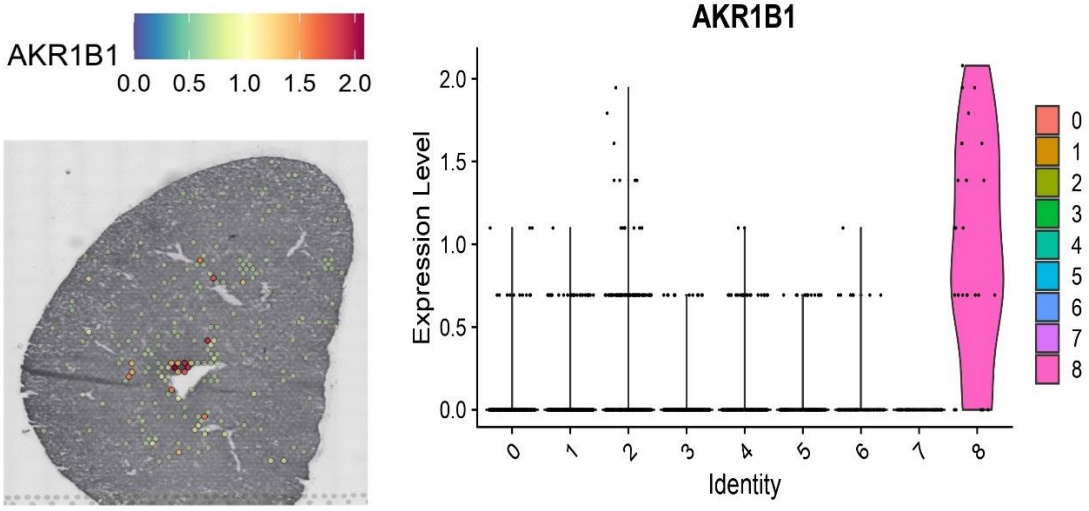

APPENDIX XI: GENE MARKER MAPS OF MAJOR CELL TYPES IN THE KIDNEY FOR TISSUE B1

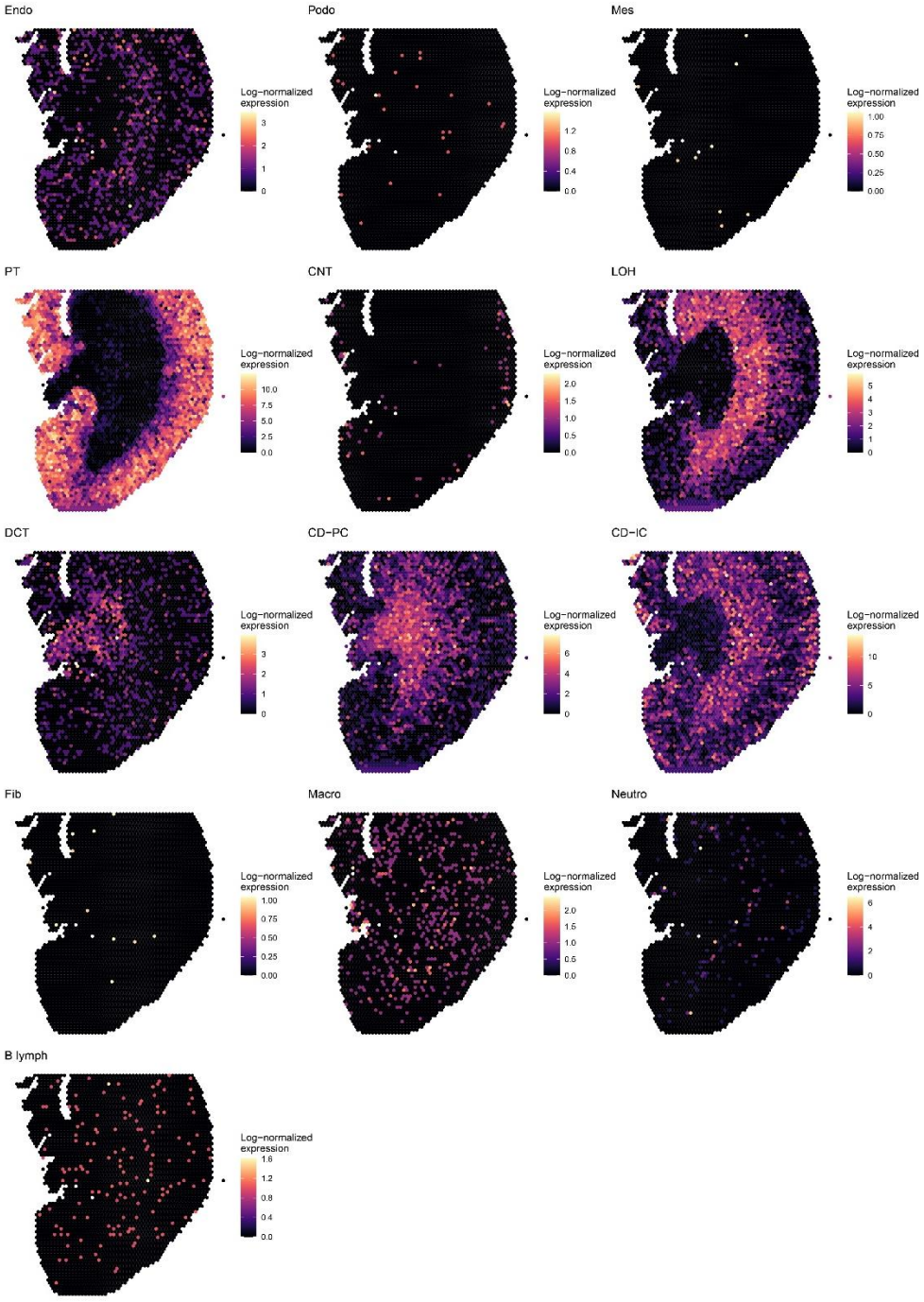

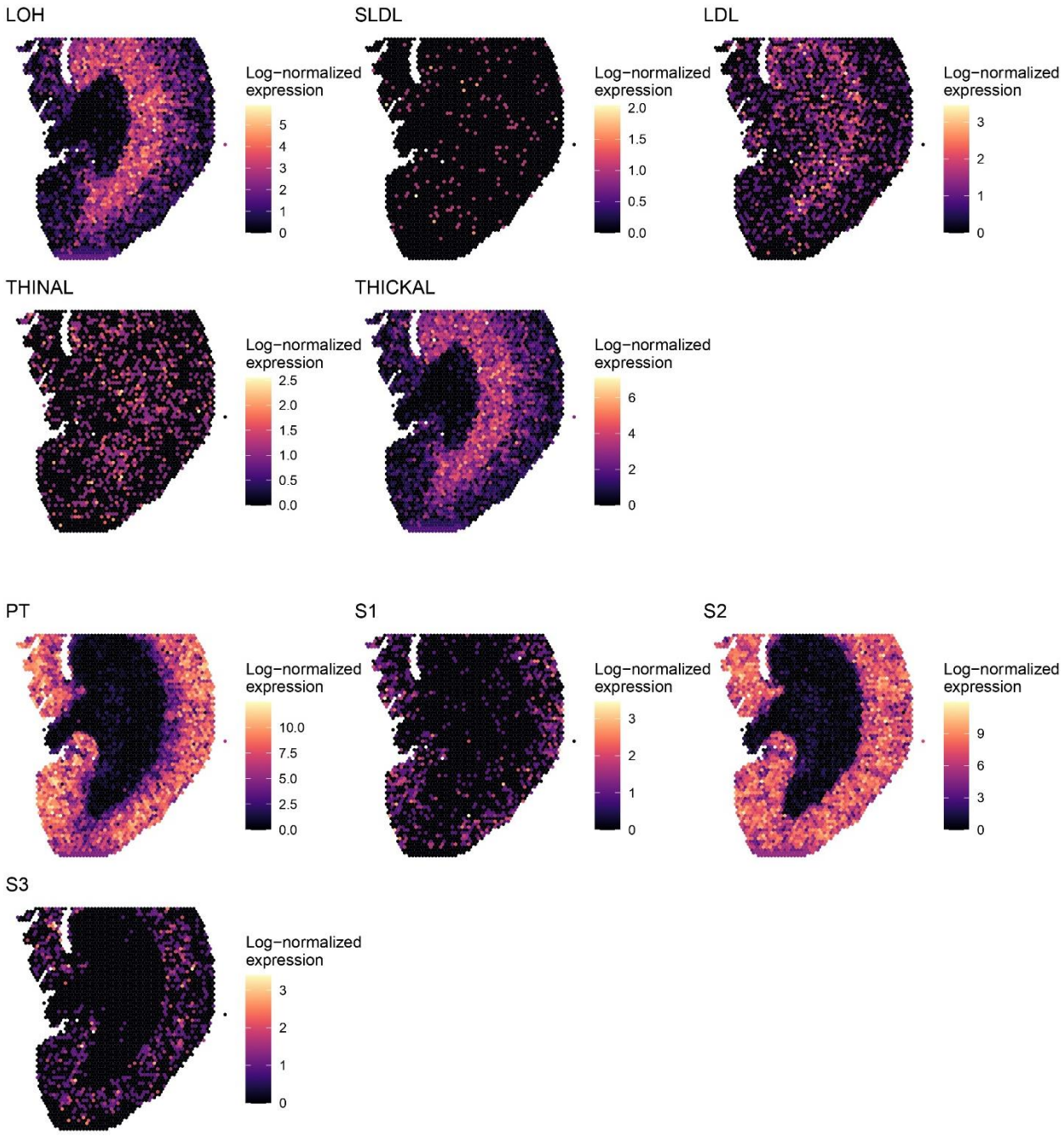
LOH
Log−normalized expression
5
4
3
2
1
0
SLDL
Log−normalized expression
2.0
1.5
1.0
0.5
0.0
LDL
Log−normalized expression
3
2
1
0
THINAL
Log−normalized expression
2.5
2.0
1.5
1.0
0.5
0.0
THICKAL
Log−normalized expression
6
4
2
0
PT
Log−normalized expression
10.0
7.5
5.0
2.5
0.0
S1
Log−normalized expression
3
2
1
0
S2
Log−normalized expression
9
6
3
0
S3
Log−normalized expression
3
2
1
0

APPENDIX XII: GENE MARKER MAPS OF MAJOR CELL TYPES IN THE KIDNEY FOR TISSUE C1

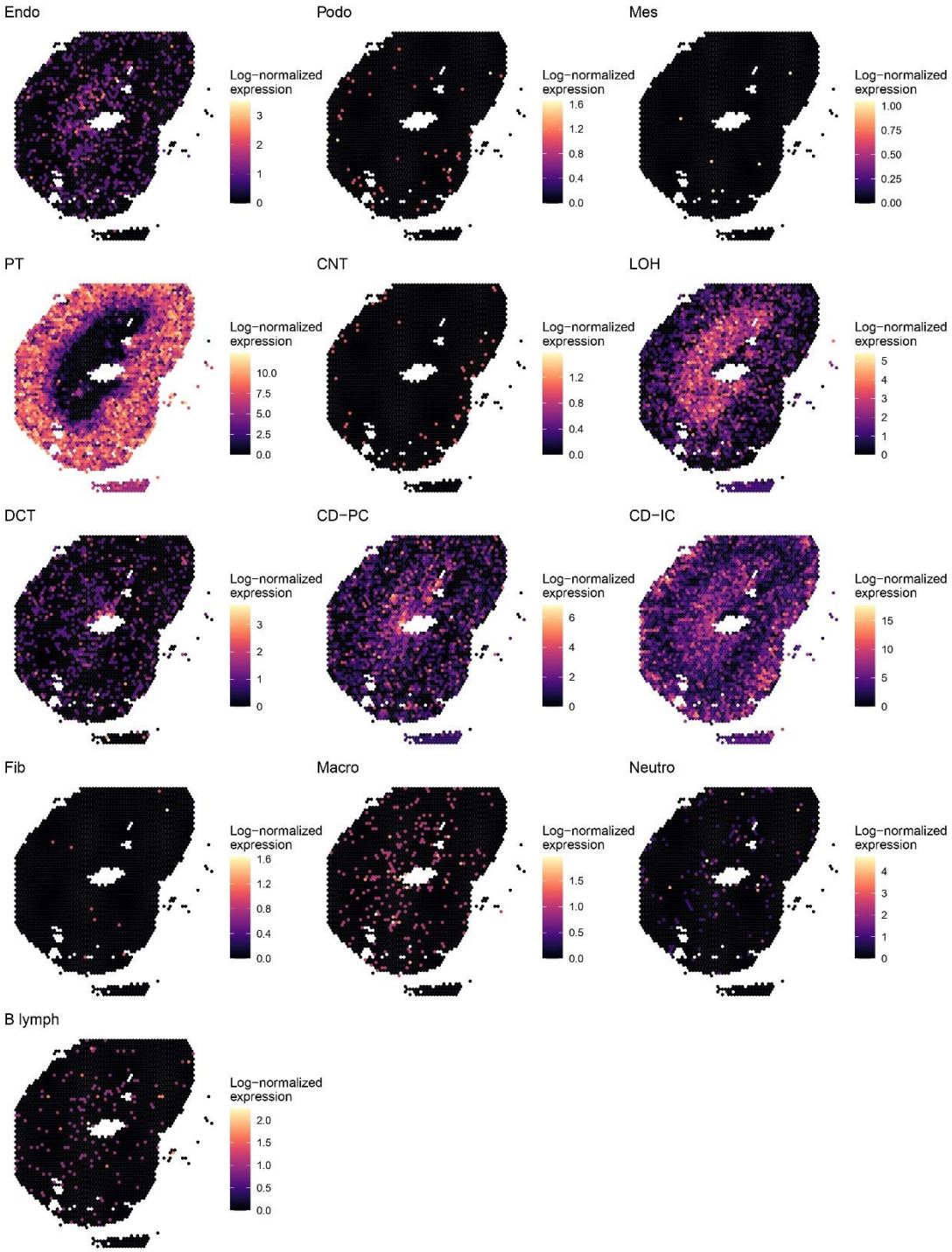

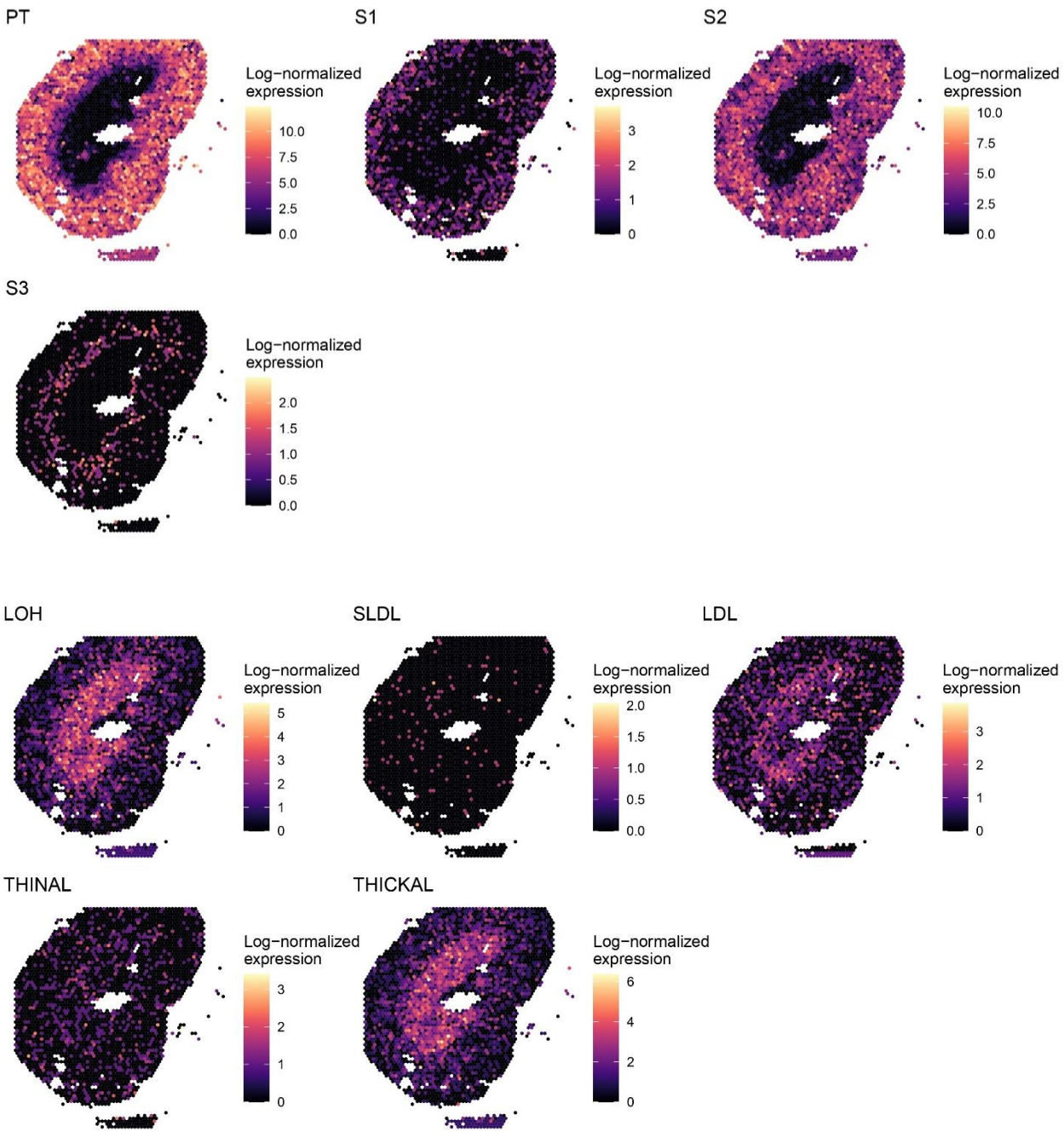
PT
Log−normalized expression
10.0
7.5
5.0
2.5
0.0
S1
Log−normalized expression
3
2
1
0
S2
Log−normalized expression
10.0
7.5
5.0
2.5
0.0
S3
Log−normalized expression
2.0
1.5
1.0
0.5
0.0
LOH
Log−normalized expression
5
4
3
2
1
0
SLDL
Log−normalized expression
2.0
1.5
1.0
0.5
0.0
LDL
Log−normalized expression
3
2
1
0
THINAL
Log−normalized expression
3
2
1
0
THICKAL
Log−normalized expression
6
4
2
0

APPENDIX XIII: GENE MARKER MAPS OF MAJOR CELL TYPES IN THE KIDNEY FOR TISSUE D1

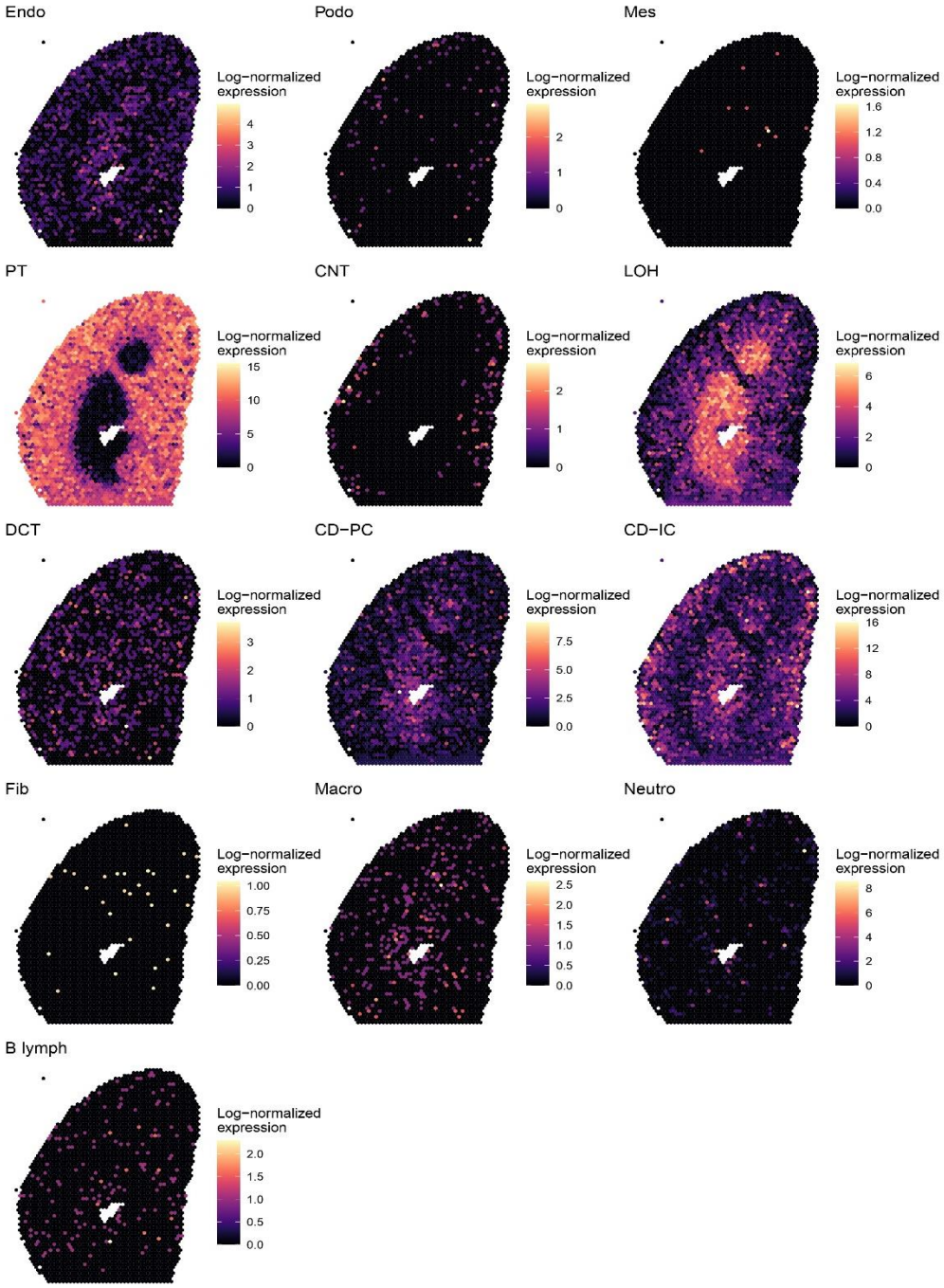

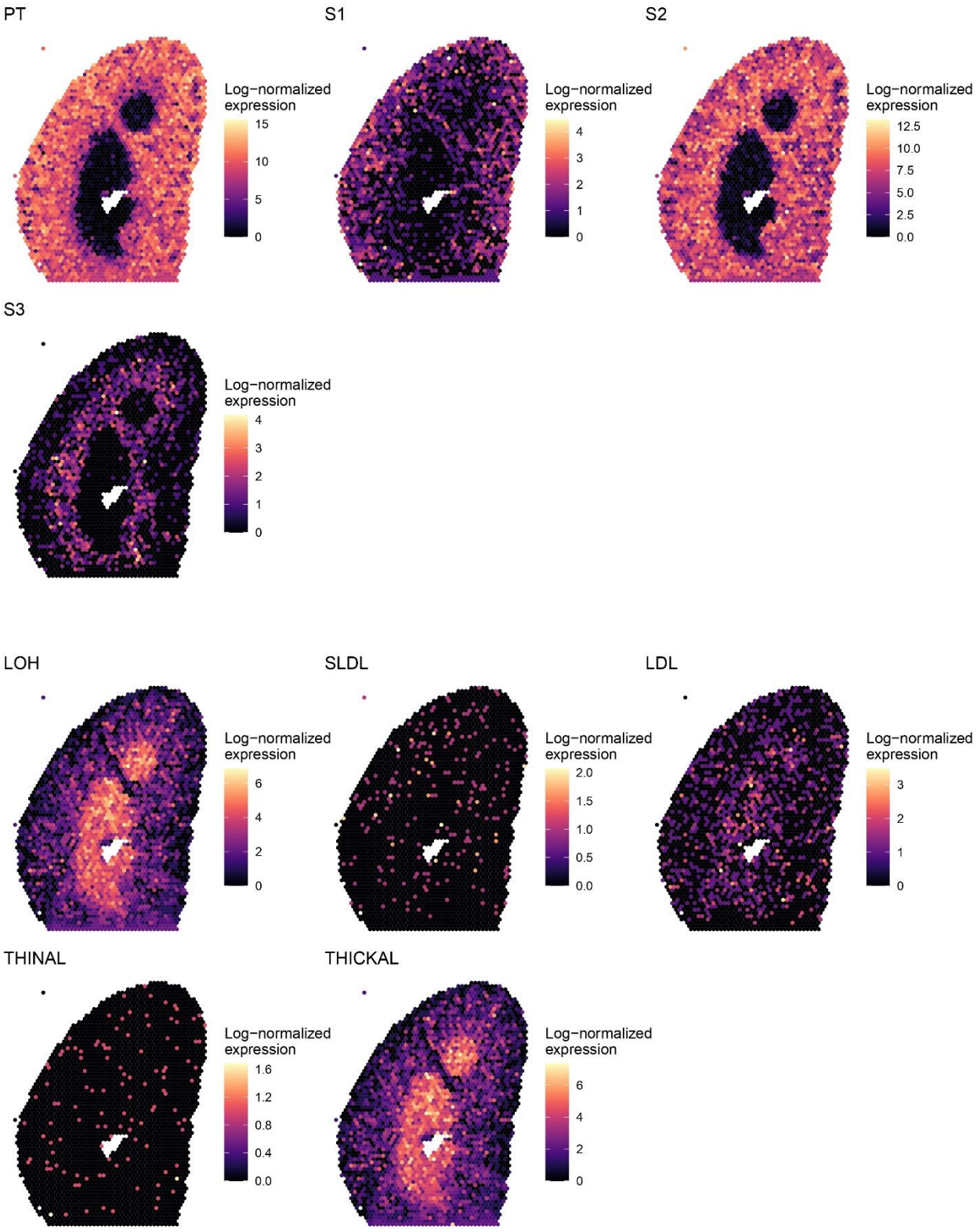
PT
Log−normalized expression
15
10
5
0
S1
Log−normalized expression
4
3
2
1
0
S2
Log−normalized expression
12.5
10.0
7.5
5.0
2.5
0.0
S3
Log−normalized expression
4
3
2
1
0
LOH
Log−normalized expression
6
4
2
0
SLDL
Log−normalized expression
2.0
1.5
1.0
0.5
0.0
LDL
Log−normalized expression
3
2
1
0
THINAL
Log−normalized expression
1.6
1.2
0.8
0.4
0.0
THICKAL
Log−normalized expression
6
4
2
0

APPENDIX XIV: SODIUM RELATED GENE LOG NORMALIZED EXPRESSION VALUE VIOLIN PLOTS FOR TISSUE B1

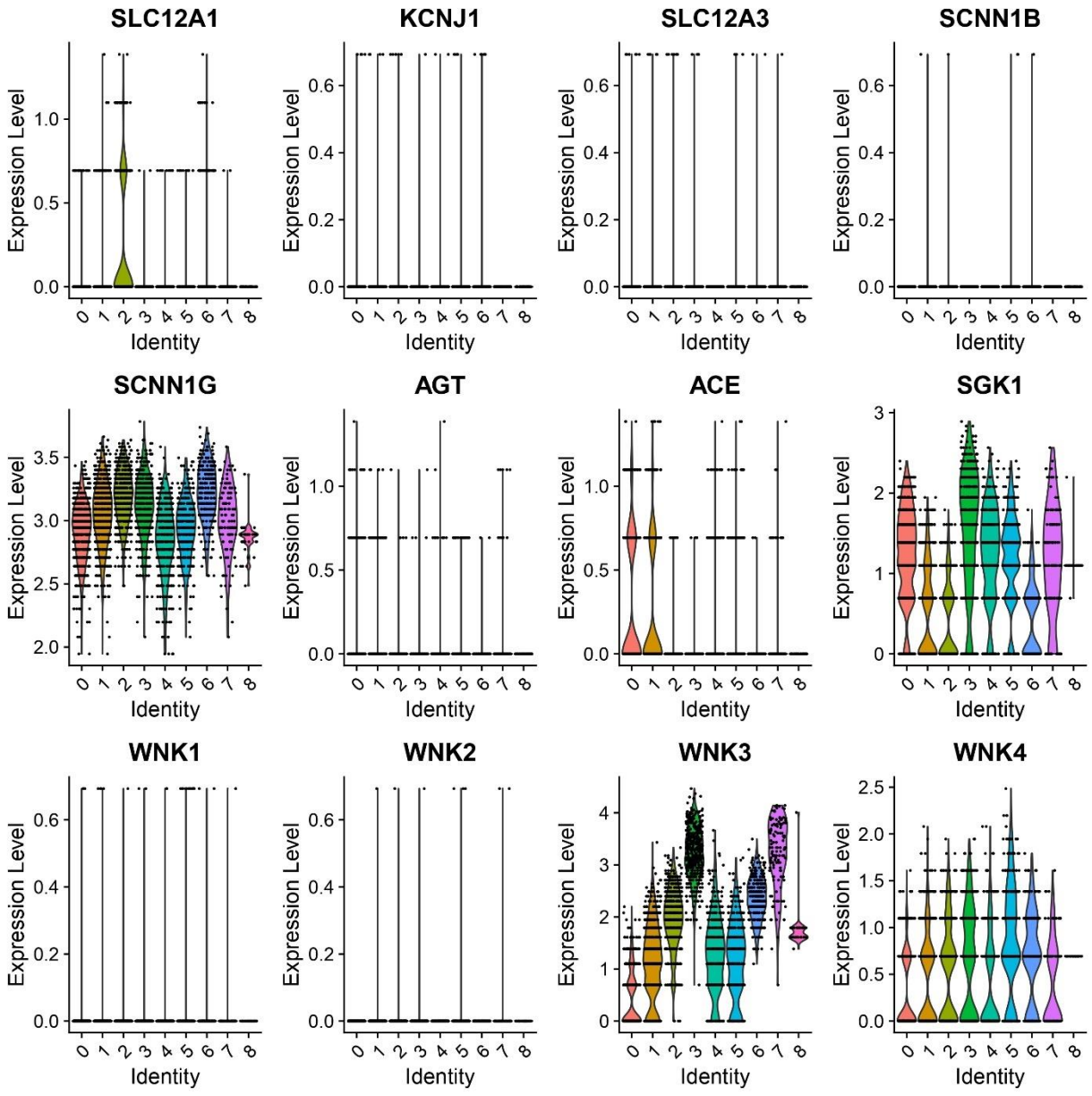

APPENDIX XV: SODIUM RELATED GENE LOG NORMALIZED EXPRESSION VALUE VIOLIN PLOTS FOR TISSUE C1

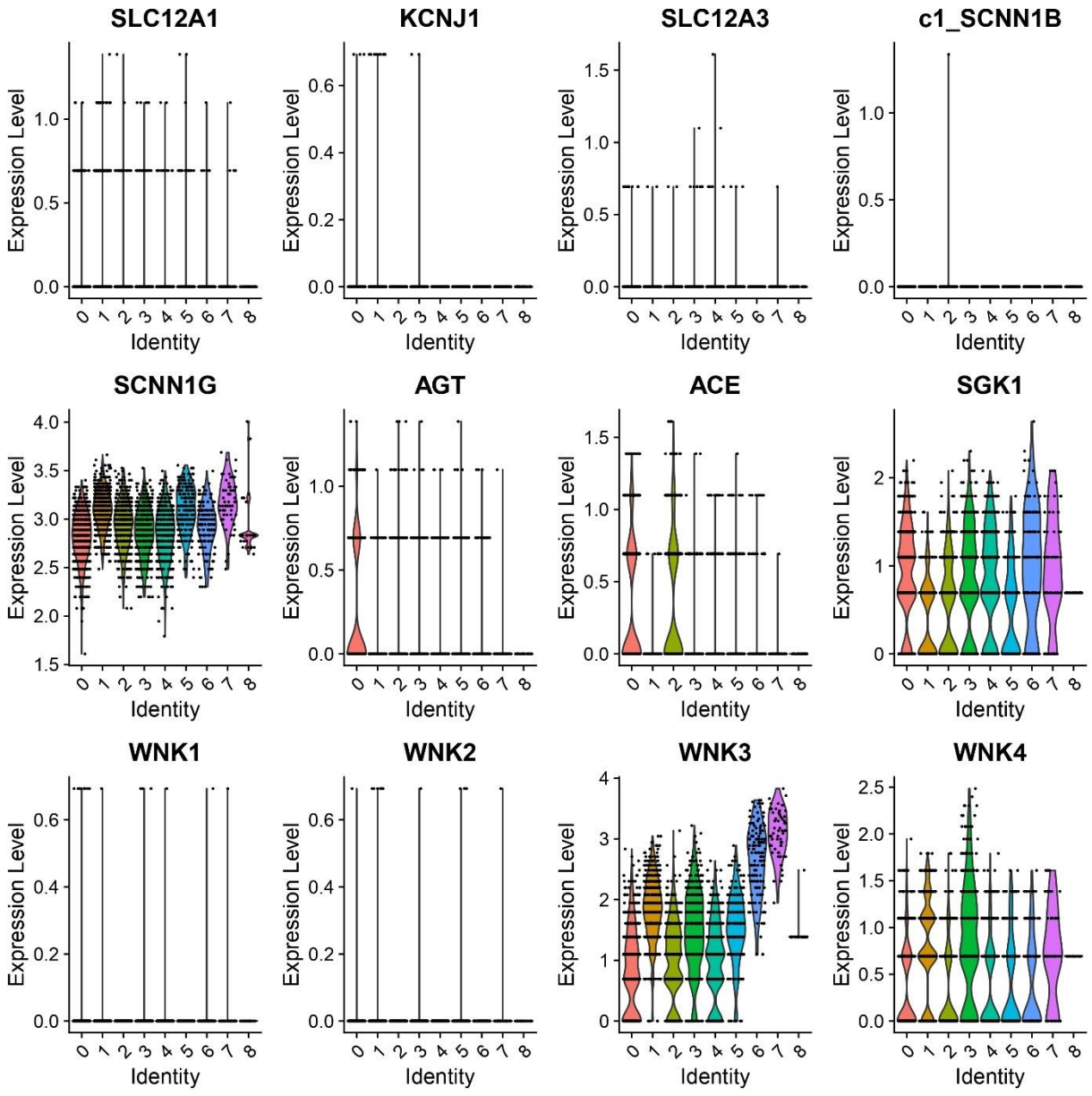

APPENDIX XVI: SODIUM RELATED GENE LOG NORMALIZED EXPRESSION VALUE VIOLIN PLOTS FOR TISSUE D1

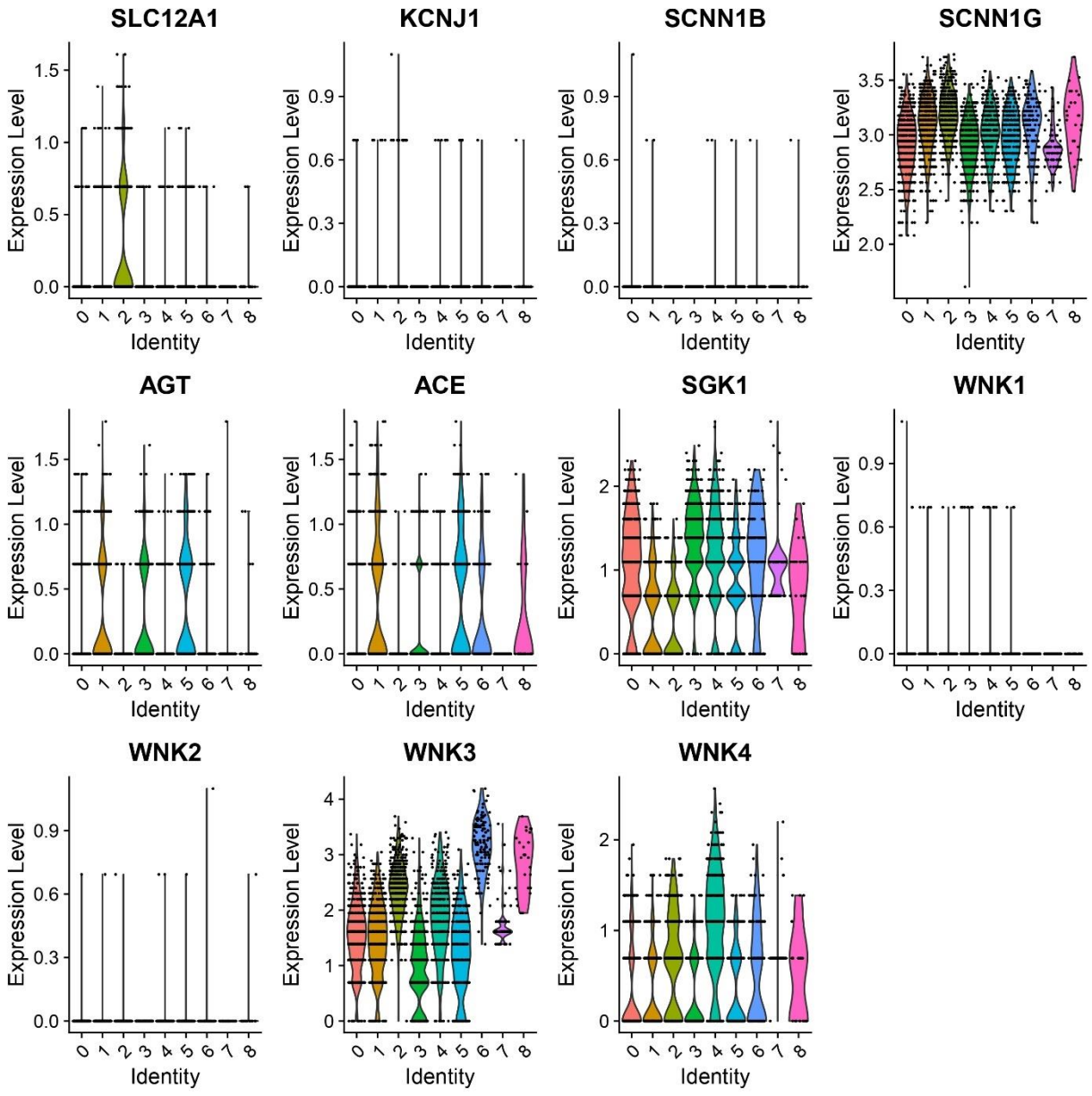

APPENDIX XVII: AQP GENE FAMILY LOG NORMALIZED EXPRESSION VALUE VIOLIN PLOTS FOR TISSUE B1

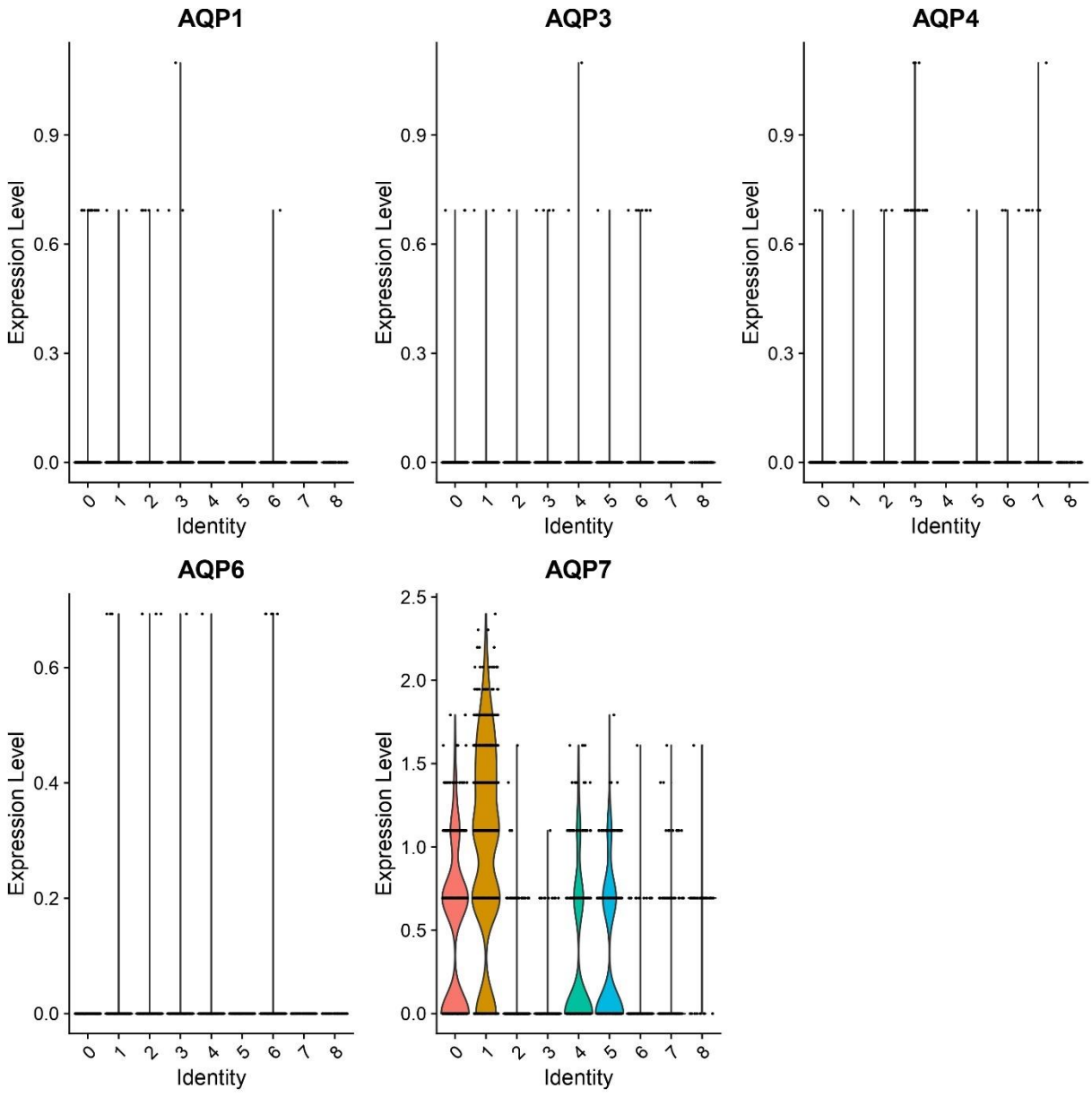

APPENDIX XVIII: AQP GENE FAMILY LOG NORMALIZED EXPRESSION VALUE VIOLIN PLOTS FOR TISSUE C1

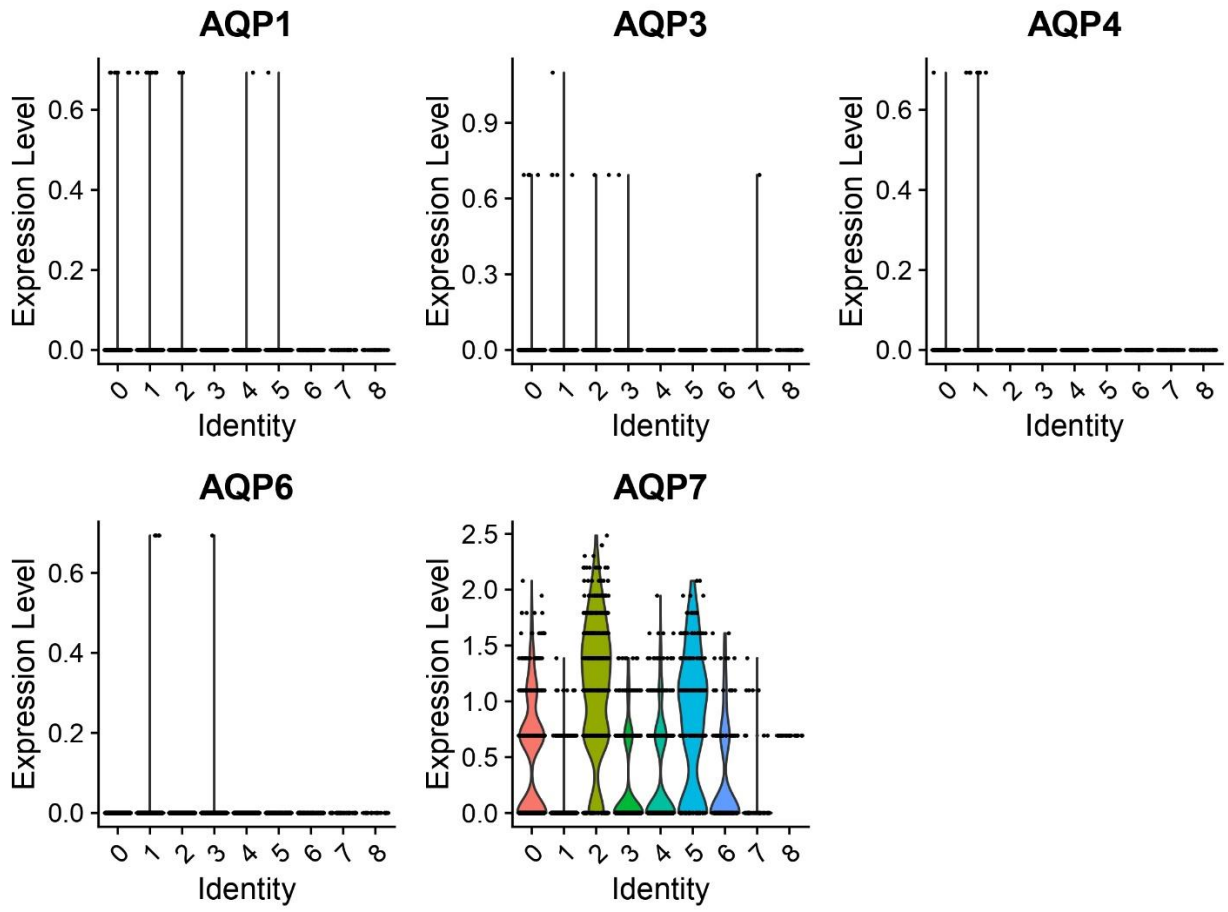

APPENDIX XIX: AQP GENE FAMILY LOG NORMALIZED EXPRESSION VALUE VIOLIN PLOTS FOR TISSUE D1

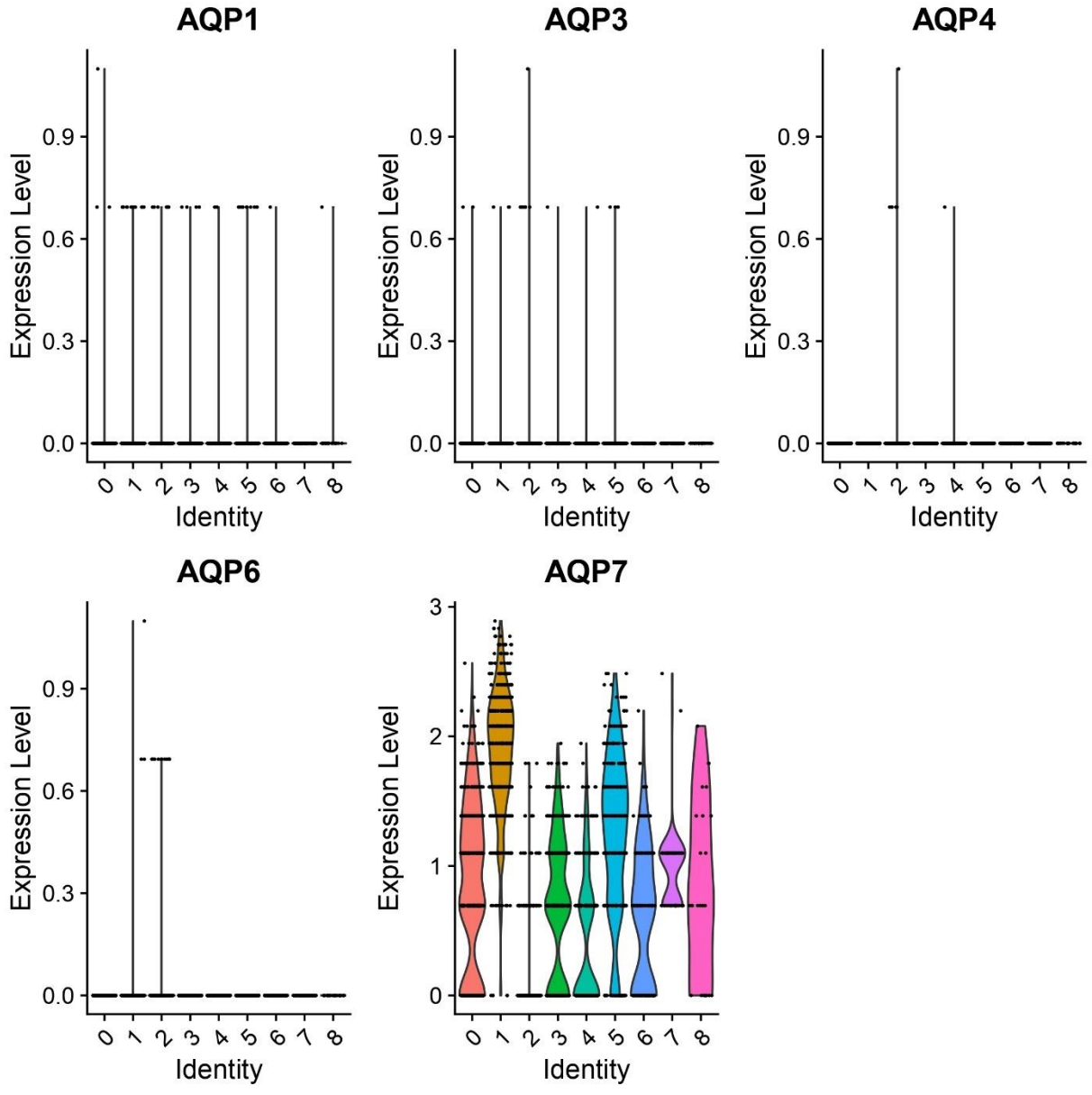

APPENDIX XX: AVERAGE LOG2 FOLD CHANGE HEATMAP OF TOP 10 GENES PER CLUSTER FOR TISSUE B1

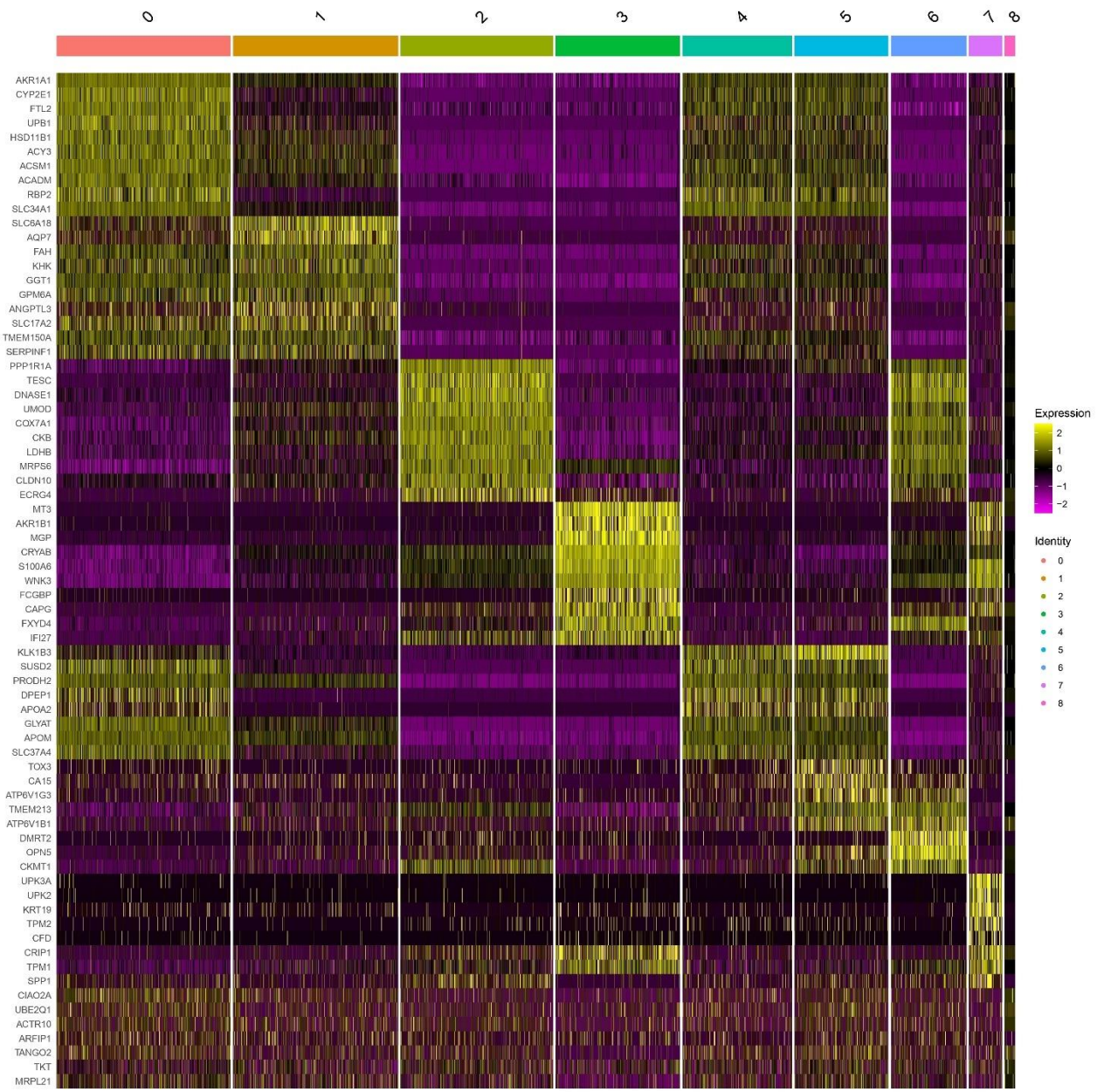

APPENDIX XXI: AVERAGE LOG2 FOLD CHANGE HEATMAP OF TOP 10 GENES PER CLUSTER FOR TISSUE C1

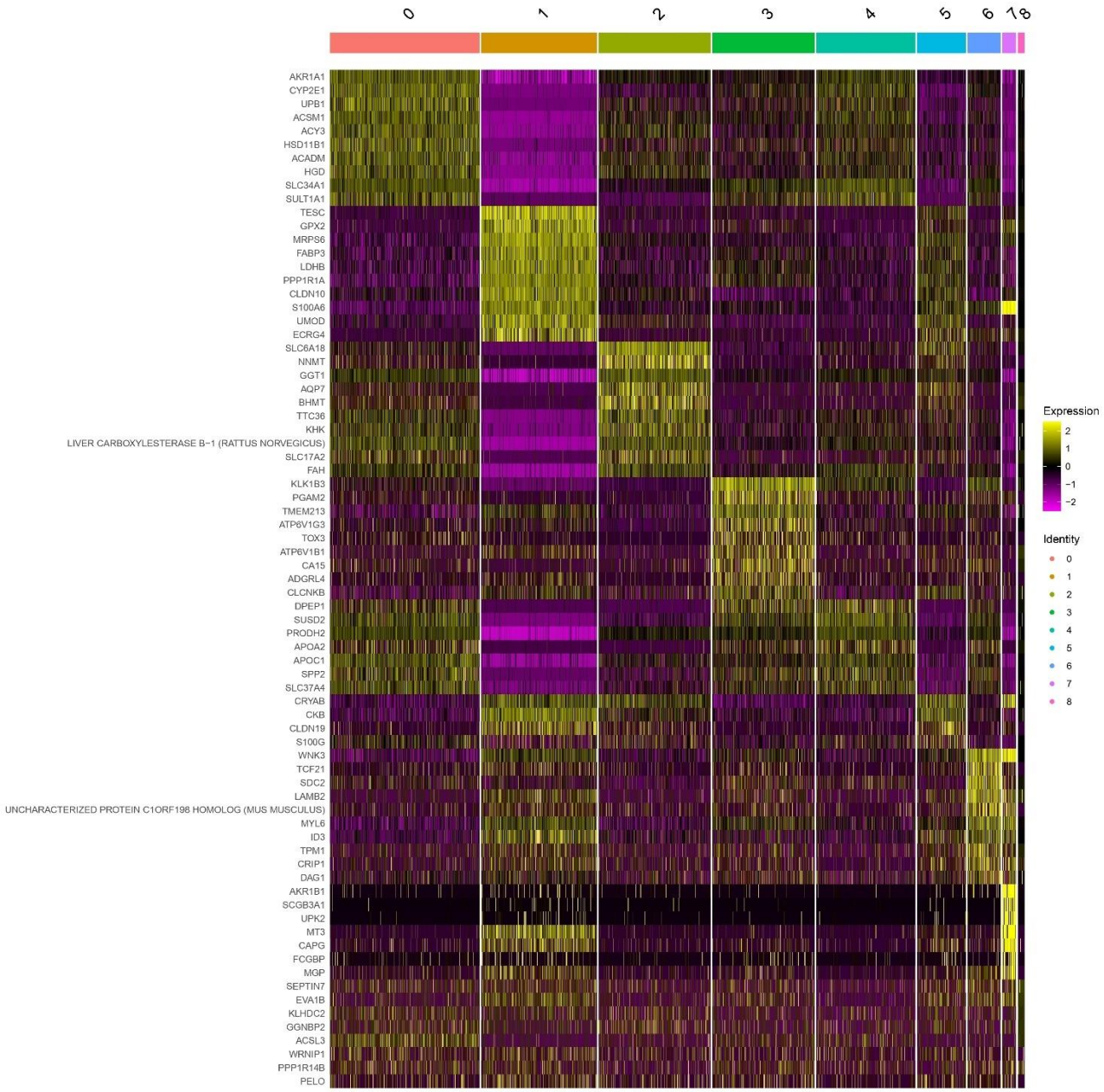

APPENDIX XXII: AVERAGE LOG2 FOLD CHANGE HEATMAP OF TOP 10 GENES PER CLUSTER FOR TISSUE D1

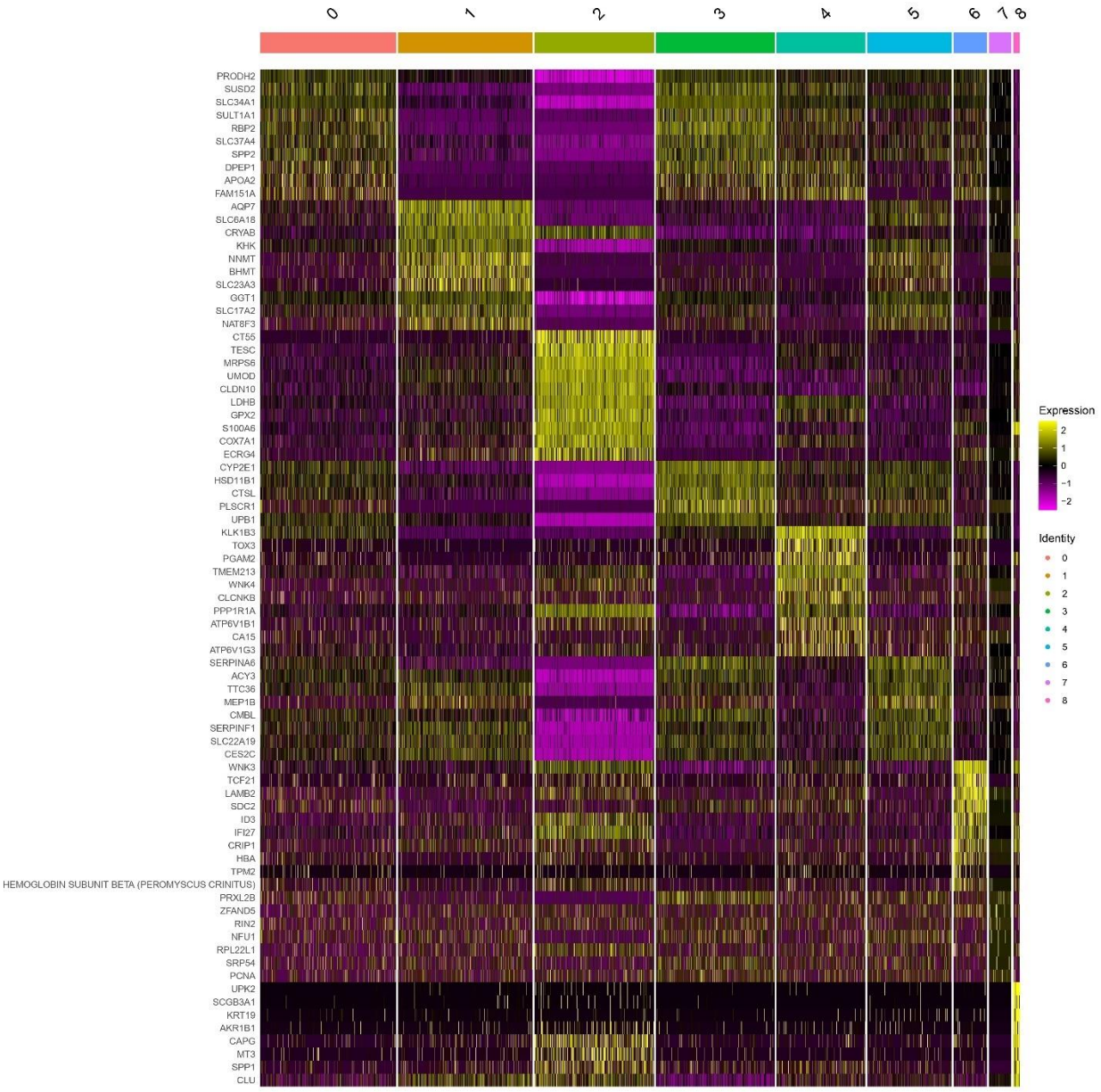

APPENDIX XXIII: GO TERMS FOR TOP 10 GENES PER CLUSTER FOR TISSUE A1

Go Term	GO ID	Cluster(s) associated	P-Value
Molecular Function			
phosphatase inhibitor activity	GO:0019212	0	2.2e-2
fumarylacetoacetase activity	GO:0004334	1	4.9e-2
ketohexokinase activity	GO:0004454	1	4.9e-2
nicotinamide N-methyltransferase activity	GO:0008112	1	4.9e-2
serpin family protein binding	GO:0097655	2	4.9e-2
beta-ureidopropionase activity	GO:0003837	2	4.9e-2
glucuronolactone reductase activity	GO:0047941	2	4.9e-2
11-beta-hydroxysteroid dehydrogenase (NADP+) activity	GO:0070524	2	4.9e-2
cortisol dehydrogenase activity	GO:0102196	2	4.9e-2
methylglyoxal reductase (NADPH-dependent, acetol producing)	GO:1990002	2	4.9e-2
mevaldate reductase (NADPH) activity	GO:0019726	2	4.9e-2
4-nitrophenol 2-monooxygenase activity	GO:0018601	2	4.9e-2
7-beta-hydroxysteroid dehydrogenase (NADP+) activity	GO:0047022	2	4.9e-2
mevaldate reductase activity	GO:0004495	2	4.9e-2
oxidoreductase activity, acting on NAD(P)H, nitrogenous group as acceptor	GO:0016657	2	4.9e-2
monoatomic ion transmembrane transporter activity	GO:0015075	6	9.0e-3
transmembrane transporter activity	GO:0022857	6	4.8e-2
Biological Process			
intracellular sodium ion homeostasis	GO:0006883	0	3.4e-2
carbohydrate derivative metabolic process	GO:1901135	2	2.6e-4
carboxylic acid metabolic process	GO:0019752	2	7.7e-3
oxoacid metabolic process	GO:0043436	2	8.4e-3
organic acid metabolic process	GO:0006082	2	8.7e-3
lipid metabolic process	GO:0006629	2	1.9e-3
glycosyl compound metabolic process	GO:1901657	2	2.0e-3
aminoglycoside antibiotic metabolic process	GO:0030647	2	4.8e-3
small molecule metabolic process	GO:0044281	2	8.0e-3
glycoside metabolic process	GO:0016137	2	2.0e-2
glucocorticoid metabolic process	GO:0008211	2	3.2e-2
organic hydroxy compound metabolic process	GO:1901615	2	2.4e-2
response to mercury ion	GO:0046689	3	1.2e-2
phosphate ion transmembrane transport	GO:0035435	3	1.6e-2
stress response to copper ion	GO:1990169	4	2.0e-3
detoxification of copper ion	GO:0010273	4	2.0e-3
stress response to metal ion	GO:0097501	4	7.4e-3
detoxification of inorganic compound	GO:0061687	4	7.4e-3
cellular response to zinc ion	GO:0071294	4	2.0e-2
cellular response to copper ion	GO:0071280	4	3.1e-2
phosphate ion transmembrane transport	GO:0035435	5	1.6e-2

organic hydroxy compound metabolic process	GO:1901615	5	3.9e-2
small molecule metabolic process	GO:0044281	5	1.9e-2
organic acid metabolic process	GO:0006082	5	5.5e-4
oxoacid metabolic process	GO:0043436	5	5.3e-4
carboxylic acid metabolic process	GO:0019752	5	4.7e-4
4-nitrophenol metabolic process	GO:0018960	5	1.4e-4
response to xenobiotic stimulus	GO:0009410	5	2.5e-2
inorganic ion transmembrane transport	GO:0098660	6	5.3e-3
monoatomic ion transmembrane transport	GO:0034220	6	8.7e-3
proton transmembrane transport	GO:1902600	6	1.3e-2
monoatomic ion transport	GO:0006811	6	2.7e-2
Cellular Component			
apical part of cell	GO:0045177	2	2.7e-3
apical plasma membrane	GO:0016324	2	4.9e-2
glial cell projection	GO:0097386	4	1.3e-2
membrane	GO:0016020	6	8.1e-3
mitochondrial inner-outer membrane contact site	GO:0044289	6	4.9e-2
postsynaptic spectrin-associated cytoskeleton	GO:0099189	6	5.0e-2
KEGG Pathway			
Collecting duct acid secretion	KEGG:04966	6	9.0e-3

APPENDIX XXIV: CLUSTER 0 PAIRWISE GO TERMS RESULTS FOR TISSUE A1

Cluster GMT File	GO Term	GO ID	P-Value
Cluster 1	Abnormal pericardium morphology	HP:0001697	0.049719
Cluster 1	Distal convoluted tubule 1 (DCT1) cell	WP:WP4183	0.04996
Cluster 2	transmembrane transporter complex	GO:1902495	0.003981
Cluster 2	respiratory chain complex	GO:0098803	0.005118
Cluster 2	respirasome	GO:0070469	0.005118
Cluster 2	mitochondrial respirasome	GO:0005746	0.005118
Cluster 2	transporter complex	GO:1990351	0.009383
Cluster 2	oxidoreductase complex	GO:1990204	0.01706
Cluster 2	inner mitochondrial membrane protein complex	GO:0098800	0.01706
Cluster 2	Respiratory electron transport	REAC:R-MMU-611105	0.040563
Cluster 2	Respiratory electron transport, ATP synthesis by chemiosmotic coupling, and heat production by uncoupling proteins.	REAC:R-MMU-163200	0.049577
Cluster 2	Electron transport chain	WP:WP295	0.017006
Cluster 4	Metapathway biotransformation	WP:WP1251	0.021448
Cluster 4	G protein signaling pathways	WP:WP232	0.021448
Cluster 4	Focal adhesion: PI3K-Akt-mTOR signaling pathway	WP:WP2841	0.029377
Cluster 6	generation of precursor metabolites and energy	GO:0006091	2.26E-05
Cluster 6	energy derivation by oxidation of organic compounds	GO:0015980	3.72E-05
Cluster 6	cellular respiration	GO:0045333	0.000101
Cluster 6	aerobic respiration	GO:0009060	0.000165
Cluster 6	oxidative phosphorylation	GO:0006119	0.000711
Cluster 6	mitochondrial respiratory chain complex assembly	GO:0033108	0.012377
Cluster 6	electron transport chain	GO:0022900	0.049976
Cluster 6	mitochondrion	GO:0005739	7.42E-07
Cluster 6	mitochondrial envelope	GO:0005740	1.02E-06
Cluster 6	organelle inner membrane	GO:0019866	1.79E-06
Cluster 6	mitochondrial inner membrane	GO:0005743	1.79E-06
Cluster 6	mitochondrial membrane	GO:0031966	2.61E-06
Cluster 6	organelle envelope	GO:0031967	2.80E-06
Cluster 6	envelope	GO:0031975	2.80E-06
Cluster 6	mitochondrial protein-containing complex	GO:0098798	0.000117
Cluster 6	inner mitochondrial membrane protein complex	GO:0098800	0.000143
Cluster 6	respirasome	GO:0070469	0.000143
Cluster 6	respiratory chain complex	GO:0098803	0.00036
Cluster 6	mitochondrial respirasome	GO:0005746	0.00036

Cluster 6	oxidoreductase complex	GO:1990204	0.003501
Cluster 6	mitochondrial respiratory chain complex I	GO:0005747	0.032172
Cluster 6	NADH dehydrogenase complex	GO:0030964	0.032172
Cluster 6	respiratory chain complex I	GO:0045271	0.032172
Cluster 6	Metabolism	REAC:R-MMU-1430728	2.38E-06
Cluster 6	The citric acid (TCA) cycle and respiratory electron transport	REAC:R-MMU-1428517	1.68E-05
Cluster 6	Respiratory electron transport	REAC:R-MMU-611105	0.000127
Cluster 6	Respiratory electron transport, ATP synthesis by chemiosmotic coupling, and heat production by uncoupling proteins.	REAC:R-MMU-163200	0.000127
Cluster 6	Complex I biogenesis	REAC:R-MMU-6799198	0.014361
Cluster 6	Electron transport chain	WP:WP295	7.65E-05
Cluster 6	Oxidative phosphorylation	WP:WP1248	0.005627

APPENDIX XXV: CLUSTER 1 PAIRWISE GO TERM RESULTS FOR TISSUE A1

Cluster 0	**Metallothionein-3 complex**	**CORUM:676**	**0.049841**
Cluster 0	Mt3-Hsp84-Ck complex	CORUM:677	0.049841
Cluster 0	Distal convoluted tubule 1 (DCT1) cell	WP:WP4183	0.049515
Cluster 2	Profilin 1 complex	CORUM:2836	0.005042
Cluster 2	cell adhesion	GO:0007155	0.01896
Cluster 2	melanosome	GO:0042470	0.02679
Cluster 2	pigment granule	GO:0048770	0.02679
Cluster 2	Glutathione and one-carbon metabolism	WP:WP730	0.041299

APPENDIX XXVI: CLUSTER 2 PAIRWISE GO TERM RESULTS FOR TISSUE A1

GMT Cluster File	Go Term	GO ID	P-Value
Cluster 1	Biological oxidations	REAC:R-MMU-211859	0.049869
Cluster 3	cellular metabolic process	GO:0044237	0.030313
Cluster 3	cellular response to chemical stimulus	GO:0070887	0.032108
Cluster 3	mitochondrion	GO:0005739	0.039084
Cluster 3	Metabolism	REAC:R-MMU-1430728	0.049766

APPENDIX XXVII: CLUSTER 3 PAIRWISE GO TERM RESULTS FOR TISSUE A1

GMT Cluster File	GO Term	GO ID	P-Value
Cluster 2	3-phosphoinositide-dependent protein kinase binding	GO:0043423	0.04992
Cluster 2	Amino Acid conjugation	REAC:R-MMU-156587	0.049943
Cluster 2	Amino acids regulate mTORC1	REAC:R-MMU-9639288	0.008496
Cluster 2	apical part of cell	GO:0045177	0.001592
Cluster 2	apical plasma membrane	GO:0016324	0.000767
Cluster 2	ATPase activity, coupled to transmembrane movement of ions, rotational mechanism	GO:0044769	0.00379
Cluster 2	ATPase complex	GO:1904949	0.023833
Cluster 2	ATPase-coupled ion transmembrane transporter activity	GO:0042625	0.00379
Cluster 2	ATPase-coupled monoatomic cation transmembrane transporter activity	GO:0019829	0.01049
Cluster 2	ATPase-coupled transmembrane transporter activity	GO:0042626	0.01049
Cluster 2	ATP-dependent activity	GO:0140657	0.04025
Cluster 2	brush border	GO:0005903	0.029864
Cluster 2	carboxylic acid metabolic process	GO:0019752	0.005632
Cluster 2	cell projection	GO:0042995	0.004512
Cluster 2	cell projection membrane	GO:0031253	0.025839
Cluster 2	cellular response to aldehyde	GO:0110096	0.04992
Cluster 2	cellular response to aldosterone	GO:1904045	0.04992
Cluster 2	cellular response to mineralocorticoid stimulus	GO:0071389	0.04992
Cluster 2	Cellular response to starvation	REAC:R-MMU-9711097	0.008496
Cluster 2	cluster of actin-based cell projections	GO:0098862	0.029864
Cluster 2	Conjugation of benzoate with glycine	REAC:R-MMU-177135	0.049943
Cluster 2	Conjugation of carboxylic acids	REAC:R-MMU-159424	0.049943
Cluster 2	enzyme inhibitor activity	GO:0004857	0.015687
Cluster 2	G protein-coupled receptor activity	GO:0004930	0.049947
Cluster 4	glucocorticoid mediated signaling pathway	GO:0043402	0.04992
Cluster 4	GPCRs, non-odorant	WP:WP1396	0.001414

Cluster 4	Insulin receptor recycling	REAC:R-MMU-77387	0.008496
Cluster 4	intracellular sodium ion homeostasis	GO:0006883	0.04992
Cluster 4	Iron uptake and transport	REAC:R-MMU-917937	0.014793
Cluster 4	Metapathway biotransformation	WP:WP1251	0.005373
Cluster 4	mmu-miR-186-5p	MIRNA:mmu-miR-186-5p	0.049712
Cluster 4	mmu-miR-208a-5p	MIRNA:mmu-miR-208a-5p	0.049712
Cluster 4	mmu-miR-335-3p	MIRNA:mmu-miR-335-3p	0.049712
Cluster 4	mmu-miR-693-3p	MIRNA:mmu-miR-693-3p	0.049712
Cluster 4	molecular function inhibitor activity	GO:0140678	0.032938
Cluster 4	organic acid metabolic process	GO:0006082	0.007847
Cluster 5	oxoacid metabolic process	GO:0043436	0.007847
Cluster 6	plasma membrane bounded cell projection	GO:0120025	0.003505
Cluster 6	plasma membrane region	GO:0098590	0.008816
Cluster 6	positive regulation of cell morphogenesis involved in differentiation	GO:0010770	0.04992
Cluster 6	positive regulation of dendrite morphogenesis	GO:0050775	0.04992
Cluster 6	protein serine/threonine/tyrosine kinase activity	GO:0004712	0.04992
Cluster 6	proton transmembrane transporter activity	GO:0015078	0.022215
Cluster 6	proton-transporting ATPase activity, rotational mechanism	GO:0046961	0.00379
Cluster 6	proton-transporting two-sector ATPase complex	GO:0016469	0.016025
Cluster 6	proton-transporting V-type ATPase complex	GO:0033176	0.005821
Cluster 6	pyrophosphate hydrolysis-driven proton transmembrane transporter activity	GO:0009678	0.00379
Cluster 6	regulation of cell morphogenesis involved in differentiation	GO:0010769	0.04992
Cluster 6	response to aldosterone	GO:1904044	0.04992
Cluster 6	response to chemical	GO:0042221	0.001818
Cluster 6	response to extracellular stimulus	GO:0009991	0.001151
Cluster 6	response to mineralocorticoid	GO:0051385	0.04992
Cluster 6	response to nutrient levels	GO:0031667	0.001151
Cluster 6	response to oxygen-containing compound	GO:1901700	0.045034
Cluster 6	response to toxic substance	GO:0009636	0.013655
Cluster 6	response to xenobiotic stimulus	GO:0009410	0.009548
Cluster 6	Retinol metabolism	WP:WP1259	0.049997
Cluster 6	Retinol metabolism	WP:WP1259	0.049963
Cluster 6	ROS and RNS production in phagocytes	REAC:R-MMU-	0.008496

		1222556	
Cluster 6	Signaling by Insulin receptor	REAC:R-MMU-74752	0.008496
Cluster 6	Signaling by Receptor Tyrosine Kinases	REAC:R-MMU-9006934	0.049948
Cluster 6	Transferrin endocytosis and recycling	REAC:R-MMU-917977	0.008496
Cluster 6	vacuolar membrane	GO:0005774	0.033759
Cluster 6	vacuolar proton-transporting V-type ATPase complex	GO:0016471	0.005821

APPENDIX XXVIII: CLUSTER 4 PAIRWISE GO TERM RESULTS FOR TISSUE A1

GMT Cluster File	GO Term	GO ID	P-Value
Cluster 2	cytosolic small ribosomal subunit	GO:0022627	0.010775
Cluster 2	cytosolic ribosome	GO:0022626	0.02679
Cluster 2	Abnormal anterior horn cell morphology	HP:0006802	0.049929
Cluster 2	Degeneration of anterior horn cells	HP:0002398	0.049929
Cluster 2	Pseudobulbar paralysis	HP:0007024	0.049929
Cluster 2	Cytoplasmic ribosomal proteins	WP:WP163	0.033581
Cluster 3	regulation of dendrite development	GO:0050773	0.049831
Cluster 3	hormone-mediated signaling pathway	GO:0009755	0.049831
Cluster 3	positive regulation of neurogenesis	GO:0050769	0.049831
Cluster 3	protein polymerization	GO:0051258	0.049831
Cluster 3	memory	GO:0007613	0.049831
Cluster 3	negative regulation of protein polymerization	GO:0032272	0.049831
Cluster 3	cellular response to aldosterone	GO:1904045	0.049831
Cluster 3	regulation of dendrite morphogenesis	GO:0048814	0.049831
Cluster 3	visual learning	GO:0008542	0.049831
Cluster 3	associative learning	GO:0008306	0.049831
Cluster 3	regulation of neurogenesis	GO:0050767	0.049831
Cluster 3	regulation of protein polymerization	GO:0032271	0.049831
Cluster 3	positive regulation of cell morphogenesis involved in differentiation	GO:0010770	0.049831
Cluster 3	positive regulation of cell development	GO:0010720	0.049831
Cluster 3	positive regulation of sodium ion transport	GO:0010765	0.049831
Cluster 3	regulation of cell morphogenesis involved in differentiation	GO:0010769	0.049831
Cluster 3	regulation of cell morphogenesis	GO:0022604	0.049831
Cluster 3	positive regulation of cell projection organization	GO:0031346	0.049831
Cluster 3	negative regulation of protein-containing complex assembly	GO:0031333	0.049831
Cluster 3	cellular response to mineralocorticoid stimulus	GO:0071389	0.049831
Cluster 3	cognition	GO:0050890	0.049831
Cluster 3	negative regulation of microtubule polymerization	GO:0031115	0.049831
Cluster 3	regulation of microtubule polymerization	GO:0031113	0.049831
Cluster 3	positive regulation of dendrite morphogenesis	GO:0050775	0.049831
Cluster 3	dendrite morphogenesis	GO:0048813	0.049831
Cluster 3	dendrite development	GO:0016358	0.049831
Cluster 3	visual behavior	GO:0007632	0.049831
Cluster 3	glucocorticoid mediated signaling pathway	GO:0043402	0.049831
Cluster 3	regulation of nervous system development	GO:0051960	0.049831

Cluster 3	positive regulation of cell differentiation	GO:0045597	0.049831
Cluster 3	microtubule polymerization	GO:0046785	0.049831
Cluster 3	positive regulation of nervous system development	GO:0051962	0.049831
Cluster 3	intracellular sodium ion homeostasis	GO:0006883	0.049831
Cluster 3	learning	GO:0007612	0.049831
Cluster 3	regulation of sodium ion transport	GO:0002028	0.049831
Cluster 3	long-term memory	GO:0007616	0.049831
Cluster 3	learning or memory	GO:0007611	0.049831
Cluster 3	steroid hormone mediated signaling pathway	GO:0043401	0.049831
Cluster 3	cytoskeletal protein binding	GO:0008092	0.04985
Cluster 3	potassium channel regulator activity	GO:0015459	0.04985
Cluster 3	ion channel regulator activity	GO:0099106	0.04985
Cluster 3	channel regulator activity	GO:0016247	0.04985
Cluster 3	protein serine/threonine/tyrosine kinase activity	GO:0004712	0.04985
Cluster 3	3-phosphoinositide-dependent protein kinase binding	GO:0043423	0.04985
Cluster 3	tau protein binding	GO:0048156	0.04985
Cluster 3	Stimuli-sensing channels	REAC:R-MMU-2672351	0.049801
Cluster 3	NGF-stimulated transcription	REAC:R-MMU-9031628	0.049801
Cluster 3	Regulation of TP53 Expression and Degradation	REAC:R-MMU-6806003	0.049801
Cluster 3	Regulation of TP53 Degradation	REAC:R-MMU-6804757	0.049801
Cluster 3	Regulation of TP53 Activity	REAC:R-MMU-5633007	0.049801
Cluster 3	Transcriptional Regulation by TP53	REAC:R-MMU-3700989	0.049801
Cluster 3	Signaling by NTRKs	REAC:R-MMU-166520	0.049801
Cluster 3	Signaling by NTRK1 (TRKA)	REAC:R-MMU-187037	0.049801
Cluster 3	Nuclear Events (kinase and transcription factor activation)	REAC:R-MMU-	0.049801

		198725	
Cluster 3	Mechanisms associated with pluripotency	WP:WP1763	0.04995
Cluster 3	Insulin signaling	WP:WP65	0.04995
Cluster 3	IL-6 signaling pathway	WP:WP387	0.04995
Cluster 5	memory	GO:0007613	0.049975
Cluster 5	positive regulation of sodium ion transport	GO:0010765	0.049975
Cluster 5	learning or memory	GO:0007611	0.049975
Cluster 5	learning	GO:0007612	0.049975
Cluster 5	cognition	GO:0050890	0.049975
Cluster 5	long-term memory	GO:0007616	0.049975
Cluster 5	visual behavior	GO:0007632	0.049975
Cluster 5	positive regulation of dendrite morphogenesis	GO:0050775	0.049975
Cluster 5	positive regulation of neurogenesis	GO:0050769	0.049975
Cluster 5	cellular response to aldosterone	GO:1904045	0.049975
Cluster 5	associative learning	GO:0008306	0.049975
Cluster 5	visual learning	GO:0008542	0.049975
Cluster 5	regulation of protein polymerization	GO:0032271	0.049975
Cluster 5	negative regulation of microtubule polymerization	GO:0031115	0.049975
Cluster 5	regulation of cell morphogenesis involved in differentiation	GO:0010769	0.049975
Cluster 5	negative regulation of protein polymerization	GO:0032272	0.049975
Cluster 5	positive regulation of nervous system development	GO:0051962	0.049975
Cluster 5	glucocorticoid mediated signaling pathway	GO:0043402	0.049975
Cluster 5	regulation of sodium ion transport	GO:0002028	0.049975
Cluster 5	microtubule polymerization	GO:0046785	0.049975
Cluster 5	positive regulation of cell morphogenesis involved in differentiation	GO:0010770	0.049975
Cluster 5	dendrite morphogenesis	GO:0048813	0.049975
Cluster 5	regulation of microtubule polymerization	GO:0031113	0.049975
Cluster 5	protein polymerization	GO:0051258	0.049975
Cluster 5	regulation of dendrite morphogenesis	GO:0048814	0.049975
Cluster 5	channel regulator activity	GO:0016247	0.049975
Cluster 5	potassium channel regulator activity	GO:0015459	0.049975
Cluster 5	protein serine/threonine/tyrosine kinase activity	GO:0004712	0.049975
Cluster 5	ion channel regulator activity	GO:0099106	0.049975
Cluster 5	tau protein binding	GO:0048156	0.049975
Cluster 5	3-phosphoinositide-dependent protein kinase binding	GO:0043423	0.049975
Cluster 5	NGF-stimulated transcription	REAC:R-MMU-9031628	0.049961
Cluster 5	Regulation of TP53 Expression and Degradation	REAC:R-	0.049961

		MMU-6806003	
Cluster 5	Regulation of TP53 Degradation	REAC:R-MMU-6804757	0.049961
Cluster 5	Stimuli-sensing channels	REAC:R-MMU-2672351	0.049961
Cluster 5	Nuclear Events (kinase and transcription factor activation)	REAC:R-MMU-198725	0.049961
Cluster 6	actin cytoskeleton organization	GO:0030036	0.034996
Cluster 6	actin filament-based process	GO:0030029	0.049973
Cluster 6	structural molecule activity	GO:0005198	0.001098
Cluster 6	RNA binding	GO:0003723	0.007084
Cluster 6	actin filament binding	GO:0051015	0.01589
Cluster 6	nucleic acid binding	GO:0003676	0.04319
Cluster 6	mmu-miR-9-5p	MIRNA:mmu-miR-9-5p	0.03371
Cluster 6	GTP hydrolysis and joining of the 60S ribosomal subunit	REAC:R-MMU-72706	0.005874
Cluster 6	L13a-mediated translational silencing of Ceruloplasmin expression	REAC:R-MMU-156827	0.005874
Cluster 6	Cap-dependent Translation Initiation	REAC:R-MMU-72737	0.005874
Cluster 6	Eukaryotic Translation Initiation	REAC:R-MMU-72613	0.005874
Cluster 6	SRP-dependent cotranslational protein targeting to membrane	REAC:R-MMU-1799339	0.005874
Cluster 6	Formation of a pool of free 40S subunits	REAC:R-MMU-72689	0.005874
Cluster 6	Nonsense-Mediated Decay (NMD)	REAC:R-MMU-927802	0.005874
Cluster 6	Nonsense Mediated Decay (NMD) independent of the Exon Junction Complex (EJC)	REAC:R-MMU-975956	0.005874
Cluster 6	Nonsense Mediated Decay (NMD) enhanced by the Exon Junction Complex (EJC)	REAC:R-MMU-975957	0.005874
Cluster 6	rRNA processing	REAC:R-MMU-72312	0.032544
Cluster 6	rRNA processing in the nucleus and cytosol	REAC:R-	0.032544

		MMU-8868773	
Cluster 6	Major pathway of rRNA processing in the nucleolus and cytosol	REAC:R-MMU-6791226	0.032544
Cluster 6	Cytoplasmic ribosomal proteins	WP:WP163	0.00352
Cluster 6	Metapathway biotransformation	WP:WP1251	0.049882

APPENDIX XXIX: CLUSTER 5 PAIRWISE GO TERMS RESULTS FOR TISSUE A1

GMT Cluster File	GO Term	GO ID	P-Value
Cluster 1	small molecule binding	GO:0036094	0.049811
Cluster 2	apical part of cell	GO:0045177	0.000374
Cluster 2	apical plasma membrane	GO:0016324	0.000402
Cluster 2	plasma membrane region	GO:0098590	0.00077
Cluster 2	plasma membrane	GO:0005886	0.035153
Cluster 2	endomembrane system	GO:0012505	0.048734
Cluster 2	lipid binding	GO:0008289	0.007643
Cluster 2	Biological oxidations	REAC:R-MMU-211859	0.046198
Cluster 3	response to organic substance	GO:0010033	0.049958
Cluster 3	Metabolism	REAC:R-MMU-1430728	0.020863
Cluster 4	cellular response to mineralocorticoid stimulus	GO:0071389	0.04992
Cluster 4	cellular response to aldosterone	GO:1904045	0.04992
Cluster 4	response to aldosterone	GO:1904044	0.04992
Cluster 4	glucocorticoid mediated signaling pathway	GO:0043402	0.04992

Cluster 4	positive regulation of dendrite morphogenesis	GO:0050775	0.04992
Cluster 4	cellular response to aldehyde	GO:0110096	0.04992
Cluster 4	response to mineralocorticoid	GO:0051385	0.04992
Cluster 4	intracellular sodium ion homeostasis	GO:0006883	0.04992
Cluster 4	positive regulation of cell morphogenesis involved in differentiation	GO:0010770	0.04992
Cluster 4	regulation of cell morphogenesis involved in differentiation	GO:0010769	0.04992
Cluster 4	protein serine/threonine/tyrosine kinase activity	GO:0004712	0.04992
Cluster 4	3-phosphoinositide-dependent protein kinase binding	GO:0043423	0.04992

APPENDIX XXX: CLUSTER 6 PAIRWISE GO TERM RESULTS FOR TISSUE A1

GMT Cluster File	GO Term	GO ID	P-Value
Cluster 3	proton transmembrane transport	GO:1902600	0.020855
Cluster 3	proton-transporting V-type ATPase complex	GO:0033176	0.010085
Cluster 3	ATPase complex	GO:1904949	0.010085
Cluster 3	proton-transporting two-sector ATPase complex	GO:0016469	0.010085
Cluster 3	vacuolar proton-transporting V-type ATPase complex	GO:0016471	0.010085
Cluster 3	vacuolar membrane	GO:0005774	0.010085
Cluster 3	catalytic complex	GO:1902494	0.038721
Cluster 3	ATPase activity, coupled to transmembrane movement of ions, rotational mechanism	GO:0044769	0.003198
Cluster 3	proton-transporting ATPase activity, rotational mechanism	GO:0046961	0.003198
Cluster 3	ATPase-coupled monoatomic cation transmembrane transporter activity	GO:0019829	0.003198
Cluster 3	ATPase-coupled ion transmembrane transporter activity	GO:0042625	0.003198
Cluster 3	primary active transmembrane transporter activity	GO:0015399	0.003198
Cluster 3	ATPase-coupled transmembrane transporter activity	GO:0042626	0.003198
Cluster 3	proton transmembrane transporter activity	GO:0015078	0.003198
Cluster 3	pyrophosphate hydrolysis-driven proton transmembrane transporter activity	GO:0009678	0.003198
Cluster 3	active monoatomic ion transmembrane transporter activity	GO:0022853	0.030275
Cluster 3	ATP-dependent activity	GO:0140657	0.030275
Cluster 3	Cellular response to starvation	REAC:R-MMU-9711097	0.002629
Cluster 3	Amino acids regulate mTORC1	REAC:R-MMU-9639288	0.002629
Cluster 3	Transferrin endocytosis and recycling	REAC:R-MMU-917977	0.002629
Cluster 3	Iron uptake and transport	REAC:R-MMU-917937	0.002629
Cluster 3	Insulin receptor recycling	REAC:R-MMU-77387	0.002629

Cluster 3	Signaling by Insulin receptor	REAC:R-MMU-74752	0.002629
Cluster 3	Signal Transduction	REAC:R-MMU-162582	0.004974
Cluster 3	Ion channel transport	REAC:R-MMU-983712	0.010303
Cluster 3	ROS and RNS production in phagocytes	REAC:R-MMU-1222556	0.010303
Cluster 3	Innate Immune System	REAC:R-MMU-168249	0.025224
Cluster 3	Signaling by Receptor Tyrosine Kinases	REAC:R-MMU-9006934	0.025224
Cluster 3	Cellular responses to stress	REAC:R-MMU-2262752	0.049382
Cluster 3	Transport of small molecules	REAC:R-MMU-382551	0.049382
Cluster 3	Cellular responses to stimuli	REAC:R-MMU-8953897	0.049382
Cluster 3	GPCRs, non-odorant	WP:WP1396	0.009231

APPENDIX XXXI: IACUC APPROVAL LETTER

University of New Hampshire

Research Integrity Services, Service Building51 College Road, Durham,
NH 03824-3585
Fax: 603-862-3564

22-Jun-2023

MacManes, Matthew D
Molecular, Cellular & Biomedical SciencesGregg Hall Room 434
Durham, NH 03824-3521

IACUC #: 210602

Project: Using Physiology and Genomics to Understand Adaptation to Desert Life in Rodents
Next Review Date: 01-Jul-2024

The Institutional Animal Care and Use Committee (IACUC) has reviewed and approved your requestfor a time extension for this protocol. Approval is granted until the "Next Review Date" indicated above. You will be asked to submit a report with regard to the involvement of animals in this study before that date. If your study is still active, you may apply for extension of IACUC approval through this office.

The appropriate use and care of animals in your study is an ongoing process for which you hold primary responsibility. Changes in your protocol must be submitted to the IACUC for review andapproval prior to their implementation.

Please Note:

1. All cage, pen, or other animal identification records must include your IACUC # listed above.
2. Use of animals in research and instruction is approved contingent upon participation in the UNHOccupational Health Program for persons handling animals. Participation is mandatory for all principal investigators and their affiliated personnel, employees of the University and students alike. Information about the program, including forms, is available at http://unh.edu/research/occupational-health-program-animal-handlers.

If you have any questions, please contact either Dean Elder at 862-4629 or Susan Jalbert at 862-3536.

For the IACUC,

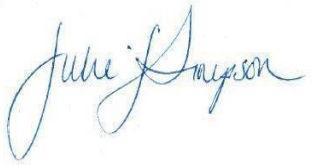

Julie Simpson, Ph.D.
Director